UNIVERSITY OF OKLAHOMA
GRADUATE COLLEGE

OBSERVATIONS AND SIMULATIONS OF POLARIMETRIC RADAR SIGNATURES DURING THE 24 – 25 MAY 2011 TORNADO OUTBREAK

A DISSERTATION
SUBMITTED TO THE GRADUATE FACULTY
in partial fulfillment of the requirements for the
Degree of
DOCTOR OF PHILOSOPHY

by RACHAEL N. CROSS

Norman, Oklahoma

2026

Downloaded from SHAREOK. Persistent Handle URL: https://hdl.handle.net/11244/342850

OBSERVATIONS AND SIMULATIONS OF POLARIMETRIC RADAR SIGNATURES DURING THE 24 – 25 MAY 2011 TORNADO OUTBREAK

A DISSERTATION APPROVED FOR THE
SCHOOL OF METEOROLOGY

BY THE COMMITTEE CONSISTING OF

Dr. David Bodine (Chair)

Dr. Robert Palmer

Dr. Leigh Orf

Dr. Jason Furtado

Dr. Caleb Fulton

©Copyright by RACHAEL N. CROSS 2026

All Rights Reserved.

Acknowledgments

The completion of this dissertation would not have been possible without the love and support from numerous people. I honestly could write an entire, separate book about the overwhelming support I have received from friends, family, pets, and professionals in the field, but I will try and summarize some of the highlights here.

Firstly, I want to thank my fiance, Dr. Michael Hosek, for supporting me through the ups and downs of my Ph.D. From being there and comforting me as I cry in my office to celebrating every small win, his steady confidence in my abilities to finish my Ph.D. helped me complete this dissertation. I am truly blessed to have such a supportive partner and am consistently overwhelmed by his love and support.

Now, Dr. Emily Lenhardt and I have been at OU together for 10 years. She and I have laughed, cried, and lost our minds together during our time here at OU and I would not have had it any other way. Emily became my sister throughout the stress of undergrad and grad school, and being her roommate and friend made the grad school experience so fun and enjoyable. While I am sad the completion of this dissertation marks the end of our time here together at OU, I look forward to causing mayhem at future conferences together.

To my other OU undergrad friends – Dr. Morgan Schneider and Sam Emmerson – they too became long standing friends of mine who I cherish dearly. They contributed to the joy I experienced here at OU and I am forever grateful for their friendship. And for the new friends I made during graduate school – Alec Prosser, Laura Shedd, Brandon Cohen, Dr. Margaret Hollis, Erin Jones, Stephen Foskey, Maddy Diedrichsen, Dr. Kevin Thiel, Logan Mitchell, Dr. Arianna Jordan, Jessica Davis, Katie Giesa, Peter Brechner, and Zhihong Chen – they all contributed to the many great times I

had here at OU. From Flapjack Friday to ghost hunting to daily lunches together, this friend group has been warm and welcoming, making Norman, OK truly feel like home.

Thank you to my mom and dad for always supporting me. Throughout my graduate school experience I had numerous health scares, and my family was always right by my side to help me get back on my feet. Also, thank you to Michael's parents for their support and giving me a second home up in NY. And, of course, thank you to my sister, Emily. Her humor and support is always a light in my life and it definitely help me through graduate school.

To my first research advisor, Dr. Daphne LaDue, thank you for guiding me through my first research project and helping me develop my love for research. Without your excellent and careful guidance, I would not be where I am today. Also, thank you to Dr. Joe Ripberger for letting Emily and I write a paper together and for giving us that summer internship. That was one of the most enjoyable projects I have done (I just hope Emily and I's constant giggling while we were working wasn't too annoying!). Furthermore, thank you to Dr. T down at Collin College in Plano, TX for your constant belief in me and for always being there to provide advice or just an listening ear.

Of course, none of this would have been possible without Dr. David Bodine. David, being advised by you was truly a blessing. Thank you for letting me into the world of radar meteorology and teaching me so many things, from how to handle challenging teaching scenarios to how to conduct independent research. There is a reason you have an army of students – you are an excellent advisor and I am so happy to have been able to be one of your students!

Thank you to my committee members, Dr. Robert Palmer, Dr. Leigh Orf. Dr. Jason Furtado, and Dr. Caleb Fulton, for taking the time to serve on my committee. Each and every one of you enhanced my graduate school experience and I learned a lot about teaching, research, and faculty life from each of you. This work was also

supported by NSF grants AGS-1823478 and AGS-2114817. Collaborations with L. Orf are funded by AGS-1832327, AGS-2114757 and OAC-1663954.

Finally, thank you to my soul dog, Iza. He was with me from the start of college at Collin College up to 1 week after my Ph.D. defense. He was the definition of love wrapped up in a ball of energetic fluff. I could not have asked for a better dog to be by my side throughout college, and he will forever have a place in my heart as one of the best dogs to ever exist.

Table of Contents

Acknowledgments . . . iv

List of Tables . . . ix

List of Figures . . . x

Abstract . . . xvi

1 Introduction . . . 1

2 A Case Study of Polarimetric Radar Signatures Across Tornadic and Nontornadic Supercells in a Volatile Environment During the 24 – 25 May 2011 Outbreak . . . 8
- 2.1 Introduction . . . 8
- 2.2 Data and Methodology . . . 12
  - 2.2.1 Polarimetric Signature Identification . . . 15
- 2.3 Results . . . 17
  - 2.3.1 Z_{DR} Column . . . 21
  - 2.3.2 Z_{DR} Arc . . . 30
  - 2.3.3 K_{DP} Foot . . . 36
  - 2.3.4 Z_{DR}-K_{DP} Separation Vector . . . 37
  - 2.3.5 Storm Interactions . . . 43
- 2.4 Summary and Discussion . . . 45

3 A Comparative Analysis of Polarimetric Radar Signatures in Pre-Tornadic Supercells Across CM1 Microphysics Schemes and Observations . . . 49
- 3.1 Introduction . . . 49
- 3.2 Data and Methodology . . . 54
  - 3.2.1 Description of Observations . . . 55
  - 3.2.2 Melting Models . . . 56
  - 3.2.3 Polarimetric Forward Operator . . . 59
  - 3.2.4 CM1 Model Configuration . . . 62
- 3.3 Results . . . 66

3.3.1 Melting Model Comparison 66
3.3.2 Microphysics Comparison to KOUN Observations 81
3.4 Conclusions 102

4 The Impact of Microphysics Schemes on the Dynamics, Thermodynamics, and Polarimetric Radar Signatures in Simulated Tornadic Supercells 107
4.1 Introduction 107
4.2 Methodology 111
4.2.1 Polarimetric Signature Identification 114
4.3 Results 114
4.3.1 Tornado Characteristics 114
4.3.2 Updraft Characteristics 119
4.3.3 Cold Pool Characteristics 129
4.3.4 Relationships Between Polarimetric Signatures and Supercell Dynamics 133
4.3.5 Conclusion 140

5 Summary and Conclusions 146

Reference List 152

List of Tables

2.1 Table of supercells from 24 – 25 May 2011. Supercells with an asterisk were not analyzed due to a lack of data or distance from KOUN. The time window for each TOR was taken from NWS storm data. Distance from KOUN was calculated at 5.0 km AGL from the gridded radar data. 14

2.2 Time of first radar echo (defined as $Z_H > 20$ dBZ) as seen by KTLX at an elevation angle of 0.5°, time of the genesis of the first tornado in the supercell or time of VROT_{max}, and the difference between the tornadogenesis and first echo times. 19

2.3 Environmental parameters from the near-storm environment taken from ERA5 and SPC Mesoanalysis. Values from the NWS for supercells and values for significant tornadoes from Thompson et al. (2003) are provided for comparison. Values for each supercell were taken from the closest time step before the first tornado or maximum VROT. 21

3.1 List of densities for each hydrometeor category. 57

3.2 Configuration of CM1 used for each simulation. 62

3.3 List of values of supercell and polarimetric areas. All areas were calculated using the 15-min composites of the simulated and observed data. The supercell area provided is valid for 1.5 km AGL. Each of the polarimetric signature areas are normalized by storm size at 1.5 km AGL (or 5.5 km AGL for the Z_{DR} column). 88

3.4 Comparison of microphysics scheme performance in representing the observed supercell and polarimetric signature area and depth. 105

4.1 Configuration of CM1 used for each simulation. 112

List of Figures

2.1 Tornado damage path overview from the National Weather Service summary of the 24 – 25 May 2011 outbreak. 15

2.2 Horizontal cross-section of ungridded Z_H from KTLX at 2031 UTC and an elevation angle of 0.5°. 19

2.3 Temporal evolution of the Z_{DR} column (a,b), Z_{DR} arc (c,d), and K_{DP} foot (e,f) prior to tornadogenesis (VROT_{max}). Solid lines represent the tornadic supercells, while dashed lines represent the nontornadic supercells. 24

2.4 Histograms of the area values for the Z_{DR} column (a,b), Z_{DR} arc (c,d), and K_{DP} foot (e,f) from T-30 to T-0 for the nontornadic (blue) and tornadic (red) supercells. 25

2.5 Time series of Z_{DR} column area starting at the time of the genesis of the last reported tornado or VROT_{max}. Solid lines represent the tornadic supercells while the dashed lines represent the nontornadic supercells. . 27

2.6 Horizontal cross-sections of gridded Z_{DR} at 5.5 km AGL as seen by KOUN for supercell B (a–c), supercell C (d–f), and supercell D (g–i). . 29

2.7 Same as in Fig. 2.6 but for supercell F (a–c), supercell G (d–f), and supercell H (g–i). 30

2.8 Horizontal cross-sections of gridded Z_{DR} at 1.5 km AGL as seen by KOUN for supercell B (a–e), supercell C (f–i), supercell D (k–o). Plots to the left of the black line are prior to the 30-min pre-tornadic window while plots to the right of the black line showcase the Z_{DR} arc during the 30-min window prior to tornadogenesis. 34

2.9 Same as in Fig. 2.8 but for supercell F (a–d), supercell G (e–f), supercell H (g–j). 35

2.10 Conceptual model of the Z_{DR} arc development for the supercells on 24 May 2011. Black dashed lines represent the 2 dB contour while red dashed lines represent the 3 dB contour. 36

2.11 Kernel density estimate contours ($\geq$ 50%) of the separation angle and distance for the tornadic (red) and nontornadic (blue) supercells during the T-30 to T-0 window. Storm motion is aligned with the 0°axis such that 90° is to the right of storm motion and -90° is to the left of storm motion. Red and blue markers represent the median separation angle and distance for the tornadic and nontornadic supercells. 38

2.12 Kernel density estimate contours of the separation angle and distance for the tornadic (left) and nontornadic (right) supercells. The T-30 window is broken down into the early intensification phase (T-30 to T-15), the late intensification phase (T-15 to T), and after the intensification phase. Storm motion is aligned with the 0°axis such that 90° is to the right of storm motion and -90° is to the left of storm motion. 39

2.13 Evolution of the Z_{DR} -K_{DP} separation angle and distance for supercell C during and after the T-30 to T-0 window. The mesocyclone as seen by KTLX at 0.5°(black circle), K_{DP} foot (blue contour), K_{DP} foot centroid (blue point), Z_{DR} arc (black contour), Z_{DR} arc centroid (black point), and reflectivity (colorfill) at 1.5 km AGL are shown. 40

2.14 Evolution of supercell interactions for supercell B (a – c), supercell C (d – e), and supercell G (f – h) at 1.5 km AGL. The mesocyclones at 0.5°as seen by KTLX are shown (black circle and star). White dashed lines represent the 1 dB contour at 5.5 km AGL. The x- and y-axes are adjusted to remain centered on each supercell. 45

3.1 Horizontal cross-section of Z_H (a–c) and horizontal velocity (d–e) at 0.04 km AGL for the MORR, NSSL2, and NSSL3 microphysics schemes. All plots shown are taken from the time of tornadogenesis. 65

3.2 2D histogram of the $D_{m,wh}$ (top row) and the $D_{m,wg}$ (bottom row) and N_t for the J08, L24, and CMM melting models. Values are taken from the entire depth of the supercell. Colorfill represents the frequency of the relationship between D_m and N_t. 68

3.3 Vertical cross-section of N_{wg} on a log scale for the J08 (a), L24 (b), and CMM (c) melting models. The dashed grey line represents the freezing level. The black contour denotes the 20 ms^{-1} updraft. 69

3.4 Vertical cross-section of Q_g on a log scale for the J08 (a), L24 (b), and CMM (c) melting models. The dashed grey line represents the freezing level. The black contour denotes the 20 ms^{-1} updraft. 71

3.5 Same as Fig. 3.4 but for dry hail. 72

3.6 Horizontal cross sections of hydrometeor number concentration (left column) and $D_{m,r}$ (right column) for the J08 (a,b), L24 (c,d), and CMM (e,f) melting models. Black contours represent the updraft core (w > 20 ms^{-1}) and the black arrows represent the horizontal wind field. Data from 6.0 AGL is presented. 74

3.7 Same as Fig. 3.6 but for melting hail. 75

3.8 Scatter plots relating $D_{m,g}$ and $D_{m,wg}$ to Z_{DR} for the J08 (a,b), L24 (c,d), and the CMM (e,f) melting models. Colorfill represents the liquid water fraction associated with the scatter point. 77

3.9 Horizontal cross-sections of Z_{DR} at 1.5 km AGL for the a) J08, b) L24, and c) CMM. Data shown are taken from the time of tornadogenesis for each melting model. 79

3.10 Horizontal cross-sections of Z_{DR} at 5.5 km AGL for the a) J08, b) L24, and c) CMM. Data shown are taken from the time of tornadogenesis for each melting model. 80

3.11 Horizontal cross sections of Z_H from KOUN (a,b,c) and from the CM1 simulations (d,e,f) at 1.5 km AGL. Both the observed and simulated supercells are shown at the time of tornadogenesis. 82

3.12 Vertical cross-section through the center of the Z_{DR} column for the MORR (a), NSSL2 (b), and NSSL3 (c) schemes. The data shown in this plot represent a 15-min composite. Grey colorfill represents the D_m for dry graupel. Colored contour lines represent the D_m of melting graupel. Black dashed line represents the freezing level at 4.5 km AGL. 85

3.13 Cross-section through the center of the Z_{DR} column for the MORR (a), NSSL2 (b), and NSSL3 (c) schemes. Colorfill represents f_g, and the freezing level (4.5 km AGL) is represented by the black dashed line. . . 86

3.14 Cross-section through the center of the Z_{DR} column for the MORR (a), NSSL2 (b), and NSSL3 (c) schemes. Colorfill represents Q_r, and the freezing level (4.5 km AGL) is represented by the black dashed line. . . 87

3.15 Contours of $Z_H = 30$ dBZ (a) and Z_H =50 dBZ (b) at 1.5 km AGL from the MORR (blue), NSSL2 (red), NSSL3 (gold), and observed (grey) datasets. 89

3.16 Vertical cross-sections through the center of the Z_{DR} column for the MORR (a,b), NSSL2 (c,d), NSSL3 (e,f), and observed (g,h) composited datasets. Cross-sections in the left column are zoomed in to focus on the Z_{DR} column. 92

3.17 Cross-section through the Z_{DR} column for the a) MORR, b) NSSL2, and c) NSSL3 schemes. Red contours represent the q_{g+h} field. Blue contours represent the q_r field. Contour lines represent the 2, 5, and 10 g/kg levels. 93

3.18 Horizontal cross sections of Z_{DR} (a,c,e,g) and Z_H (b,d,f,h) at 1.5 km AGL for the MORR (a,b), NSSL2 (c,d), NSSL3 (e,f), and the observed (g,h) composited datasets. 96

3.19 CFADS of Z_H for the (a) observed, (b) MORR, (c) NSSL2, and (d) NSSL3 datasets. 99

3.20 Same as in Fig. 3.19 but for Z_{DR}. 100

3.21 Same as in Fig. 3.19 but for K_{DP}. 101

4.1 Time of tornadogenesis as defined by the OW parameter for each ensemble. 115

4.2 Box plots of a) the fraction of time a supercell had an EF5 tornado, b) $V_{h,max}$ at 0.04 km, and c) maximum $V_{h,max}$ during the tornado for the MORR (blue), NSSl2 (red), and NSSL3 (green) microphysics schemes. Black lines represent the range of the data; red horizontal lines show the location of the median; and the color-filled boxes range from the 25$^{\text{th}}$ to 75$^{\text{th}}$ percentile. 116

4.3 Plots of the time of tornadogenesis (a–c) and $V_{h,max}$ at 0.04 km AGL (d–f) for the MORR (a,e), NSSL2 (b,e), and NSSL3 (c,f) microphysics schemes. 117

4.4 Time-height plot of ζ_{max} for the a) MORR, b) NSSL2, and c) NSSL3 microphysics schemes. Values of ζ_{max} are averaged across ensemble members. 119

4.5 Box plots of the updraft area at T-0 at 1 km AGL (a–b) and 5.5 km AGL (c–d) for the MORR (blue), NSSL2 (red), and NSSL3 (green) microphysics schemes. Black lines represent the range of the data; red horizontal lines show the location of the median; and the color-filled boxes range from the 25$^{\text{th}}$ to 75$^{\text{th}}$ percentile. 121

4.6 Time series of w_max at 1 km AGL for the a) MORR, b) NSSL2, and c) NSSL3 ensembles. Black lines represent the 50$^{\text{th}}$ percentile while the colorfill ranges from the 0$^{\text{th}}$ to the 100$^{\text{th}}$ percentile. 122

4.7 Horizontal cross-section of surface (0.04 km AGL) convergence with the 1 km (white solid) and 5.5 km (black dashed) updraft contours at w = 20 m s^{-1} for the a) MORR, b) NSSL2, and c) NSSL3 ensembles. Values of convergence and W are averaged across ensemble members at T-0. . 124

4.8 Horizontal cross-section of θ'_p and W at 5.5 km AGL and at T-0 for the a) MORR, b) NSSL2, and c) NSSL3 ensembles. Values of convergence and W are averaged across ensemble members. Yellow contour represents W = 20 m s^{-1}. 124

4.9 Horizontal cross-section of the frequency $w > 20$ m s^{-1} (colorfill) and $Z_{DR} > 1$ dB (contours) at 5.5 km AGL occurs across all ensemble members. The blue contours are plotted for the following levels: 0.2, 0.4, 0.6, and 0.8 dB, with darker blues representing a higher frequency of occurrence of $Z_{DR} > 1$ dB. 126

4.10 Time series of the horizontal displacement of w_max at 1 km AGL from $\zeta_{sfc,max}$ for the a) MORR, b) NSSL2, and c) NSSL3 ensembles. Black lines represent the 50$^{\text{th}}$ percentile while the colorfill ranges from the 0$^{\text{th}}$ to the 100$^{\text{th}}$ percentile. 128

4.11 a) K_{DP} foot area area, b) cold pool area, c) maximum K_{DP}, and d) minimum cold pool temperature at T-0 at 1 km AGL the MORR (blue), NSSL2 (red), and NSSL3 (green) microphysics schemes. Black lines represent the range of the data; red horizontal lines show the location of the median; and the color-filled boxes range from the 25$^{\text{th}}$ to 75$^{\text{th}}$ percentile. 130

4.12 Horizontal cross-section of the frequency $\theta'_p <$ - 2 K (colorfill) and $K_{DP} > 1$ deg/km (contours) at 0.04 km AGL occurs across all ensemble members. The blue contours are plotted for the following levels: 0.2, 0.4, 0.6, and 0.8, with darker blues representing a higher frequency of occurrence of $K_{DP} > 1$ deg/km. 131

4.13 Time series of the cold pool area at 1 km AGL for the a) MORR, b) NSSL2, and c) NSSL3 ensembles. Black lines represent the 50th percentile while the colorfill ranges from the 0th to the 100th percentile. . . 132

4.14 Box plots of a) w_{max} and b) Z_{DR} column area at T-0 and 5.5 km AGL for the MORR (blue), NSSL2 (red), and NSSL3 (green) microphysics schemes. Black lines represent the range of the data; red horizontal lines show the location of the median; and the color-filled boxes range from the 25th to 75th percentile. 135

4.15 Time series of the K_{DP} foot area at 1 km AGL for the a) MORR, b) NSSL2, and c) NSSL3 ensembles. Black lines represent the 50th percentile while the colorfill ranges from the 0th to the 100th percentile. 138

4.16 Plot of the Z_{DR}-K_{DP} separation angle and distance for the MORR (red), NSSL2 (green), and NSSL3 (blue) ensembles at 0.04 km AGL. Scatter points represent the distance and angle for each ensemble member in the 30-min prior to tornadogenesis. The 0°angle is aligned with storm motion (SM). 140

4.17 Summary of the conclusions for each microphysics scheme for the updraft area, cold pool area, $V_{h,max}$, and the minimum cold pool temperature. . 142

Abstract

From 2011 to 2013, dual-polarization was implemented in the Weather Surveillance Radar 1988 Doppler (WSR-88D) network, enabling the identification of hydrometeor type, orientation, and size from radar data. With dual-polarization data, several features have since been identified as relevant to supercell intensification and development. Such features include, but are not limited to, the differential reflectivity (Z_{DR}) column, Z_{DR} arc, spectral differential phase (K_{DP}) column, K_{DP} foot, and correlation coefficient (ρ_{hv}) and Z_{DR} rings. These dual-polarization radar signatures provide critical insight into the microphysical and dynamical evolution of supercells, yet few studies have examined the temporal evolution of such signatures across multiple storms within a single outbreak or compared observations directly with high-resolution simulations of polarimetric radar data. This dissertation addresses both of these gaps through three integrated studies of the 24–25 May 2011 tornado outbreak.

In the observational component, polarimetric radar data from KOUN and KTLX were analyzed across six supercells — three tornadic and three nontornadic — during the outbreak. Tornadic supercells exhibited consistently larger mean areas across all polarimetric signatures (Z_{DR} column, Z_{DR} arc, and K_{DP} foot), had decreases in Z_{DR} column area after the genesis of an EF4+ tornado, and produced larger Z_{DR}-K_{DP} separation angles than their nontornadic counterparts. Differences between storm categories were maximized in the 15-minute window immediately preceding tornadogenesis, and a characteristic three-stage Z_{DR} arc development was identified across all tornadic supercells.

In the simulation component, tornadic supercells were modeled using Cloud Model 1 (CM1) with three bulk microphysics schemes — Morrison 2-moment (MORR), NSSL

2-moment (NSSL2), and NSSL 3-moment (NSSL3) — and a polarimetric forward operator. Three melting models were evaluated, and a novel Combined Melting Model (CMM) was developed that produces more physically realistic distributions of mixed-phase hydrometeors and removes artificial Z_{DR} artifacts above the freezing level present in prior approaches. Microphysics scheme comparisons revealed that the NSSL3 scheme best reproduced polarimetric signatures below the freezing level and the observed vertical evolution of near-surface rotation, while the MORR scheme most accurately captured signatures above the freezing level. However, the NSSL schemes produced the largest updraft areas both at 1 km AGL and above the freezing level, with the NSSL3 scheme producing both the warmest cold pools and smallest K_{DP} foot areas. Despite the differences across each microphysics schemes, all three schemes reproduced the orthogonal Z_{DR}–K_{DP} separation vector orientation characteristic of observed tornadic supercells.

These results demonstrate that bulk microphysics schemes can recreate key observed polarimetric–dynamical relationships in tornadic supercells, while also highlighting persistent challenges in representing mixed-phase hydrometeors and phase change processes in simulated storms. The observed component of this dissertation highlights the need for additional observations of the full lifecycle of supercells. The CMM and modified parameterized forward operator from the simulated component provide a computationally efficient framework for future studies of simulated polarimetric signatures which can be expanded to a range of convective modes and radar wavelengths.

Chapter 1

Introduction

Supercells produce a variety of hazards that negatively impact human life and property. Such hazards include hail, severe winds, and tornadoes. Of these hazards, tornadoes cause the greatest amount of loss of life, with the strongest tornadoes (EF4+) accounting for 67.5% of tornado-related deaths (Ashley, 2007). In addition to loss of life, large-outbreak events in which multiple strong tornadoes are produced also influence improvements to building codes in hopes of building more resilient architecture (e.g., Prevatt et al., 2012). It also cannot be understated how tornadoes impact the mental health of affected communities, with the exposure to the tornadic event, post-tornadic stressors, and prior experience with trauma all playing a role in producing negative mental health symptoms (Lee, 2022).

Tornadoes can arise in both linear and supercellular convection, though long-lived, significant tornadoes (EF3+) primarily arise from supercells (Davies-Jones et al., 2001). The general sequence of tornado formation in supercells is thought to involve the development of a rotating mid-level mesocyclone, the generation of near-surface vertical vorticity, and the convergence and amplification of near-surface vertical vorticity by a dynamically driven, intensifying low-level updraft that stretches vorticity to intensify the vortex (Davies-Jones, 2015; Fischer et al., 2024). However, a longstanding forecasting challenge is that the three-dimensional wind field is difficult to retrieve in real time. Features such as the updraft or vertical vorticity field are thus nearly impossible to apply to real-time tornado forecasting.

Polarization capabilities in radar were studied over a decade before their implementation into the Weather Surveillance Radar 1988 (WSR-88D) network in 2011 – 2013. Seliga and Bringi (1976) represents one of the first studies to assess the potential of using orthogonal polarizations to improve precipitation observations. Over the following decade or so, work by Sachidananda and Zrnić (1985, 1986, 1987), Balakrishnan and Zrnić (1990), and Jameson and Mueller (1985) improved our understanding of dual-polarization variables and their interpretation. These variables include differential reflectivity (Z_{DR}) – which is the difference in logarithmic reflectivity in the H and V polarizations – propagation differential phase (ϕ_{DP}) – which is the difference in the phase shift between the two polarizations – and the co-polar correlation coefficient (ρ_{hv}) – which is the correlation in the returned signal across the H and V polarizations. The range derivative of ϕ_{DP} along a certain distance, called the specific differential phase (K_{DP}), is often used as it is not impacted by attenuation and is not significantly affected by the presence of hail (Zrnić and Ryzhkov, 1996). These dual-polarization radar variables allow for inferences about hydrometeor type, size, and concentration (Vivekanandan et al., 1999; Straka et al., 2000). Kumjian (2013) provides an excellent summary of dual-polarization radar variables and how the magnitude of each variable varies for different hydrometeor types (see their Fig. A1 – A4).

There are multiple dual-polarization radar signatures in supercells that have been well documented. These signatures include, but are not limited to, the Z_{DR} column (Loney et al., 2002; Kumjian and Ryzhkov, 2008; Snyder and Ryzhkov, 2015; French and Kingfield, 2021), the Z_{DR} arc (Kumjian and Ryzhkov, 2008, 2009; Palmer et al., 2011; Dawson II et al., 2014; Dawson et al., 2015a; Van Den Broeke, 2017), the K_{DP} foot (Romine et al., 2008; Loeffler and Kumjian, 2018), the K_{DP} column (Hubbert et al., 1998; Loney et al., 2002), ρ_{hv} and Z_{DR} rings (Kumjian and Ryzhkov, 2008), and tornadic debris signatures (Ryzhkov et al., 2005; Van Den Broeke and Jauernic, 2014;

Bodine et al., 2014; Cross et al., 2023). Each of these signatures has been related back to supercell dynamics and, given the challenges in retrieving the three-dimensional wind field of supercells, dual-polarization radar signatures have been used to evaluate supercell development and tornado potential throughout the literature (Gibbs, 2016; Loeffler et al., 2020; Van Den Broeke, 2020; Wilson and Van Den Broeke, 2022; French and Kingfield, 2021; Segall et al., 2022). For example, the Z_{DR} column is an enhanced region of Z_{DR} ($Z_{DR} > 0$ dB) above the freezing level. This Z_{DR} enhancement is caused by relatively large, oblate supercooled drops that are lofted by the updraft (Kumjian et al., 2014). Thus, it is thought that the Z_{DR} column can serve as a proxy for the supercell updraft location and intensity. With the lack of information of the vertical wind field from single radar observations, the Z_{DR} column provides crucial insight into the updraft that would otherwise be unavailable to operational meteorologists.

Much of the previous literature on dual-polarization radar signatures has been focused on either climatological studies of radar signatures across numerous supercells from a variety of environments (e.g., Van Den Broeke, 2017; Loeffler et al., 2020; Homeyer et al., 2020; Van Den Broeke, 2020; Tuftedal et al., 2021; French and Kingfield, 2021; Segall et al., 2022; Healey and Van Den Broeke, 2023) or provide a case study of one supercell (e.g., Houser et al., 2015; Kurdzo et al., 2015; Bluestein et al., 2019; Wakimoto et al., 2020; Van Den Broeke et al., 2023). Klees et al. (2016) provides an example of one of the few studies that have looked at multiple supercells during the same event, though focus of the study was not the evolution of dual-polarization radar signatures. This leads into the first objective of this dissertation:

Objective 1: *To provide a detailed documentation of the time-evolution of dual-polarization radar signatures across multiple tornadic and nontornadic supercells during the same event.*

In addition to observations of dual-polarization radar signatures, other studies have

evaluated such signatures using supercell simulations. Numerical models provide a method of examining supercell dynamics and microphysics at higher spatiotemporal scales compared to most observations. However, in order to retrieve dual-polarization radar variables from model output, a forward operator and an appropriate melting model must be employed. With this in mind, numerous studies have developed various forward operators to produce realistic dual-polarization radar signatures (e.g., Shima et al., 2009; Ryzhkov et al., 2011; Matsui et al., 2019; Oue et al., 2020; Zhang et al., 2021). Most of these operators use the T-matrix method (Waterman, 1965) to calculate the desired polarimetric variables. Some of these emulators derive polarimetric variables directly from the output of the numerical model. Examples of these types of emulators include the Hebrew University Cloud Model (HUCM) developed by Ryzhkov et al. (2011) and the POLArimetric Radar Retrieval and Instrument Simulator (POLARRIS; Matsui et al., 2019). Other emulators, such as RSim (Mahre et al., 2020) and SimRadar (Cheong et al., 2017), employ realistic beam patterns and scanning strategies in addition to a forward operator. However, the addition of a beam pattern increases the computational expense of the emulator, making it less efficient for analyses of high-resolution data.

Given the computational expense of the T-matrix method, Zhang et al. (2021) developed a set of fitted equations that related the modeled drop size distribution parameters to the polarimetric variables and tested the output of the fitted equations with an observed case study. The parameterized forward operator developed in Zhang et al. (2021) showed good agreement with observations of a broad region of supercellular convection, though this was tested using model output on a 1.5 km x 1.5 km horizontal grid.

The performance of the parameterized forward operator is also modulated by the microphysics scheme of the model and the representation of melting processes. Different

methods of representing melting have been tested in convective storms (Jung et al., 2008; Dawson II et al., 2014; Johnson et al., 2016; Liu et al., 2024b), but no study has evaluated the impact that different melting models and microphysics schemes have on producing realistic polarimetric radar signatures at high spatial resolutions (< 100 m) and for tornadic supercells.

Currently, there is no set framework for comparing observations and simulations of supercells from a polarimetric signature perspective. Often, studies focus on either observations of polarimetric signatures (e.g., Tanamachi et al., 2012; Snyder et al., 2013; Wakimoto et al., 2020) or simulations of polarimetric signatures (e.g., Jung et al., 2010; Johnson et al., 2016), with a rare set of studies comparing both observations and simulations of polarimetric signatures (Dawson II et al., 2014; Zhang et al., 2021; Liu et al., 2024b). Out of the studies that have compared polarimetric observations and simulations, Dawson II et al. (2014) is one of the few studies that have looked at an isolated supercell. The comparison of the observed and simulated polarimetric signatures in Dawson II et al. (2014) was primarily qualitative, comparing the general size, structure, and magnitude of various signatures. Liu et al. (2024b) employed the use of contoured frequency by altitude diagrams (CFADs) as a more quantitative way of comparing observations and simulations. Furthermore, the simulations in these previous studies were performed on a horizontal grid of 1 km – 1.5 km and at one (or a select few) time step (Dawson II et al., 2014; Zhang et al., 2021; Liu et al., 2024b). Thus, few (if any) studies have performed a detailed, quantitative comparison of simulated and observed dual-polarization radar signatures over a continuous period of time and at high (< 100 m) spatial resolutions. Such comparisons are crucial for model improvement, as ensuring simulations replicate observations is important for the accuracy of the storm microphysics and dynamics the model attempts to replicate. This leads into the second set of objectives for this dissertation:

Objective 2a: *To use the Zhang et al. (2021) parameterized forward operator to evaluate which microphysics scheme produces realistic polarimetric signatures in tornadic supercells compared to radar observations.*

Objective 2b: *To evaluate the performance of different previously established melting models in producing realistic polarimetric signatures.*

Objective 2c: *To develop an improved method to parameterize mixed-phase hydrometeors in simulated supercells.*

In addition to using numerical models to evaluate supercell microphysics and polarimetric radar signatures, numerical models have been used to study the dynamics in tornadic supercells (e.g., Dahl, 2015; Coffer et al., 2017a; Orf et al., 2017; Yao et al., 2018; Flournoy et al., 2020; Vich and Romero, 2023; Fischer and Dahl, 2023). Such studies have been pivotal in our conceptual knowledge of tornadic supercells and have even influenced the trajectory of field campaigns (e.g., the results of Orf et al. (2017) helped formulate one of the key research questions in the Targeted Observation by Radars and UAS of Supercells field campaign (Houston et al., 2026)). However, supercell thermodynamics, dynamics, and microphysics are all interconnected. For example, changes in how evaporative cooling is represented in a model will alter the thermodynamic profile of the supercell. The resulting buoyancy changes will in turn alter portions of the supercell dynamics (i.e., the updraft and downdraft).

The impact different microphysics schemes have on storm dynamics has been documented in various studies (Snook and Xue, 2008; Dawson et al., 2010; Morrison and Milbrandt, 2011; Van Weverberg et al., 2012; Van Weverberg, 2013; Dawson et al., 2015b). Given the observed relationships between polarimetric signatures and supercell dynamics (Van Den Broeke, 2017; Snyder et al., 2017; French and Kingfield, 2021), it follows that changes in the model microphysics scheme will also alter how these polarimetric signature relationships are presented in supercell simulations. Healey and

Broeke (2025) evaluated the relationships between polarimetric radar signatures and storm dynamics in a simulated quasi-linear convective system for a single microphysics scheme. However, the impact that different model microphysics schemes have on the polarimetric signatures and their relationships to supercell dynamics is unknown for tornadic supercells. This leads into the final objectives of this dissertation:

Objective 3a: *To evaluate how different microphysics schemes impact tornado, updraft, and cold pool characteristics in tornadic supercells.*

Objective 3b: *To assess which model microphysics scheme best represents the relationship between polarimetric signatures and supercell dynamics seen in observations.*

This dissertation thus provides a unique analysis of dual-polarization radar signatures from observations and simulations. The selected case for analysis is the 24 – 25 May 2011 tornado outbreak across central Oklahoma. This outbreak provides observations of multiple nontornadic and tornadic supercells. Also, a sounding taken from the supercell that produced the prolific El Reno tornado (Orf et al., 2017) allows for the initialization of simulations of the supercells during the outbreak. Chapter 2 covers the observed case study and addresses Objective 1; Chapter 3 details the parameterized forward operator, melting models, and simulation configuration and addresses Objectives 2a-2c; and Chapter 4 uses the simulation framework from Chapter 3 to address Objectives 3a and 3b. Finally, Chapter 5 will provide a summary of the findings from the work herein.

Chapter 2

A Case Study of Polarimetric Radar Signatures Across Tornadic and Nontornadic Supercells in a Volatile Environment During the 24 – 25 May 2011 Outbreak

2.1 Introduction

Supercells produce some of the most intense and long-lived tornadoes, which cause significant destruction of life and property. Although there have been improvements to tornado forecasting, such as the implementation of the WSR-88D network, forecast skill for tornadoes has shown limited improvement over the past decade (Brooks and Correia, 2018). With operational dual-polarization radar networks (Doviak et al., 2000), inferences about the microphysical and dynamic evolution of supercells can be made in real-time (e.g., Kumjian and Ryzhkov, 2008; Kumjian et al., 2010; Van Den Broeke, 2017). Differential reflectivity (Z_{DR}) helps determine the orientation and size of the scatterer, the specific differential phase (K_{DP}) provides information about

the liquid water content, and the correlation coefficient (ρ_{hv}) indicates the diversity of scatterers within a radar volume. Using these fields, various polarimetric signatures are common to supercells: the Z_{DR} arc (Kumjian and Ryzhkov, 2008, 2009; Van Den Broeke, 2017), K_{DP} foot, Z_{DR} column (Loney et al., 2002; Kumjian and Ryzhkov, 2008; Snyder et al., 2015), and tornado debris signature (TDS; Ryzhkov et al., 2005; Bodine et al., 2013; Van Den Broeke and Jauernic, 2014) when applicable. Each of these signatures has a relationship to supercell or tornado dynamics. The Z_{DR} arc area scales with the intensity of the low-level, storm-relative winds (Kumjian and Ryzhkov, 2009; Dawson et al., 2015a); the magnitude of the K_{DP} foot indicates the amount of liquid water in the radar volume and is related to negative buoyancy (Carlin and Ryzhkov, 2019); the TDS height can indicate tornadic intensity (Cross et al., 2023); and the Z_{DR} column can be used as a proxy for updraft location, strength, and width (Kumjian and Ryzhkov, 2008; Kumjian et al., 2014; Snyder et al., 2015; French and Kingfield, 2021). Of these four signatures, only the TDS cannot be used across tornadic and nontornadic supercells since a tornado must be present for a TDS to exist.

Within the subset of the literature examining differences between tornadic and nontornadic supercells, some studies have investigated how well dual-polarization radar signatures distinguish between these types of supercells in relatively large sample sizes (dozens or hundreds of supercells). Given the correlation of the Z_{DR} column with a storm's updraft properties, the Z_{DR} column area, width, and height are commonly studied signatures (Van Den Broeke, 2017; Snyder et al., 2017; Van Den Broeke, 2020; French and Kingfield, 2021). Van Den Broeke (2017) looked at Z_{DR} columns in nontornadic and tornadic storms and found that EF2+ storms had taller Z_{DR} columns than storms that produced weak (EF0 only) tornadoes (Van Den Broeke, 2017). Snyder et al. (2017) looked at similar features in a simulated framework, noting that larger Z_{DR} columns were present in cases with stronger vertical wind shear. A larger sample

size of 198 Z_{DR} columns in supercells was analyzed by French and Kingfield (2021). This time, however, French and Kingfield (2021) analyzed the Z_{DR} column area rather than height. They showed that, much like the Z_{DR} column heights in Van Den Broeke (2017), nontornadic supercells had small Z_{DR} column areas (< 20 km^2) and EF3+ supercells had larger areas than EF1–2 supercells (French and Kingfield, 2021). Finally, Van Den Broeke (2020) showed that, in the 30-min period prior to tornadogenesis, tornadic supercells had larger Z_{DR} column depths and sizes above the freezing level.

Other, non-dual-polarization proxies for updraft strength and tornado intensity exist and are useful as well, such as mesocyclone width and overshooting tops (e.g., Marion et al., 2019; Sessa and Trapp, 2020). While there appears to be forecast utility in these signatures, some questions remain since these updraft proxies probably better represent middle- and upper-level updrafts rather than low-level updrafts directly linked to tornadogenesis processes.

Polarimetric signatures within the lower levels of the supercell (< 2 km AGL) have also been shown to distinguish between tornadic and nontornadic supercells. The Z_{DR} arc tends to have larger variability in its width, higher dB values in EF2+ tornadoes, and have larger sizes in tornadic supercells (Van Den Broeke, 2017, 2020). The Z_{DR} -K_{DP} separation angle is another metric that can distinguish between nontornadic and tornadic supercells (Loeffler et al., 2020; Homeyer et al., 2020; Wilson and Van Den Broeke, 2022). Within each ensemble in Loeffler et al. (2020) and Homeyer et al. (2020), supercells had separation angles 90° to the right of storm motion. In Wilson and Van Den Broeke (2022), the tornadic supercells had separation angles slightly lower than what was seen in Loeffler et al. (2020) and Homeyer et al. (2020), with tornadic supercells having separation angles larger than 40°. The orthogonal orientation relative to storm motion is hypothesized to benefit tornadogenesis since the K_{DP} foot and associated cooling are pushed northward and away from the storm's primary updraft

(Loeffler et al., 2020). Furthermore, Homeyer et al. (2020) found a ρ_{hv} minimum near the Z_{DR}–K_{DP} separation, with the minimum overlapping with the K_{DP} enhancement region in nontornadic supercells.

The aforementioned studies examined tornado intensity and potential using dual-polarization radar variables for supercells across numerous cases and environments. However, few studies have documented the time-evolution of polarimetric signatures during the same event. In fact, only one known study has examined observations of dual-polarization radar signatures across numerous nontornadic and tornadic supercells during the same event (Healey and Van Den Broeke, 2023). Healey and Van Den Broeke (2023) examined nontornadic and tornadic supercell pairs occurring within 1 hour of each other with similar environmental variables. Healey and Van Den Broeke (2023) then looked at the average areal extent of the Z_{DR} arc, Z_{DR} column, and hail fallout along with the K_{DP} foot-Z_{DR} arc separation distance and angle during the 30 min window before tornadogenesis, or max rotation for nontornadic supercells. The primary distinguishing features between tornadic and nontornadic supercells were the K_{DP} foot-Z_{DR} arc separation distance and Z_{DR} column area. The remaining signatures (Z_{DR} arc, hail fallout, and K_{DP} foot-Z_{DR} arc separation angle) were similar across tornadic and nontornadic supercells, emphasizing how the environment can play an important role in the evolution of these features.

Much of the previous literature has compared 30-min averages of polarimetric radar signature characteristics (e.g., Healey and Van Den Broeke 2023), but few studies have examined the temporal evolution of dual-polarization radar signatures across nontornadic and tornadic supercells during the same event and on longer timescales than 30 min. Van Den Broeke et al. (2023) provided a polarimetric analysis of a long-lived supercell on 10–11 December 2021, covering the genesis, maintenance, and dissipation of the supercell's EF4 tornado, and Van Den Broeke (2020) provided a comparative

analysis in the 30-min window prior to tornadogenesis between tornadic and nontornadic supercells in different environments. Klees et al. (2016) evaluated two supercells during the same event, but the analysis did not include observations of the polarimetric signatures.

This study provides an analysis of the time evolution of polarimetric signatures across tornadic and nontornadic supercells during the 24 – 25 May 2011 outbreak. Specifically, the time evolution and structure of the Z_{DR} column, K_{DP} foot, Z_{DR} arc, and Z_{DR} arc-K_{DP} foot separation vector are analyzed across 3 tornadic and 3 nontornadic supercells. Section 2.2 details the case selected for this study and the methods used for dual-polarization signature identification. Section 2.3 outlines the results of this analysis, while section 2.4 provides a summary of this paper's contents.

2.2 Data and Methodology

The 24 – 25 May 2011 tornado outbreak was a prolific event, with 5 tornadic supercells across Oklahoma identified by the NWS (Fig. 2.1), and tornadoes ranging from EF0 – EF5. This specific outbreak was chosen because of the high concentration of supercells (tornadic and nontornadic) during the same event that were visible by a WSR-88D. Furthermore, the 24 – 25 May 2011 outbreak has been well-documented by mobile dual-polarization and phased array radars (Houser et al., 2015; French et al., 2015; Tanamachi et al., 2015), allowing for a comparison of the polarimetric signatures with the updraft dynamics and mergers analyzed by past work.

Polarimetric radar data from KOUN and Doppler velocity data from KTLX, KFDR, and KOUN were used to analyze each supercell on 24 – 25 May 2011. The KTLX and KFDR velocity data were corrected using the region-based dealiasing from the Python ARM Radar Toolkit (Py-ART) (Helmus and Collis, 2016). The quality of the

corrected velocity data was also manually inspected after the region-based dealiasing. The Nyquist velocity for the dealiasing was taken from the NEXRAD Level II files and was 26.1 m s^{-1}. Also, the Z_{DR} field was calibrated by comparing the Z_{DR} field above the freezing level (approximately 4.5 km AGL) to the expected value of Z_{DR} for dry snow (0.2 dB). The correction resulted in 0.1 dB added to the Z_{DR} field and was done before any gridding or feature identification was performed.

Supercells on 24 – 25 May 2011 were identified using WSR-88D and NWS storm data. Tornadic storms were selected using NWS storm data (NOAA, 2011) while nontornadic storms were identified based on the presence of a mesocyclone at 0.5° from KTLX or KFDR and polarimetric radar signatures common to supercells at 1.5 km AGL from KOUN (e.g., some combination of a Z_{DR} arc, K_{DP} foot, and Z_{DR} column). To identify a mesocyclone, the center of rotation was manually identified. Then, since mesocyclones have average widths between 3-8 km (Markowski and Richardson, 2010), VROT was calculated from the maximum and minimum radial velocities within an 8 km x 8 km box centered on the manually identified center. For polarimetric signatures, if one or more were present in a storm, that storm was classified as a supercell and included in the analysis. Table 2.1 gives a list of each identified storm. Supercell A and E were not analyzed as they were too far from KOUN to observe polarimetric data at 1.5 km AGL and, in the case of supercell E, had poor data quality just before and during the supercell's tornado. Fig. 2.1 shows the path and location of each tornadic supercell within Oklahoma.

$$VROT = \frac{V_{max\ outbound} - V_{max\ inbound}}{2} \tag{2.1}$$

It should be noted that the use of tornado reports approximates the time of tornadogenesis. Thus, genesis likely occurred between T-5 (5 minutes before tornadogenesis)

and T (time of tornadogenesis) rather than at T for some cases. Furthermore, using maximum VROT as a comparison point for the nontornadic storms approximates genesis failure. It is also possible that failure occurred right after maximum VROT or right before. It is impossible to achieve high accuracy in genesis or genesis failure with the coarse time resolution of KOUN and the lack of 3D wind data, making these approximations best guesses based on the available data.

Table 2.1: Table of supercells from 24 – 25 May 2011. Supercells with an asterisk were not analyzed due to a lack of data or distance from KOUN. The time window for each TOR was taken from NWS storm data. Distance from KOUN was calculated at 5.0 km AGL from the gridded radar data.

Supercell Identifier	TOR?	Time of TOR (UTC)	Average Distance from KOUN (km)	Average Beam Height at 0.5° (km)	Average Beam Height at 19° (km)
Supercell A*	Y	EF3: 20:20 – 20:43 EF0: 20:47 – 20:51	152.9	3.17	52.78
Supercell B	Y	EF3: 20:31 – 20:46 EF5: 20:50 – 22:35 EF0: 21:37 - 21:38 EF2: 22:50 - 23:05	88.7	1.67	30.49
Supercell C	Y	EF4: 22:06 – 23:01 EF0: 22:45 – 22:46	65.8	1.25	22.64
Supercell D	Y	EF4: 22:26 – 23:05 EF1: 23:02 EF2 23:36 – 23:39	74.0	1.39	25.45
Supercell E*	Y	EF1: 00:30 – 00:45	158.6	3.33	54.78
Supercell F	N	N/A	120.6	2.35	41.51
Supercell G	N	N/A	134.2	2.68	46.25
Supercell H	N	N/A	140.0	2.83	48.27

Tornadogenesis times for each supercell were defined using NWS storm data (the first time listed in Table 2.1). For the nontornadic supercells, the maximum rotational velocity (VROT, Eq. 2.1) at 0.5° from KTLX and KFDR was used as a proxy for genesis failure. When relevant, the x- and y-coordinates of the KTLX and KFDR

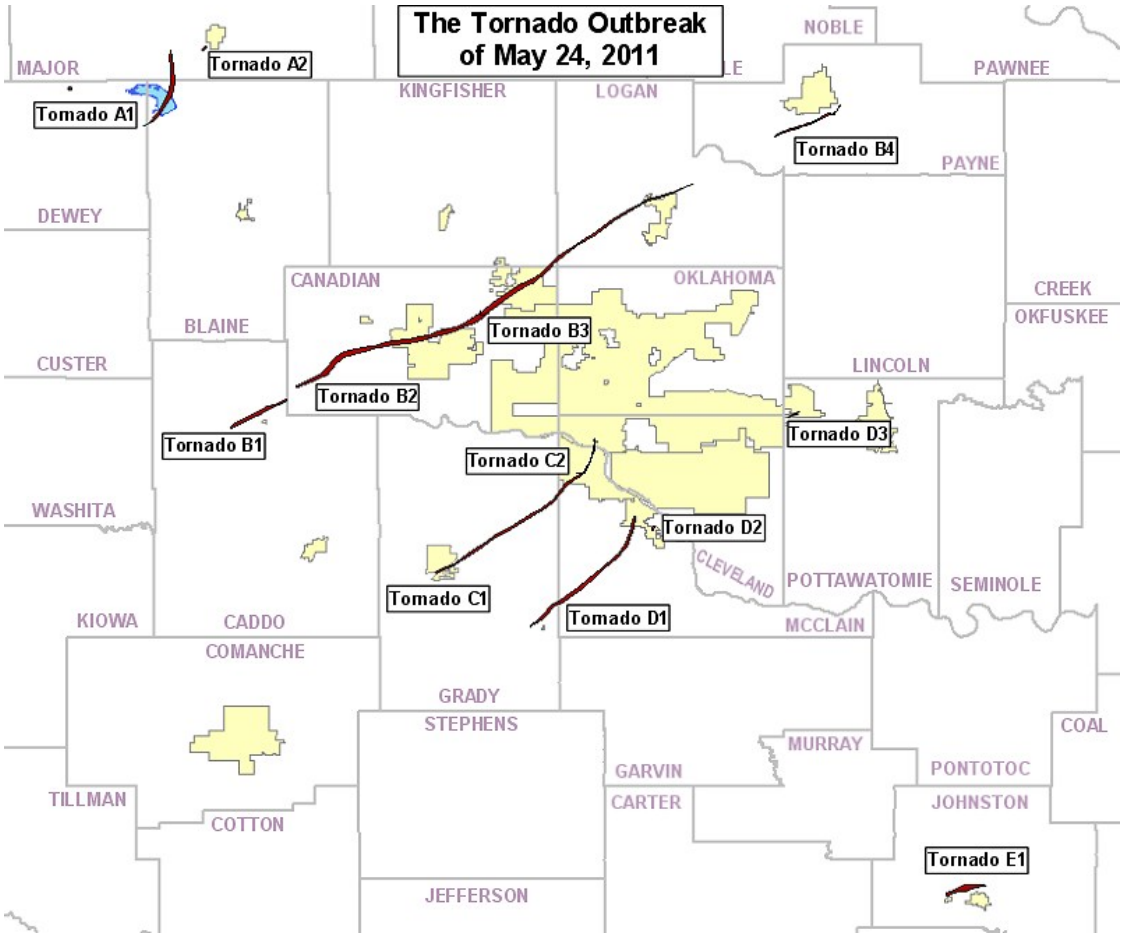


Figure 2.1: Tornado damage path overview from the National Weather Service summary of the 24 – 25 May 2011 outbreak.

radars were subtracted from the x- and y-coordinates of the KOUN radar so that KOUN was at the origin of the KTLX and KFDR data. This adjustment was made so that the mesocyclone locations from KTLX and KFDR could be compared with the polarimetric radar data from KOUN.

2.2.1 Polarimetric Signature Identification

To analyze dual-polarization radar signatures, the Z_{DR} arc, Z_{DR} column, and K_{DP} foot had to be identified first. First, K_{DP} was calculated using Py-ART's Vulpani algorithm

(Vulpiani et al., 2012). Then, data from KOUN were gridded using Py-ART's Barnes interpolation to a 1 km x 1 km x 0.5 km grid to keep the analysis height consistent across all supercells.

With the gridded KOUN data, the center of each polarimetric feature was manually selected at each time step. A 20 km x 20 km analysis box was then centered on the selected point, similar to what was done in Loeffler et al. (2020). Each grid point within the analysis box was passed through a simple detection algorithm to see which bins represented the feature and which did not. The algorithm's criteria varied depending on the polarimetric radar signature being analyzed. Two other methods for detecting polarimetric signatures were tested to assess their sensitivity: manually tracing the boundaries of each signature and using a larger analysis box (40 km x 40 km). The previously mentioned thresholds were then applied to all locations within the traced boundary or the larger analysis box. All locations that met the threshold criteria were then defined as part of the polarimetric feature under analysis. The larger analysis box better captured larger features (Z_{DR} arcs in particular), but would sometimes detect high Z_{DR} regions in nearby cells for smaller storms. The trace method captured signatures well and had less room for error than the 40 km x 40 km box method when detecting features, but it was time-consuming for multiple long-lived supercells and more subjective. The trace method and box methods (both the 40 km x 40 km and 20 km x 20 km box methods) showed similar temporal trends in the areal values of polarimetric signatures (now shown). Given the consistency in temporal trends across methods, the smaller (20 km x 20 km) analysis box was selected to remain consistent with the methodology used in past work.

In the gridded data, there are instances of missing data that especially impact supercells further away from KOUN. Any missing data that fell within the analysis box was not flagged as part of the observed signature. As such, the calculation of

the area of polarimetric signatures could be under estimated in instances where the missing data masked portions of the signature. Supercell H was most impacted by missing data, so the reported areas of signatures in this supercell are likely slightly larger than what is presented.

The Z_{DR} column was defined as a region of enhanced Z_{DR} ($>$ 1.0 dB) at 5.5 km AGL. The freezing level was defined as z = 4.5 km AGL in the El Reno reanalysis sounding, as reported in Orf et al. (2017), placing the analysis of the Z_{DR} column 1.0 km above the freezing level (AFL). The Z_{DR} arc was defined as a region of enhanced $Z_{DR} > 3$ dB and the K_{DP} foot was defined as a region of enhanced K_{DP} ($> 1.5^{\circ}$ km^{-1}) at 1.5 km AGL. A ρ_{hv} threshold of 0.93 was used in the identification of each signature to help remove non-meteorological scatterers as done in Loeffler and Kumjian (2018). The 1.5-km analysis height of the Z_{DR} arc and K_{DP} foot was chosen to ensure that close and far-range supercells can be compared, while remaining within the expected altitudes of the signatures. The 1.5° km^{-1} threshold is lower than the 3° km^{-1} threshold used for K_{DP} foot detection in other studies (e.g., Loeffler and Kumjian, 2018; Loeffler et al., 2020). Interpolation of the K_{DP} data to a Cartesian grid may have smoothed the peaks in K_{DP} that are often seen in supercells. Thus, a lower threshold was used to help distinguish between the K_{DP} foot and the rest of the storm. Finally, the K_{DP} foot-Z_{DR} arc separation angle and distance calculation was computed based on Loeffler and Kumjian (2018) with the same bin threshold ($N_g = 10$).

2.3 Results

To compare tornadic and nontornadic supercells, the evolution of the Z_{DR} column, Z_{DR} arc, K_{DP} foot, and Z_{DR} -K_{DP} separation angle and distance were analyzed during storm development up to the time of tornadogenesis for the tornadic supercells or

mesocyclone intensification for the nontornadic supercells. The time of the first radar echo, which we define as $Z_H > 20$ dBZ at an elevation angle of 0.5°, for each supercell is given in Table 2.2. Since the time of VROT_{max} was obtained from KTLX, the KTLX radar was used to analyze the first echo of each supercell for a more accurate time comparison. Additionally, the time of VROT_{max} or the time of the genesis of the first tornado within a given supercell is also provided in Table 2.2. Subtracting the time of tornadogenesis from the first echo time provides the longevity of the supercell before reaching VROT_{max} (or genesis of the first tornado).

Supercell B and F initiated within 30 min of each other, with supercell F residing approximately 40 km north of supercell B (not shown). Despite their proximity, supercell B persisted for almost twice as long as supercell F before producing its first tornado (Table 2.2). Meanwhile, supercell F produced no reported tornado. At 2031 UTC (approximately 30 min after VROT_{max} was achieved by supercell F), supercell F was situated between supercell B and A (Fig. 2.2). At 2106 UTC, supercell F split into two distinct cells (not shown). The left split interacted with the remains of supercell A, while the right split dissipated into the northern edge of supercell B. It is quite possible that the position of supercell F between two already established, tornadic supercells dampened its tornadic potential. Finally, the remaining supercells (C, D, G, and H) had similar longevities before tornadogenesis or VROT_{max} (Table 2.2).

Table 2.2: Time of first radar echo (defined as $Z_H > 20$ dBZ) as seen by KTLX at an elevation angle of 0.5°, time of the genesis of the first tornado in the supercell or time of VROT_{max}, and the difference between the tornadogenesis and first echo times.

Supercell Identifier	Time of First Echo (UTC)	Time of Tornadogenesis (UTC)	Analysis Window (hr)
Supercell B	1824	2031	2.1
Supercell C	2027	2206	1.7
Supercell D	2044	2226	1.7
Supercell F	1857	2005	1.1
Supercell G	2019	2208	1.8
Supercell H	2205	2327	1.4

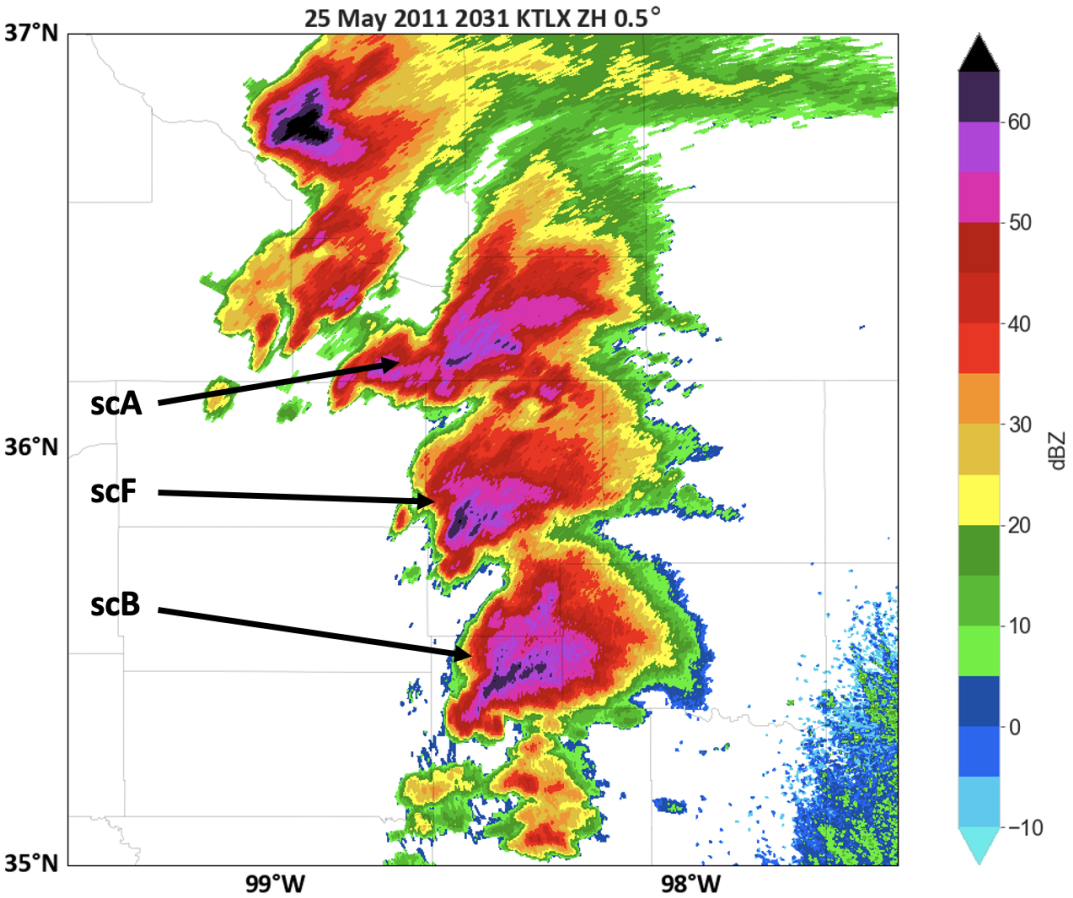


Figure 2.2: Horizontal cross-section of ungridded Z_H from KTLX at 2031 UTC and an elevation angle of 0.5°.

We did not explicitly quantify environmental spread, as in Healey and Van Den Broeke (2023), because this study focused on analyzing the time evolution of polarimetric signatures across supercells during the same event. However, polarimetric radar signatures are influenced by their environment. As such, we analyzed ECMWF Reanalysis v5 (ERA5) data and the Storm Prediction Center (SPC) mesoanalysis archive to quantify the environment near each identified supercell.

Using the ERA5 data, values of dewpoint temperature at the surface, 0 – 6 km shear, and 0 – 1 km shear were compared across supercells from 2000 UTC 24 May 2011 to 0000 UTC 25 May 2011 (Table 2.3). Values were taken in the near-storm environment, which was defined to be 40 km from the storm's updraft (approximated to be near the mesocyclone), within the inflow region as in Parker (2014), and at the closest timestep before a reported tornado or maximum rotational velocity (VROT) for the nontornadic supercells (Table 2.3). Since there was no way to obtain a specific point value through the mesoanalysis archive data, a range of values is provided in Table 2.3. The range of environmental values was obtained by finding the minimum and maximum contours in central Oklahoma.

While there is good agreement between the environmental parameters from ERA5 and SPC mesoanalysis, the ranges of values differ across the two data sources. These differences are because the ERA5 values come from the near-storm environment, while the SPC mesoanalysis represents the broad, synoptic-scale environment supercells moved into during the outbreak. Furthermore, the ERA5 data are on a 0.25°-by -0.25° grid, while the SPC mesoanalysis data are on a 13-km horizontal grid, further explaining the differences in the values in Table 2.3.

Comparing the ERA5 and SPC mesoanalysis values to the values from the proximity Rapid Update Cycle (RUC) soundings in Thompson et al. (2003), the environment was well primed for the production of significant tornadoes (Table 2.3). The minimum

Table 2.3: Environmental parameters from the near-storm environment taken from ERA5 and SPC Mesoanalysis. Values from the NWS for supercells and values for significant tornadoes from Thompson et al. (2003) are provided for comparison. Values for each supercell were taken from the closest time step before the first tornado or maximum VROT.

Environment Parameters	NWS Supercell Threshold	Thompson et al. (2003) SIG TOR Range	ERA5 Range	ERA5 Mean	SPC Mesonalysis Range
SBCAPE (J/kg)	> 1000		1458 – 3737	2357	2000 – 4000
MLCAPE (J/kg)		1059 – 3683			2000 – 4000
SFCCIN (J/kg)			8 – 96	33	25 – 100
0 – 1 km Shear (m s^{-1})	> 7 – 10	5.8 – 16.2	6 – 17	11	10 – 30
0 – 6 km Shear (m s^{-1})	> 15 – 21	18.3 – 31.8	28 – 36	33	40 – 50

values from the ERA5 and the SPC mesoanalysis ranges also do not always correspond to the nontornadic supercells. The lowest SBCAPE (1458 J kg^{-1}) lies within the inflow of supercell C, which produced a long-track EF4. Conversely, one of the largest values of SBCAPE occurred near the nontornadic supercell F. Furthermore, 0 – 1 km and 0 – 6 km vertical wind shear generally increased from north to south, meaning higher values of wind shear did not strictly correlate with the supercells that produced strong (EF3+) tornadoes. The most southern supercells (supercells G, H, and E) had the highest 0 – 1 km shear and were either nontornadic or produced weak tornadoes (EF0-1).

2.3.1 Z_{DR} Column

To allow for a more accurate comparison of the temporal evolution of the Z_{DR} column area of each supercell, each time series ends at the time of tornadogenesis (VROT_{max}).

The time of tornadogenesis, rather than storm initiation, was used, as KOUN was unable to observe the initiation of all supercells. The time of tornadogenesis (or VROT_{max}) provides a point of comparison that was observable by KOUN and defined by the NWS storm reports (or VROT_{max} values).

It should be noted that, for both supercells B and F, the genesis of the Z_{DR} column was not observed by KOUN. Thus, it is likely that the Z_{DR} column in both supercell B and F began earlier than what is shown in Fig. 2.3a,b. Meanwhile, the earlier stages of the Z_{DR} column for supercells C, D, and G were better captured by KOUN. Supercells C, D, and G – which all initiated within 30 min of each other – each had Z_{DR} columns which appeared approximately 80 min before tornadogenesis (VROT_{max}) and 98 – 105 min after storm initiation. Between supercells C, D, and G, the Z_{DR} column area of supercell G remained relatively consistent from T-80 to T-0 (minus a drop in column area at T-24) while the tornadic supercells C and D had column areas that steadily increased from 20 – 40 km^2 to 70 – 110 km^2 from T-80 to T-0.

The means of the column area from T-30 to T-0 are provided in Fig. 2.4. The average Z_{DR} column area differed by only 12 km^2 between tornadic (60 km^2) and nontornadic (52 km^2) supercells (Fig.2.4a), with supercell C reaching the largest value (104 km^2) at the genesis of its EF4 tornado (Fig.2.3a). This result follows that of French and Kingfield (2021) and Healey and Van Den Broeke (2023), which found that tornadic supercells had larger column areas than their nontornadic counterparts. Also, even though the dataset in Healey and Van Den Broeke (2023) did not include prolific events as what is assessed in this study, the difference of the means between the tornadic and nontornadic supercells in Healey and Van Den Broeke (2023) (6.9 km^2) is similar to the difference (12 km^2) seen in the 24 May 2011 supercells.

The evolution of the Z_{DR} column was also assessed using a higher Z_{DR} threshold (> 3 dB). Larger values of Z_{DR} within the column could suggest the updraft has lofted

larger drops, potentially indicating stronger vertical motions within the storm and the location of the updraft core. Most of the supercells had column areas between 0 – 20 km^2 between T-80 and T-0 (Fig. 2.3b). The exceptions were supercell B and supercell D, both of which had column areas exceeding 20 km^2 at 1 time step. Using the higher ZDR threshold, the average column areas across the tornadic and nontornadic supercells differed by 5 km^2 (Fig. 2.4b). Once again, the tornadic storms had slightly larger column areas (10 km^2) than the nontornadic storms (5 km^2). Given the lack of a clear distinction between the tornadic and nontornadic column areas, and that Z_{DR} columns have been used as a proxy for updraft width and location (Kumjian and Ryzhkov, 2008; Kumjian et al., 2014; Snyder et al., 2015; French and Kingfield, 2021), it is possible that the development and size of the mid-to-upper level updraft were similar across the supercells on 24 – 25 May 2011.

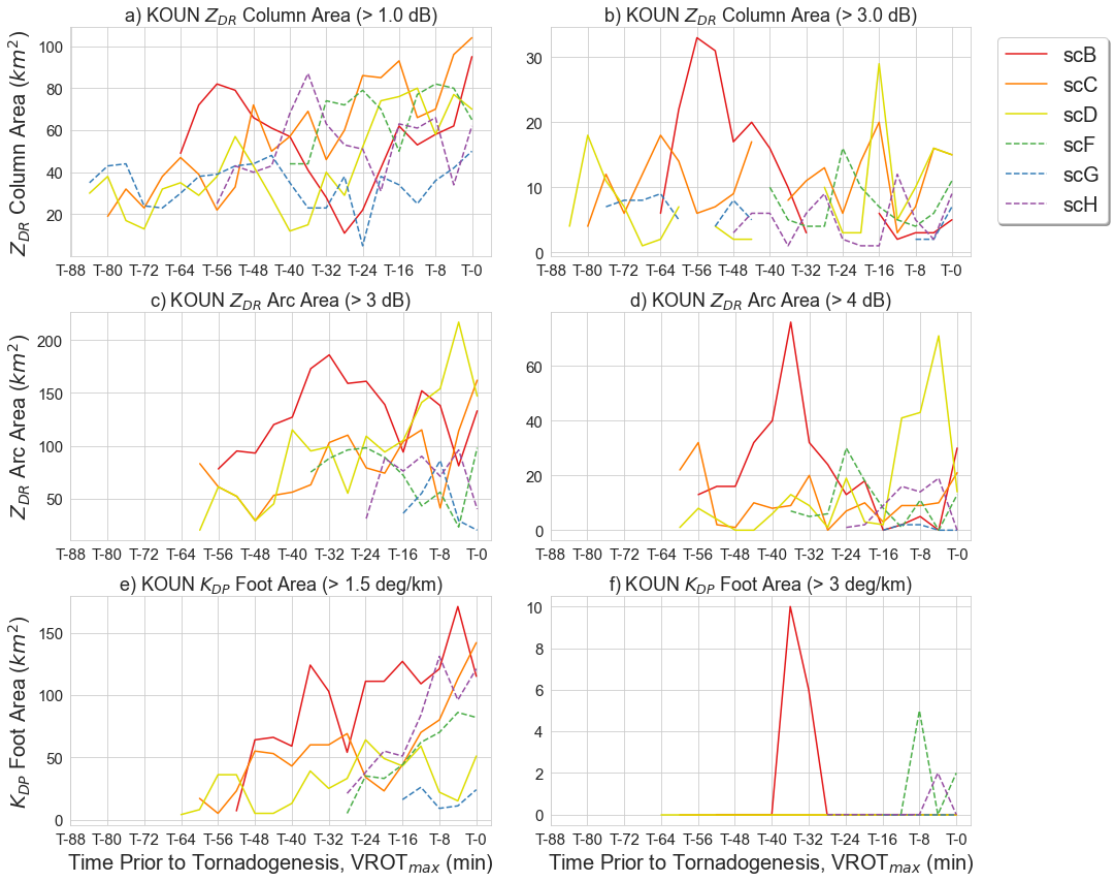


Figure 2.3: Temporal evolution of the Z_{DR} column (a,b), Z_{DR} arc (c,d), and K_{DP} foot (e,f) prior to tornadogenesis (VROT$_{max}$). Solid lines represent the tornadic supercells, while dashed lines represent the nontornadic supercells.

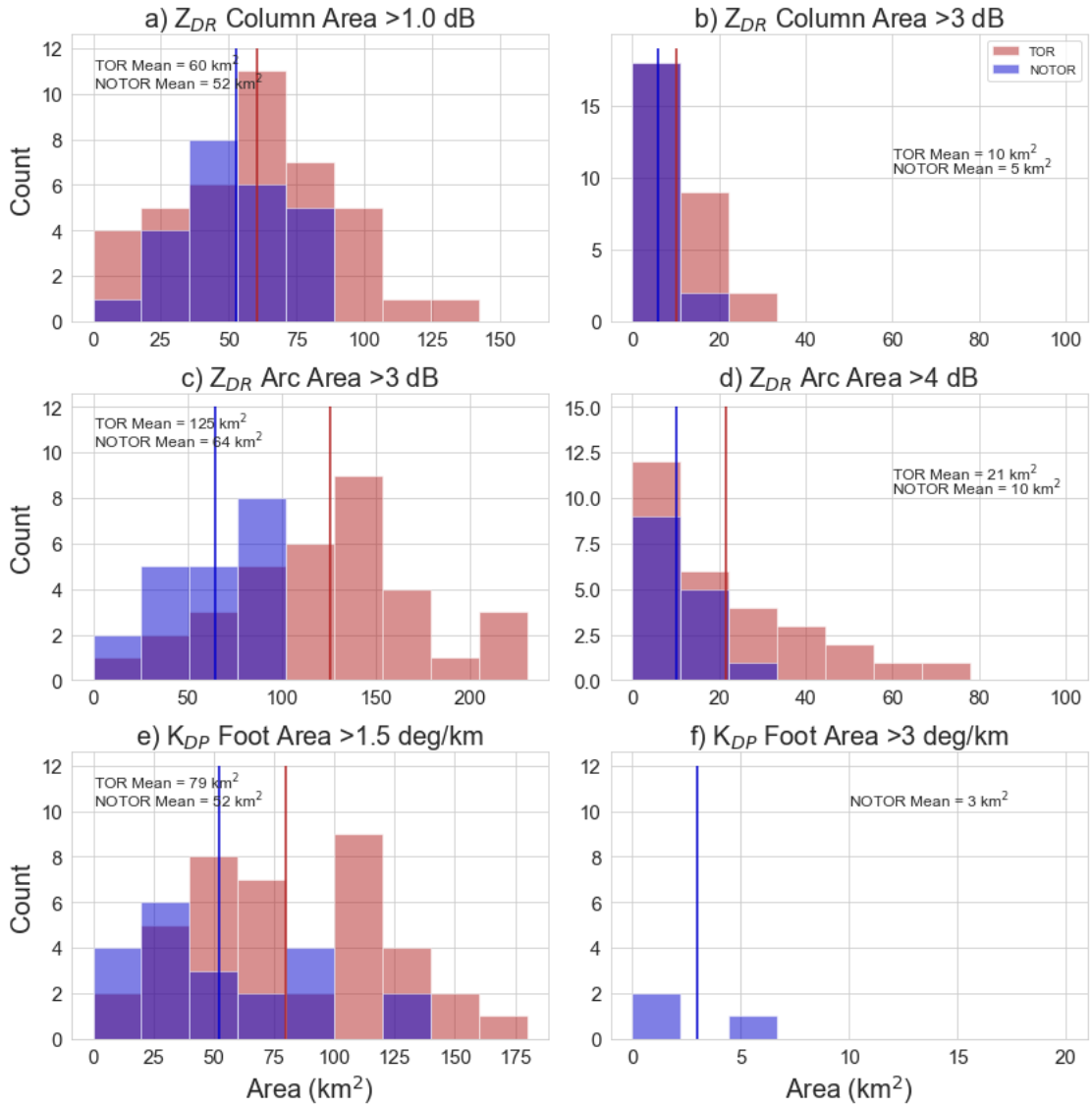


Figure 2.4: Histograms of the area values for the Z_{DR} column (a,b), Z_{DR} arc (c,d), and K_{DP} foot (e,f) from T-30 to T-0 for the nontornadic (blue) and tornadic (red) supercells.

The structural evolution of the Z_{DR} column is given in Figs. 2.6 and 2.7. Approximately 50 to 60 min before tornadogenesis, the Z_{DR} column in the tornadic supercells was situated in the western portion of the supercell (Fig. 2.6a,d,g). Supercell B had multiple Z_{DR} columns throughout the supercell lifecycle (Fig. 2.6a). Given the multiple

updraft objects shown in Tanamachi et al. (2015) for supercell B later in its lifecycle, it is likely that these Z_{DR} columns represent the early onset of multiple updraft pulses.

At T-0, the Z_{DR} columns in supercells C and D formed a partial ring (Fig. 2.6e,h). In these two supercells, the first tornado to form was an EF4 tornado. For supercell B, a partial Z_{DR} ring was not present at T-0, but a full Z_{DR} ring later formed at T+8 (Fig. 2.6b,c). In supercells C and D, 8 min after tornadogenesis, the Z_{DR} column area and magnitude decreased (Fig. 2.5). This was not the case for supercell B, which had a column area at T+8 that was similar (if not larger) than the area at T-0 (Fig. 2.6b). It should be noted that the first tornado in supercell B was not the strongest. At 2031 UTC, supercell B formed an EF3 tornado. The stronger EF5 tornado did not form until 2050 UTC (as seen by KOUN). After 2050 UTC, the column area and magnitude in supercell B decreased (Fig. 2.5). Thus, each of the long-lived, EF4+ tornadoes was characterized by a decrease in Z_{DR} column area and magnitude after tornadogenesis.

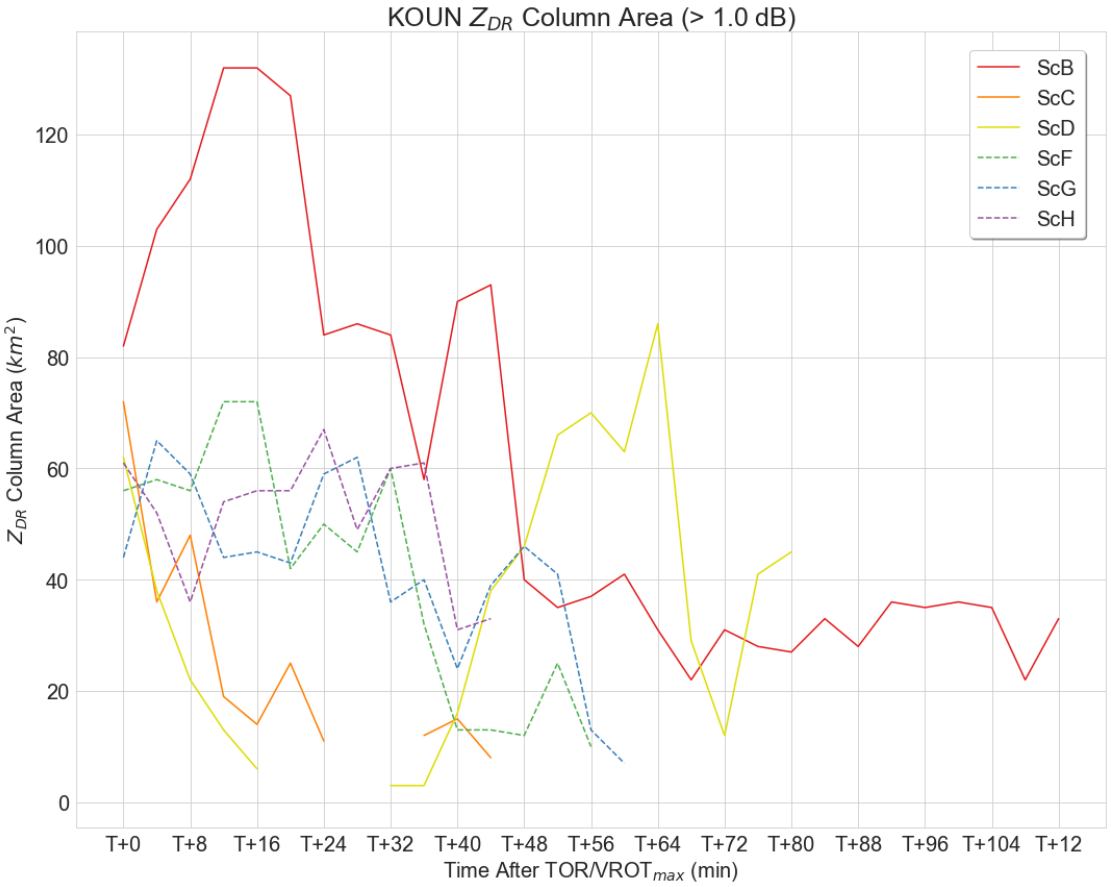


Figure 2.5: Time series of Z_{DR} column area starting at the time of the genesis of the last reported tornado or VROT$_{max}$. Solid lines represent the tornadic supercells while the dashed lines represent the nontornadic supercells.

Similar to the tornadic supercells, the nontornadic supercells had Z_{DR} columns at T-45 to T-52 in the western portion of the storm (Fig. 2.7a,d,g). The location of the column in the western corner of the storm from 45 to 60 min before tornadogenesis (or VROT$_{max}$) was consistent across all supercells on 24 May 2011. Also, like supercell B, supercell F also exhibited multiple Z_{DR} columns at T-45 (Fig. 2.7a). Given supercell B and F initiated within the same 30 min window (Table 2.2) and within 40 km of one another, the presence of multiple Z_{DR} columns – and potential updraft pulses – could have been a by-product of the environment between 1800 – 1900 UTC.

At T-0, the nontornadic supercells did not exhibit partial Z_{DR} rings (Fig. 2.7b,e,h). For supercells G, the Z_{DR} column remained in the western portion of the supercell at T-0 (Fig. 2.7e). Supercell F had a region of lowered Z_{DR} west of the column at T-0, while supercell H had a column with $Z_{DR} > 3$ dB (Fig. 2.7b,h). The nontornadic supercells did have partial – and in some cases complete – Z_{DR} rings, but they occurred after T+8. Finally, the area of the column did not drastically decrease after T-0 in the nontornadic supercells (Fig. 2.5). In fact, the column area either remained quasi-constant until T+32 (Fig. 2.5).

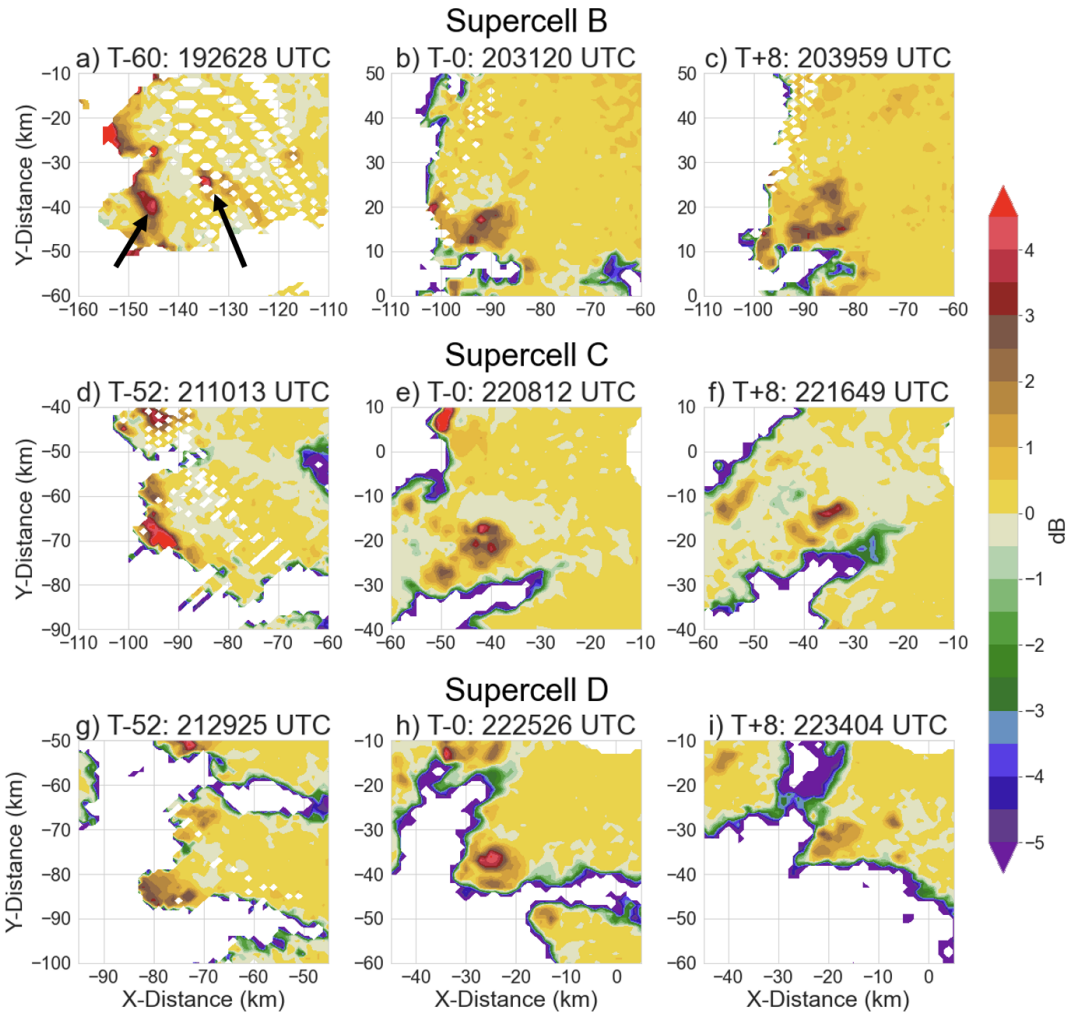


Figure 2.6: Horizontal cross-sections of gridded Z_{DR} at 5.5 km AGL as seen by KOUN for supercell B (a–c), supercell C (d–f), and supercell D (g–i).

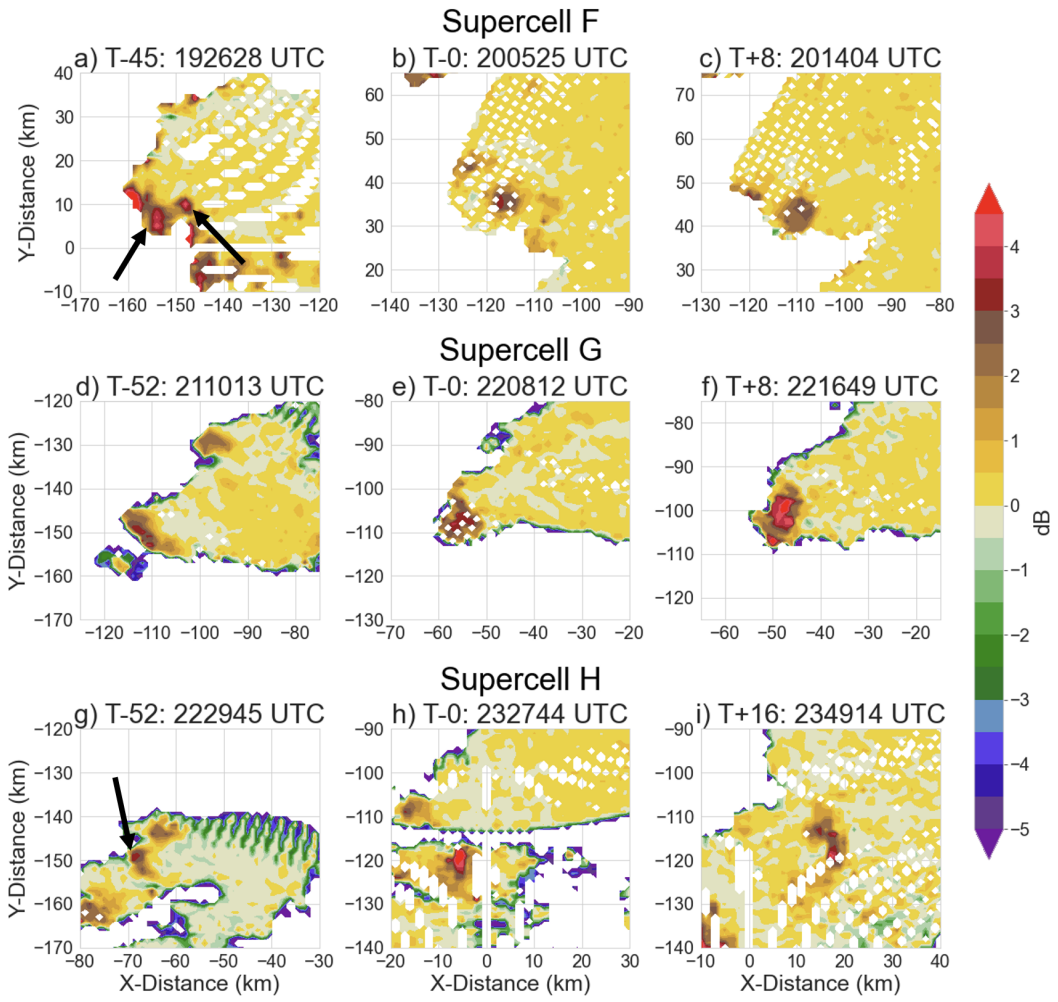


Figure 2.7: Same as in Fig. 2.6 but for supercell F (a–c), supercell G (d–f), and supercell H (g–i).

2.3.2 Z_{DR} Arc

When looking at the Z_{DR} arc, only the tornadic supercells had arcs that persisted longer than 40 min before tornadogenesis (Fig. 2.4c). The nontornadic supercells had arcs that appeared within the 40 min window before VROT_{max}. For the supercells where the early development of the Z_{DR} arc is captured by KOUN (supercells C and D), the arc appeared between 60-min prior to tornadogenesis (Fig. 2.4c).

Both supercells C and D had arc areas that gradually increased throughout the early development phase (Fig. 2.4c). Given that supercells C and D went on to produce tornadoes of similar intensity and longevity, and that the Z_{DR} arc intensity and size can be thought of as a proxy for changes in the storm-relative wind magnitude (Kumjian and Ryzhkov, 2009), it follows that the development of the Z_{DR} arc in both supercells is similar. Meanwhile, supercell G had a decreasing arc area leading to VROT$_{max}$ while supercells F and H remained quasi-constant (Fig. 2.4c).

At T-0, the nontornadic supercells had arc areas that were less than 100 km^2 while the tornadic supercells had arc areas that were larger than 100 km^2. This difference is also evident in Fig. 2.6c, which shows that the tornadic supercells have average arc areas (125 km^2) than the nontornadic supercells (64 km^2). The average areas of the Z_{DR} arcs were generally much larger than those found in Healey and Van Den Broeke (2023), highlighting how volatile the environment was on 24 May 2011.

The trends in arc area were also assessed with a higher Z_{DR} threshold ($>$ 4 dB). A Z_{DR} arc with larger values of positive Z_{DR} indicates larger drop sizes in the forward flank downdraft. Supercells B and D had the largest arc areas, while the remaining supercells had areas mostly between 0 – 20 km^2 (Fig. 2.4d). At tornadogenesis (or VROT$_{max}$), the tornadic supercells once again had larger arc areas (>10 km^2) compared to nontornadic supercells (0 – 13 km^2), with mean areas of 21 km^2 and 10 km^2, respectively (Fig. 2.4d and 2.6d).

The Z_{DR} arc's early evolution was visible at 2.0 km AGL in supercells B, C, and D, but not in supercells F, G, and H. The genesis of the arc presented itself in supercells C and D as a region of enhanced Z_{DR} in the southwest quadrant of the storm (Fig. 2.8f,k). This enhanced Z_{DR} region was characterized by a single, continuous 3-dB contour. The exception to this was supercell B, which had multiple Z_{DR} enhancement regions throughout the center and western half of the supercell (Fig. 2.8a). Other nontornadic

cells were observed outside supercells F, G, and H, most of which had Z_{DR} enhancement regions similar to supercells C and D at the genesis of the storms (Fig. 2.8f,k). It is possible that, at the early onset of supercells F, G, and H, the nontornadic supercells also had such Z_{DR} enhancement regions in the western half of the storm. However, it is hard to draw concrete conclusions given the limited low-level data during the early development of these nontornadic supercells.

As each supercell matured, the Z_{DR} enhancement region could be seen at for all supercells (Fig. 2.8 and 2.9). Before T-30, the tornadic arc of the tornadic supercells evolved into a curved arch of higher ($>$ 2 dB) Z_{DR} values that enveloped a distinct region of lower Z_{DR} (Fig. 2.8b,g,l). This lower Z_{DR} "hole" (also called a low Z_{DR} hail signature in Dawson II et al. (2014)) is often characterized by Z_{DR} between -1 and 0 dB. The Z_{DR} "hole" is accompanied by a local maximum in Z_H, indicating a region of hail.

Most of the nontornadic supercells also exhibited a Z_{DR} "hole" to varying degrees of prominence of the signature between T-25 and T-40 (Fig. 2.9a,e,g). The Z_{DR} "hole" was most pronounced in supercell H (Fig. 2.9g). During the T-30 window, supercells F and H had unorganized arcs (Fig. 2.9b-d and 2.9h-j). It is clear from Fig. 2.9 that supercells F and H were impacted by nearby storms, which likely influence the appearance of development of the Z_{DR} arc.

In the tornadic supercells, the Z_{DR} arcs exhibited smaller (or non-existent) Z_{DR} "holes" compared to supercell G between T-30 and T-0. Supercells F and H also had small (or non-existent) Z_{DR} "holes" between T-30 and T-0, but this the appearance of this feature could have been masked by nearby cells interacting with the main supercell (Fig. 2.9b-d and 2.9j-l). For supercells B, C, and D, the arc organized along the forward flank of the storm between T-30 and T-0 (Fig. 2.8c-e, 2.8h-j, and 2.8m-o). At T-0, the arc was characterized by a continuous region of 2 dB, with localized dB maxima

throughout. Generally, the region of $Z_{DR} > 3$ dB increased during this T-30 window in the tornadic supercells (Fig. 2.8c-e, 2.8h-j, and 2.8m-o).

For the nontornadic supercells, the Z_{DR} arc was either generally more disorganized (as in supercells F and H) or had a more prominent arc within the T-30 window (Fig. 2.9). Between T-5 and T-0, the areal extent of $Z_{DR} > 3$ dB also decreased in supercells F, G, and H (Fig. 2.9b-d, 2.9f-h, and 2.9j-l). However, at T-0, each arc still became attached to the forward flank, despite being more disorganized compared to the arcs in the tornadic supercells (Fig. 2.9d,h,l).

Most supercells on 24 May 2011 exhibited a localized Z_{DR} enhancement region in the southwest quadrant of the storm and a Z_{DR} "hole" preceding the attachment of the mature arc to the forward flank. Since each of the tornadic supercells exhibited a similar arc development, a conceptual model of the arc's early evolution is shown in Fig. 2.10. This model outlines the arc evolution outside of disruptions from cell mergers and summarizes the arc evolution up to T-0 for the tornadic supercells on 24 May 2011. Nontornadic supercells also generally followed this conceptual model, but it was challenging to verify the early genesis of the Z_{DR} enhancement region for the nontornadic supercells.

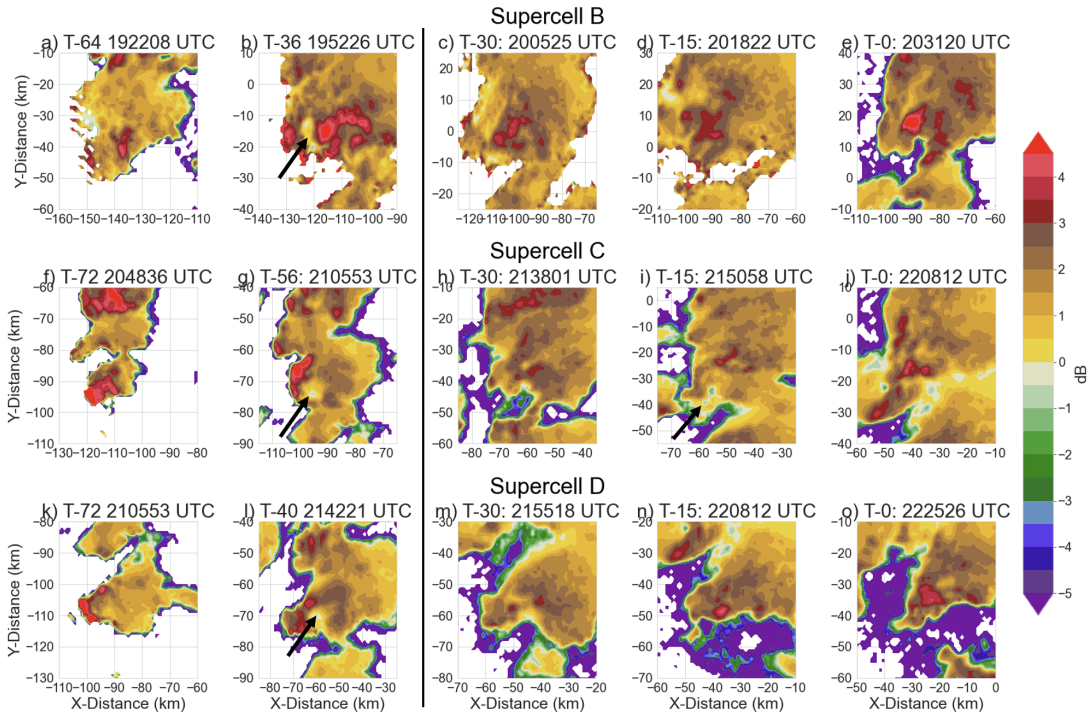


Figure 2.8: Horizontal cross-sections of gridded Z_{DR} at 1.5 km AGL as seen by KOUN for supercell B (a–e), supercell C (f–i), supercell D (k–o). Plots to the left of the black line are prior to the 30-min pre-tornadic window while plots to the right of the black line showcase the Z_{DR} arc during the 30-min window prior to tornadogenesis.

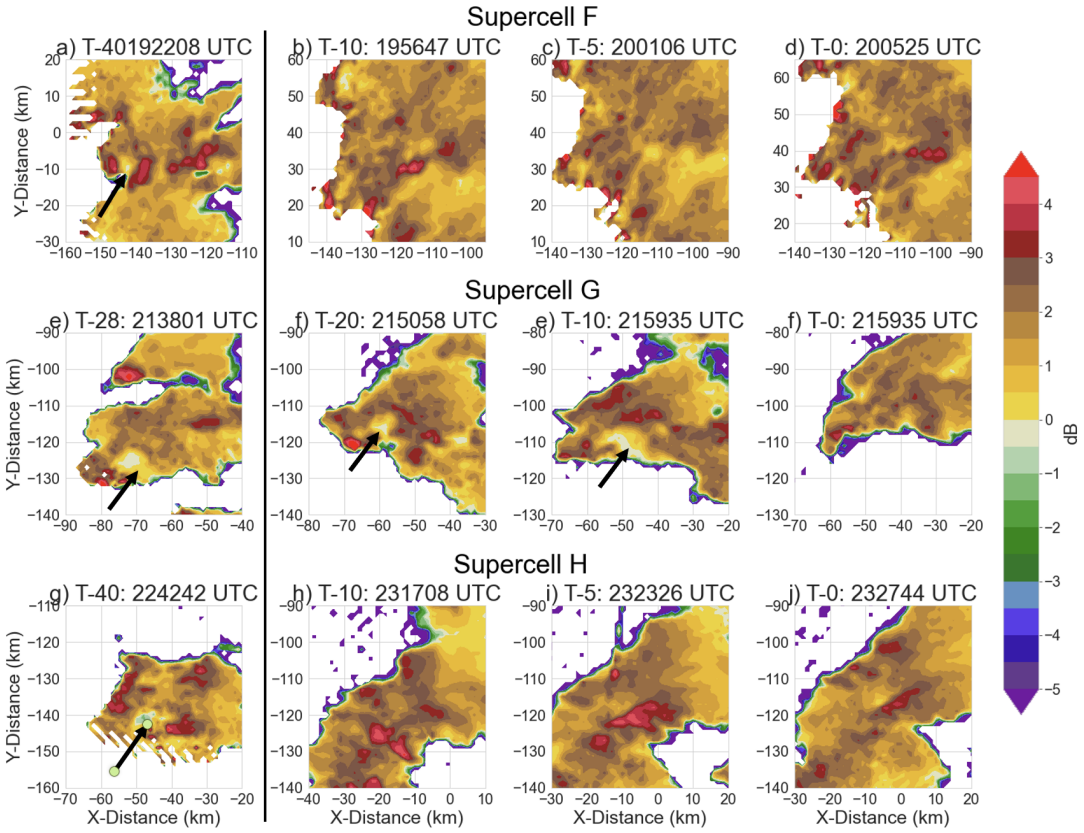


Figure 2.9: Same as in Fig. 2.8 but for supercell F (a–d), supercell G (e–f), supercell H (g–j).

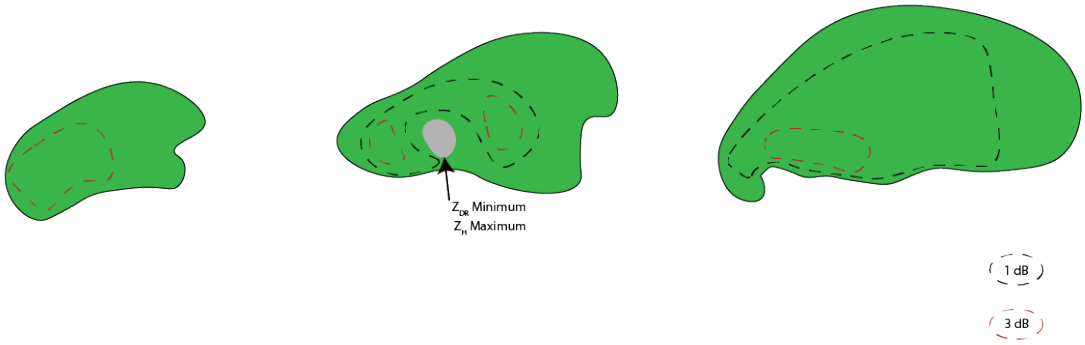


Figure 2.10: Conceptual model of the Z_{DR} arc development for the supercells on 24 May 2011. Black dashed lines represent the 2 dB contour while red dashed lines represent the 3 dB contour.

2.3.3 K_{DP} Foot

While supercell C and D had a similar range of values for the Z_{DR} arc area, they had different evolutions of the K_{DP} foot (Fig. 2.3e). Supercell C had a K_{DP} foot area that gradually increased from approximately 5 to 145 km^2 while supercell D had a K_{DP} foot that varied between 0 – 60 km^2 and did not have a consistent, temporal trend. Meanwhile, at T-0, supercell B had one of the largest K_{DP} foots of all the supercells with an area greater than 100 km^2.

The nontornadic supercells had a smaller average area of 52 km^2 compared to the average area of 79 km^2 for the tornadic supercells (Fig. 2.4e). When defining the K_{DP} foot using a higher threshold ($> 3^\circ$ km^{-1}), only the nontornadic supercells had a K_{DP} foot that exceed 3° km^{-1} within the T-30 window (Fig. 2.3f). The timing of the enhanced K_{DP} values in the nontornadic supercell F and H occurred within 13

min of VROT_{max} (Fig. 2.3f). Since the magnitude of K_{DP} scales with liquid water content, and thus negative buoyancy (Carlin and Ryzhkov, 2019), the enhanced values of K_{DP} seen in supercell F and H could be the result of excessive negative buoyancy that would adversely impact the intensification of the updraft and subsequent mesocyclone.

Despite not having a reported tornado, supercell G did not have a K_{DP} foot with values greater than 3° km^{-1} during the 30 min window prior to VROT_{max}. It is possible that supercell G produced a weak (EF0-EF1) tornado that went unreported due to the supercell passing through the scarcely populated Arbuckle Mountains in central Oklahoma. Supercell G also had a slightly stronger mesocyclone out of the three nontornadic supercells with a VROT_{max} of 33 m s^{-1} compared to 30 m s^{-1} for supercell H and 26 m s^{-1} for supercell F. However, whether or not supercell G produced a weak tornado is difficult to determine from KTLX velocity data. It is also possible that supercell G remained nontornadic due to other factors, while the presence of higher K_{DP} was what impacted tornado development in supercell F and H.

Finally, the structure of the K_{DP} foot across supercells had no distinct trend that separated one storm from another (not shown). The similarity in K_{DP} is reflected in the temporal evolution of the K_{DP} foot, with either the signature not existing during the early development phase or gradually increasing in size as seen with supercells B and C (Fig. 2.4e).

2.3.4 Z_{DR}-K_{DP} Separation Vector

In addition to the individual polarimetric radar signatures, the separation angle and distance between the Z_{DR} arc and K_{DP} foot centroids have been shown to distinguish between tornadic and nontornadic supercells (Loeffler et al., 2020; Homeyer et al., 2020). When evaluating the separation angles and distances of the tornadic and nontornadic supercells, there is a clear distinction between the median angles in the non-

tornadic (70°) and tornadic (127°) supercells (Fig. 2.11). The nontornadic storms also had smaller range in the separation angles (8° – 202°) compared to the tornadic storms (52° – 260°).

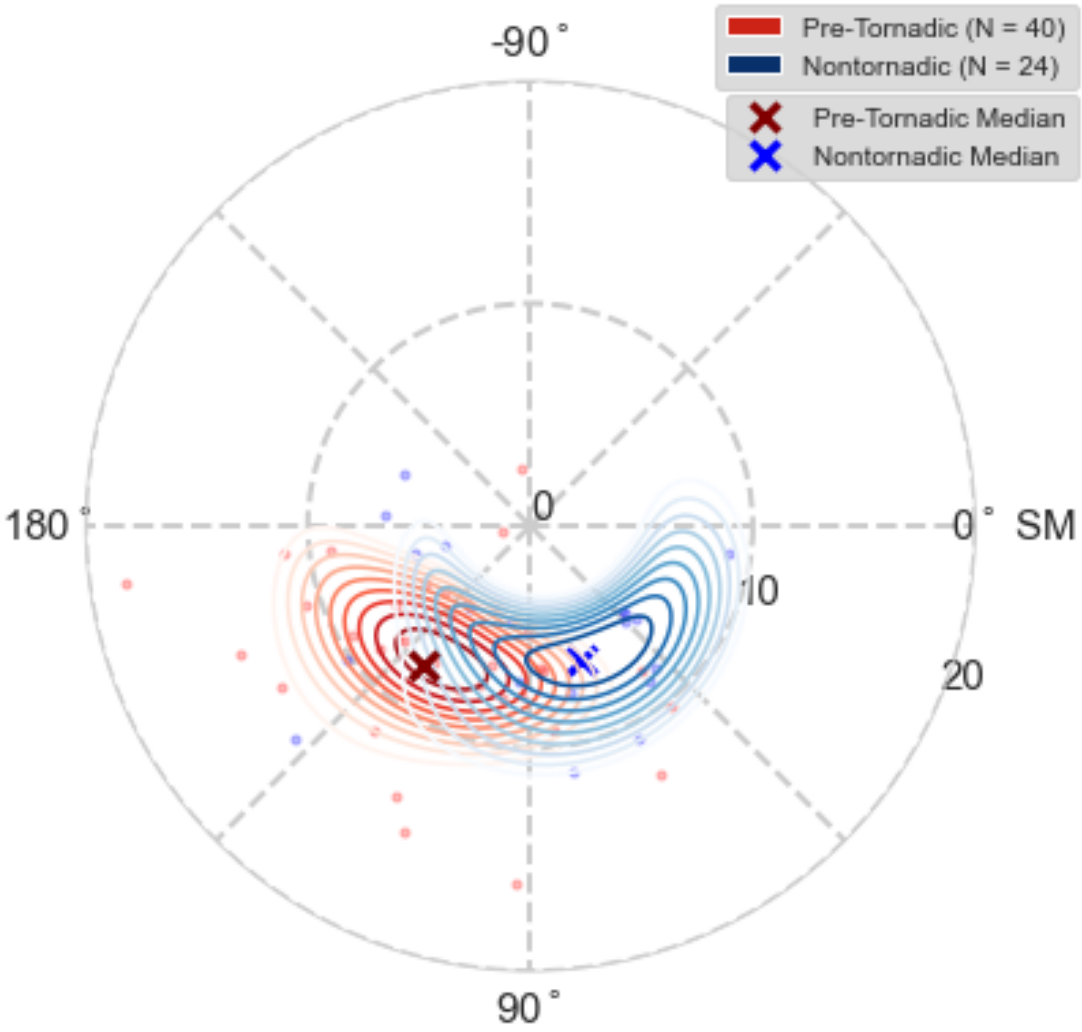


Figure 2.11: Kernel density estimate contours (≥ 50%) of the separation angle and distance for the tornadic (red) and nontornadic (blue) supercells during the T-30 to T-0 window. Storm motion is aligned with the 0°axis such that 90° is to the right of storm motion and -90° is to the left of storm motion. Red and blue markers represent the median separation angle and distance for the tornadic and nontornadic supercells.

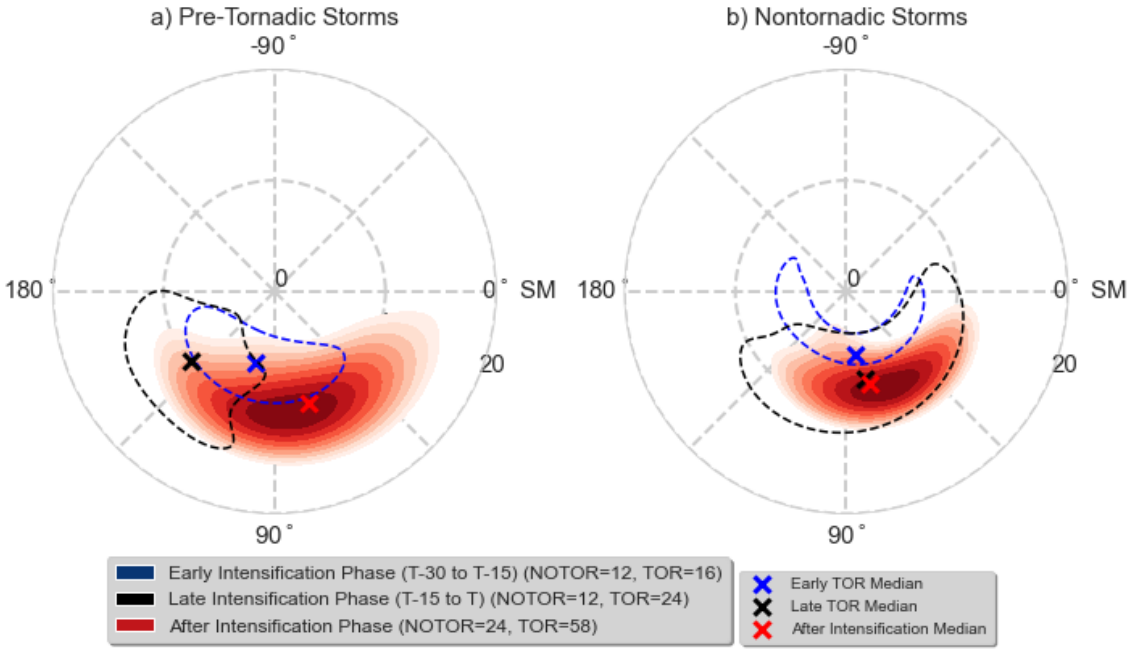


Figure 2.12: Kernel density estimate contours of the separation angle and distance for the tornadic (left) and nontornadic (right) supercells. The T-30 window is broken down into the early intensification phase (T-30 to T-15), the late intensification phase (T-15 to T), and after the intensification phase. Storm motion is aligned with the 0°axis such that 90° is to the right of storm motion and -90° is to the left of storm motion.

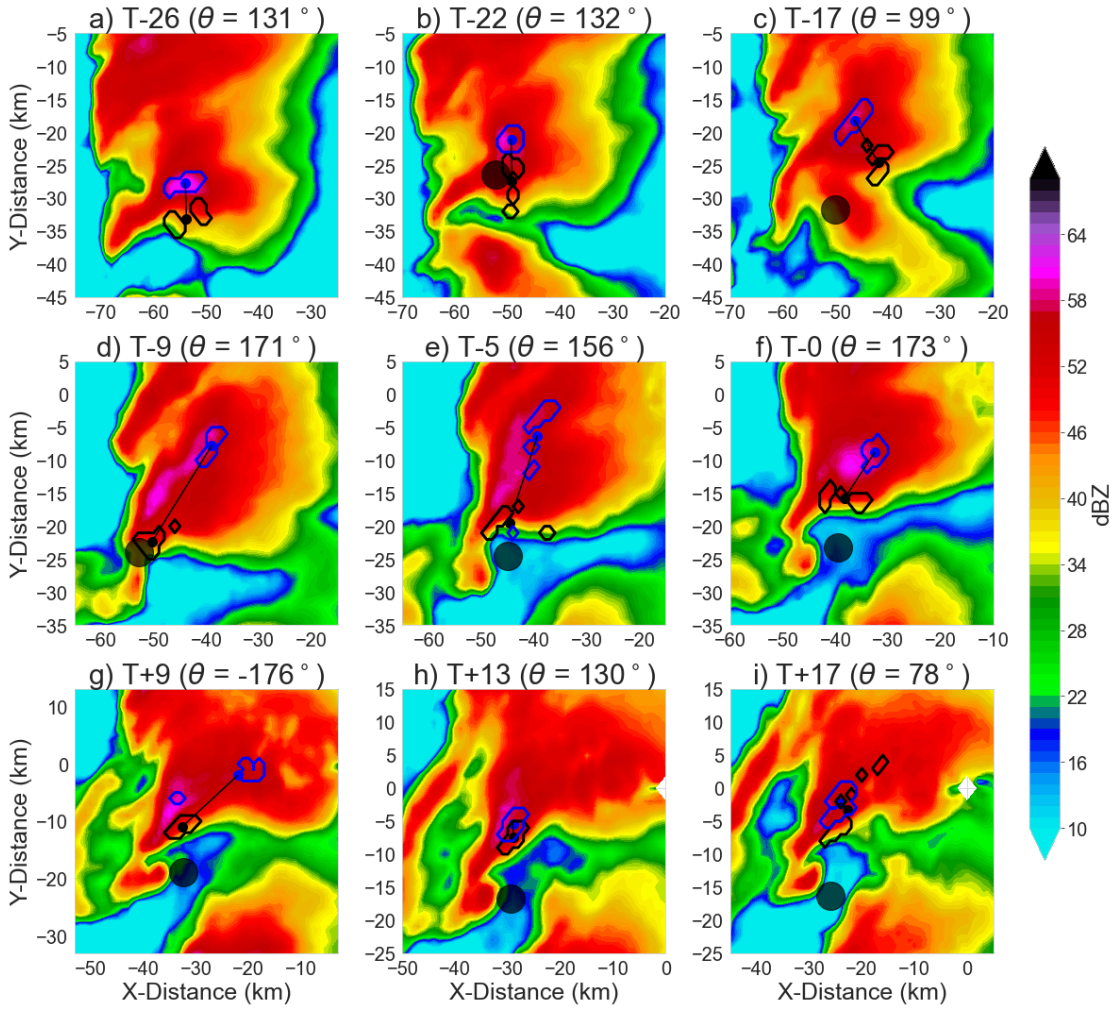


Figure 2.13: Evolution of the Z_{DR} -K_{DP} separation angle and distance for supercell C during and after the T-30 to T-0 window. The mesocyclone as seen by KTLX at 0.5°(black circle), K_{DP} foot (blue contour), K_{DP} foot centroid (blue point), Z_{DR} arc (black contour), Z_{DR} arc centroid (black point), and reflectivity (colorfill) at 1.5 km AGL are shown.

We further explored the evolution of the Z_{DR} -K_{DP} separation angle and distance during the 30-min window before tornadogenesis (or VROT$_{max}$) for the tornadic and nontornadic supercells (Fig. 2.12). During the early intensification phase (defined to be between T-30 and T-15), the separation angles for tornadic supercells indicated a perpendicular alignment between the Z_{DR} arc and K_{DP} foot relative to storm motion

(Fig. 2.12a). The median separation angle from T-30 to T-15 was 105°. During the late intensification period (T-15 to T), the separation angles shifted so the Z_{DR} arc was pushed to the west of the K_{DP} foot. This westward shift of the Z_{DR} arc occurred at slightly different times in different supercells, but the median angle in the late intensification phase (140°) is higher than in the early intensification phase (Fig. 2.12a). After the intensification period (during the tornado for the tornadic storms), the Z_{DR} arc and K_{DP} foot became more perpendicular relative to storm motion, with the Z_{DR} arc slightly shifted east of the K_{DP} foot (Fig. 2.12a). Meanwhile, the separation distance between the Z_{DR} arc and K_{DP} foot gradually increased from the early genesis to the post-genesis phase (Fig. 2.12a).

The same type of analysis was performed for the nontornadic supercells, but relative to VROT_{max} rather than the time of tornadogenesis (Fig. 2.12b). For nontornadic supercells, the separation angles between T-30 and T-15 had more variability compared to the tornadic supercells, with values ranging from 42°– 203°. The median angle during this period was 82°, which is 23°lower than the tornadic supercells. The storm-relative westward shift of the arc during the late intensification phase is not observed in nontornadic supercells. The arc and K_{DP} foot remain orthogonal to storm motion between T-15 and T, with a median separation angle of 78°. After the intensification phase, the median separation angle (76°) remains similar to what it was between T-15 and T. Thus, the greatest difference between the tornadic and nontornadic supercells during the intensification phase is seen in the median separation angles (140°for the tornadic supercells compared to 78°for the nontornadic) between T-15 and T.

An example of the evolution of the Z_{DR} arc and K_{DP} foot for the tornadic supercells is given in Fig. 2.13, which depicts the evolution of the Z_{DR} arc and K_{DP} foot for supercell C during each of the phases described in Fig. 2.12. In Fig. 2.13a – c, the Z_{DR} arc and K_{DP} foot at T-26 and T-22 are vertically aligned. As described in

Loeffler et al. (2020), a more orthogonal orientation between the Z_{DR}-K_{DP}separation and storm motion places the K_{DP} foot farther into the forward flank of the storm and away from the primary updraft. Removing the enhanced region of K_{DP}, and thus a region of negative buoyancy (Carlin and Ryzhkov, 2019), is likely beneficial for the enhancement of the low-level (0 – 2 km AGL) mesocyclone since excessively cold air inhibits buoyancy and tornadogenesis potential (Markowski et al., 2002; Markowski and Richardson, 2009).

During the late intensification period (T-15 to T), the supercell developed a well-defined hook echo (Fig. 2.13d – f). It was between T-15 to T that the low-level (0.5°as seen by KTLX) mesocyclone shifted into the hook echo of supercell C (Fig. 2.13d – f). Furthermore, during this period, the large drops within the Z_{DR} arc (black contours in Fig. 2.13) wrapped into the hook echo while the K_{DP} foot remained in the more northern portions of the supercell. This development in the arc and K_{DP} foot caused the separation angle to increase from T-9 to T (Fig. 2.13d – f).

At the time of tornadogenesis, the enhanced K_{DP} within the supercell began to shift southwestward in a storm-relative sense (Fig. 2.13f). This displacement continued until the K_{DP} foot was nearly on top of the Z_{DR} arc at T+17 (Fig. 2.13f – i). The southwestward movement (in a storm-relative sense) of the K_{DP} foot was what caused the separation angles to decrease from T to T+17. Furthermore, the hook echo began to deteriorate at 2242 UTC (T+34), only 17 min after the K_{DP} foot shifted towards the mesocyclone. Once the hook echo deteriorated, the tornado soon followed and dissipated at 2201 UTC (approximately T+48). In this case, it is unlikely that the initial displacement of the K_{DP} foot towards the mesocyclone weakened the supercell by introducing a higher liquid water content into the updraft. This is because the hook echo of supercell C was elongated to the southwest (Fig. 2.13h and 2.13i). Thus, as the K_{DP} foot moved to the southwest in a storm-relative sense from T+9 to T+13,

the hook and subsequent mesocyclone stretched to the southwest as well, effectively maintaining a separation between the mesocyclone and K_{DP} foot.

2.3.5 Storm Interactions

In addition to the temporal evolution of polarimetric radar signatures within each supercell, there were also interactions of the Z_{DR} arc across multiple supercells (Fig. 2.14). The first type of arc interaction is showcased in Fig. 2.14a – c, from the genesis of the EF5 tornado (recorded as 2050 UTC by the NWS and approximated to be 2048 UTC as seen by KOUN) to 2105 UTC. A supercell to the south began to merge into the forward flank of supercell B at 2048 UTC (Fig. 2.14a). This merger event is well documented by Tanamachi et al. (2015), and the two storms are considered to be one reflectivity object at 2055 UTC based on the work done in Tanamachi et al. (2015). Tanamachi et al. (2015) looked at the mid-level (5 km AGL) updrafts of both supercell B and the merging cell and noted that the updrafts of both storms merged at 2105 UTC. However, the two mesocyclones at 0.5° as seen by KTLX do not merge until 2118 UTC.

During this merger, the Z_{DR} arc from the southern supercell pushed the mesocyclone in supercell B northward from 2048 – 2105 UTC (Fig. 2.14a – c). During this period, the original arc follows the original mesocyclone and moves northward while a new arc forms between the new and original arcs (we will refer to this as the bridge arc). At 2056 UTC Tanamachi et al. (2015) noted a new updraft pulse that bridged the updrafts of supercell B and the merging storm. When looking at the Z_{DR} column between 2048 UTC, there are three distinct regions of enhanced Z_{DR}trailing from south to north, likely indicating the early location of the three updraft pulses seen in Tanamachi et al. (2015) (Fig. 2.14a). At 2048 UTC, these regions of enhanced Z_{DR} align with the location of the original, bridging, and new arc (Fig. 2.14a). This remains

true at 2057 UTC, though the three Z_{DR} columns are beginning to consolidate at this time (Fig. 2.14b). The bridging arc may have formed as a result of the updraft pulse seen in Tanamachi et al. (2015), meaning the development of the arc at 1.5 km AGL is indicative of the updraft development aloft in supercell B. Finally, he new arc associated with the mesocyclone of the merging storm attaches to the forward flank of the reorganizing supercell at 2105 (Fig. 2.14a – c).

Supercell C experienced a storm merger before the genesis of its EF4 tornado at 2206 UTC (as determined by the NWS). The merger is shown in Fig. 2.14d – f. Similar to supercell B, the new storm merged from the south of the primary supercell (Fig. 2.14d). The merger mesocyclone dissipated near 2155 UTC, and the mesocyclone of supercell C persisted (Fig. 2.14e). It is when the mesocyclones merger that the Z_{DR} arc developed into a more uniform region of $Z_{DR} > 3$ dB. Aloft, the Z_{DR} column forms a partial Z_{DR} ring at 2155 UTC (Fig. 2.14e). Within this ring, there are two distinct regions of $Z_{DR} > 3$ dB (not shown), which could indicate the presence of smaller updraft pulses within the broader updraft. These two regions of $Z_{DR} > 3$ dB consolidate at 2203 UTC (not shown) when the arc attaches to the forward flank (Fig. 2.14f). The process of the reorganization of the Z_{DR} arc during mesocyclone and updraft merger events in supercells B and C lead to the hypothesis that structure of the Z_{DR} arc could be an indicator of multiple updrafts or mesocyclones prior to tornadogenesis.

Finally, supercell G also experienced a cell merger; however, the merging cell was east of supercell G's mesocyclone (Fig. 2.14g – i). Since the merging storm was displaced eastward, Z_{DR} columns and mesocyclones never interacted. At 2203 UTC, when the merging cell partially combined with the eastern portion of supercell G, the Z_{DR} arc of the supercell is disorganized (Fig. 2.14h). However, as the merging storm passed through the eastern portion of the forward flank of supercell G, the Z_{DR} arc of supercell G reformed (Fig. 2.14i). Since the mesocyclones never interacted, the merg-

ing storm passed through the forward flank of the primary supercell and continue to move northward.

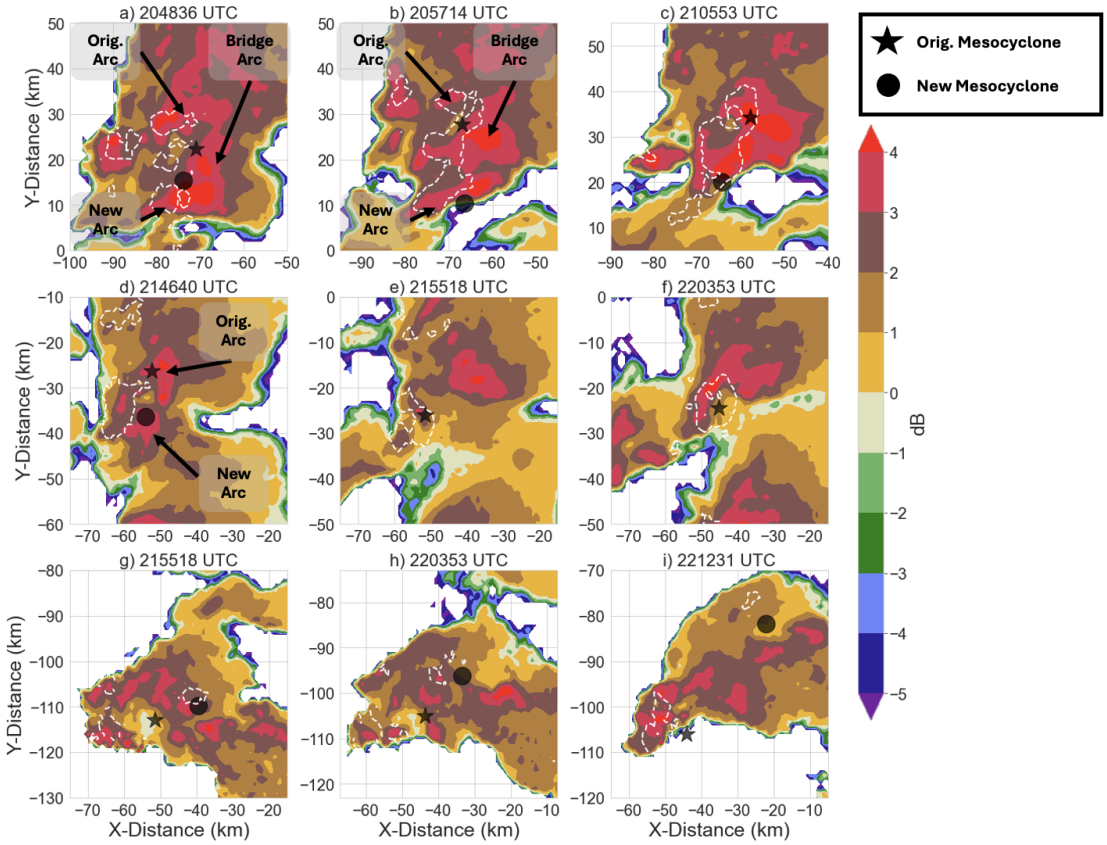


Figure 2.14: Evolution of supercell interactions for supercell B (a – c), supercell C (d – e), and supercell G (f – h) at 1.5 km AGL. The mesocyclones at 0.5°as seen by KTLX are shown (black circle and star). White dashed lines represent the 1 dB contour at 5.5 km AGL. The x- and y-axes are adjusted to remain centered on each supercell.

2.4 Summary and Discussion

Both nontornadic and tornadic supercells exist in the same environment (e.g., Klees et al., 2016), creating a challenge for forecasting tornado formation. While past work has found multiple environmental and dynamical differences between tornadic and nontornadic supercells (e.g., Markowski et al., 2002; Hirth et al., 2008; Markowski and

Richardson, 2014; Coffer et al., 2017b), such features cannot be easily resolved by the current operational network. Dual-polarization radar signatures have shown some promise in distinguishing between supercells that produce tornadoes and those that do not (e.g., Van Den Broeke, 2017; Loeffler et al., 2020; Homeyer et al., 2020; French and Kingfield, 2021); however, only one study (Healey and Van Den Broeke, 2023) has focused on evaluating dual-polarization signatures in the same environment.

Through a case study approach, this study assessed polarimetric signatures over time in tornadic and nontornadic supercells during the 24 May 2011 tornado outbreak. To perform the required analysis, KOUN data were gridded, and each polarimetric signature was detected using a simple algorithm throughout the lifecycle of each supercell. The temporal evolution and structure of polarimetric signatures in six supercells (three tornadic, three nontornadic) were then analyzed.

The primary results from this work are summarized herein:

- Similar development of the Z_{DR} arc in most supercells
- Tornadic supercells exhibited Z_{DR} rings within 8 min of tornadogenesis
- Each of the long-lived, EF4+ tornadoes were characterized by a decrease in Z_{DR} column area and magnitude 4 to 8 min after T-0
- Tornadic supercells consistently had larger mean areas for all polarimetric signatures
- $K_{DP} > 3$ deg/km only existed in nontornadic supercells between T-30 and T-0
- Tornadic supercells had larger separation angles than the nontornadic supercells, and this distinction was maximized within 15 min of tornadogenesis (VROT_{max})
- The structure of the Z_{DR} arc could be indicative of updraft pulses or mesocyclone merger events prior to tornadogenesis

The development of the Z_{DR} arc started in the western portion of most supercells and grew into an arc with a Z_{DR}-"hole" (or hail fallout region) before attaching to the forward flank of the mature supercell. This development represents the evolution of the Z_{DR} arc without interactions from other storms. For the temporal trends in the Z_{DR} arc and K_{DP} foot, these low-level signatures appeared 30 min earlier in the tornadic supercells compared to the nontornadic supercells. However, it should be noted that the available data from KOUN limit the comparison of the timing of the Z_{DR} arc and K_{DP} foot.

Only the nontornadic supercells had $K_{DP} > 3$ dB during the 30 min before VROT_{max}, potentially indicating the presence of a higher liquid water content and subsequent negative buoyancy (Carlin and Ryzhkov, 2019). Furthermore, nontornadic supercells generally had smaller K_{DP} foot areas (52 km^2 on average) with higher average maximum magnitudes (3.1 deg/km) compared to tornadic supercells (79 km^2 and 2.8 deg/km on average). This means nontornadic supercells had a smaller, yet more intense K_{DP} foot while tornadic supercells had a larger, yet weaker K_{DP} foot. For the Z_{DR} arc, tornadic supercells had larger arc areas than the nontornadic storms. Since size sorting can be maintained by the updraft or storm-relative mean winds (Kumjian and Ryzhkov, 2009; Dawson et al., 2015a), it is possible that tornadic storms had stronger low-level updrafts or larger storm-relative mean winds compared to nontornadic storms.

The Z_{DR} -K_{DP} separation angle was larger in tornadic supercells compared to nontornadic ones. Median separation angles in the tornadic and nontornadic supercells were slightly larger than the average angles in Loeffler et al. (2020), where tornadic supercells had separation angles near 90°and nontornadic ones near 0°. The difference may be due to the volatile environment on 24–25 May 2011, which allowed Z_{DR} arcs to be closer to the updraft. Given the highly favorable conditions for strong tornadoes, even the nontornadic supercells on 24 May 2011 may have had stronger mesocyclones

compared to mesocyclones from storms in less volatile environments. A stronger mesocyclone could pull larger drops closer to the updraft and shift the arc's core westward (in a storm-relative sense). Despite this, the 45–90°angle difference between tornadic and nontornadic supercells remained similar to Loeffler et al. (2020).

The Z_{DR} column areas in the tornadic supercells were, on average, larger than what was seen in the nontornadic supercells. Previous studies have linked wider updrafts to greater tornado intensity (Van Den Broeke, 2017; Marion et al., 2019; Sessa and Trapp, 2020). However, it is difficult to conclude that the updrafts in the tornadic supercells on 24 May 2011 were wider than the nontornadic supercells with only a 8 km^2 difference in the mean column area. A broader, climatological sample would likely reveal greater variability in column area and subsequent updraft size due to environmental differences and a larger sample size.

This study is limited by the spatiotemporal resolution of the KOUN and KTLX radar data. After gridding the radar data, scans at each height were separated by 4-6 min. However, it is known that processes related to tornadogenesis can occur on short time scales that cannot be resolved by the current operational radar network (Wurman and Randall, 2001; Heinselman et al., 2012; Pazmany et al., 2013; Kurdzo et al., 2017). It would be interesting to observe trends in polarimetric radar signatures at higher temporal resolutions to examine shorter time-scale variability among supercells or to see if entirely new trends appear. With these limitations in mind, it is important to prioritize detailed observations of supercells within the same environment to increase the sample size and temporal resolution of this type of analysis. Other future work includes modeling of polarimetric radar signatures to get the 3D development of these features on short time scales.

Chapter 3

A Comparative Analysis of Polarimetric Radar Signatures in Pre-Tornadic Supercells Across CM1 Microphysics Schemes and Observations

3.1 Introduction

From 2011 – 2013, dual-polarization was implemented into the Weather Surveillance Radar 1988 Doppler (WSR-88D) network, allowing for the identification of hydrometeor type, orientation, and size from radar data. With dual-polarization radar data, several features have since been identified as relevant to supercell intensification and development. Such features include, but are not limited to, the differential reflectivity (Z_{DR}) column (Snyder et al., 2015; Van Den Broeke, 2016; French and Kingfield, 2021), Z_{DR} arc (Kumjian and Ryzhkov, 2008, 2009; Dawson II et al., 2014, 2015), spectral differential phase column (K_{DP}; Hubbert et al., 1998; Loney et al., 2002), K_{DP} foot (Romine et al., 2008), correlation coefficient (ρ_{hv}) and Z_{DR} rings (Kumjian

and Ryzhkov, 2008), and tornadic debris signatures (Ryzhkov et al., 2005; Van Den Broeke and Jauernic, 2014; Bodine et al., 2014; Cross et al., 2023). However, despite the improvements to the WSR-88D network, the spatial and temporal resolution of the WSR-88Ds during operational scanning strategies is often too coarse to resolve processes such as tornadogenesis and hail fallout. Higher resolution dual-polarization and velocity data have been obtained using mobile radars (e.g., Snyder et al., 2013; Houser et al., 2015; Bluestein et al., 2019; Wakimoto et al., 2020), but such observations are challenging to obtain.

Numerical models provide an additional method for evaluating supercells at higher spatiotemporal scales and provide information about storm microphysics. Simulations allow for the unique comparison of supercell dynamics and microphysics to dual-polarization radar signatures. However, multiple factors introduce uncertainty in such a comparison, including, but not limited to, the selected microphysics scheme, the implemented melting model, and the limitations of the forward operator used to obtain the polarimetric radar variables.

How model microphysics are represented depends on various inputs, including, but not limited to, how particle electromagnetic scattering is represented in the model, the selected microphysics scheme, and the representation of mixed-phase particles. Various microphysics schemes can represent the hydrometeor distribution within a supercell. Spectral bin schemes (Khain et al., 2015) allow for better representation of the hydrometeor distribution by discretizing the particle spectral density (PSD) into bins. These bins are sorted by particle mass or diameter and are not predicted by a specific functional form of the PSD. However, the flexibility of the spectral bin schemes comes at the cost of computational efficiency, making it challenging to apply the spectral bin scheme to ensembles of high-resolution numerical simulations.

A bulk microphysics parameterization (BMP) scheme is more computationally ef-

ficient than the spectral bin scheme, but assumes one functional form of the PSD for the predicted output. BMPs predict bulk parameters for each hydrometeor species, where the number of predicted variables corresponds to the moment of the BMP (e.g., 1-moment BMPs predict one variable, 2-moment BMPs predict two variables, and so on). Other methods of parameterizing model ice species have been presented, such as the predicted particle properties (P3) scheme, where properties of the ice particles are predicted rather than split into different categories (Morrison and Milbrandt, 2015). Another example is the Lagrangian cloud model (LCM; Shima et al. 2009), which calculates parameters of "super droplets" that then represent other particles with the same properties.

Previous studies have assessed the performance of different microphysics schemes through case studies in which model output is compared to observations (e.g., Morrison and Pinto 2006; Gallus Jr. and Pfeifer 2008; Rajeevan et al. 2010). However, to compare observations to dual-polarization radar signatures emulated from model output, the model output must be converted to polarimetric data through either a radar simulator or a polarimetric forward operator. The T-matrix scattering method numerically solves Maxwell's equations to calculate electromagnetic scattering by nonspherical particles. The T-matrix method was initially developed by Waterman (1965) and has since been implemented in emulations of polarimetric weather radar. In 2010, Jung et al. developed a forward operator that integrates the T-matrix scattering calculations over the PSD for all hydrometeor types. This emulator assumes a fixed axis ratio of 0.75 for snow and hailstones.

Since BMPs do not predict the particle size distributions of mixed-phase hydrometeors, melting models are needed in addition to a forward operator to properly simulate dual-polarization radar signatures. Melting models use the predicted hydrometeor classes (often including rain, dry ice, and cloud water) to calculate the drop size

distribution (DSD) parameters for mixed-phase particles. These calculations are approximate and thus inherently introduce uncertainty in the accuracy of the PSD for mixed-phase particles. The Jung et al. (2010) forward operator implements the melting model described in Jung et al. (2008) (hereafter J08). Dawson II et al. (2014) and Johnson et al. (2016) also implemented the Jung et al. (2010) forward operator with an updated melting model that allows the fraction of liquid water for all hydrometeor species to vary across the size distribution.

Other forward operators include the Hebrew University Cloud Model (HUCM) developed by Ryzhkov et al. (2011), which employs a spectral bin microphysics scheme to compute polarimetric radar observables. Additionally, the Cloud Resolving Model Radar Simulator (CR-SIM; Oue et al. 2020) is another polarimetric forward operator that implements the T-matrix scattering approximation across multiple radar and lidar frequencies. However, CR-SIM only calculates radar variables for dry hydrometeors and thus cannot replicate the "bright band" at the melting layer or other mixed-phase regions. The POLArimetric Radar Retrieval and Instrument Simulator (POLARRIS) is a forward operator that relates output from cloud resolving models to polarimetric radar variables and other radar-consistent geophysical parameters, such as vertical velocity and rainfall rate (Matsui et al., 2019). One distinguishing feature of POLARRIS from other forward operators is that POLARRIS assigns particle axis ratios and orientation angles, which is information not inherently provided by the model microphysics schemes (Matsui et al., 2019).

While the T-matrix method provides scattering information of hydrometeors, it is computationally expensive to implement at high spatiotemporal resolutions and for data assimilation. With this in mind, Zhang et al. (2021) parameterized the T-matrix method by developing a set of fitted equations that approximate the polarimetric radar variables obtained from the T-matrix calculations. The resulting parameterized for-

ward operator (PFO) is more computationally efficient than the original T-matrix method (10.55 s versus 0.098 s at 1-km horizontal grid spacing) and still produces realistic polarimetric radar signatures (Zhang et al., 2021). The PFO implements the J08 melting model, although an update to the previously established model was presented in Liu et al. (2024b).

The PFO has been compared against WSR-88D data for severe convection (Zhang et al., 2021; Liu et al., 2024b; Healey and Broeke, 2025), implemented for data assimilation (Du et al., 2021; Liu et al., 2024a; Eure et al., 2025), and could serve as a potential improvement to the Warn-on-Forecast System at the NOAA National Severe Storms Laboratory (Heinselman et al., 2024). However, the PFO and Liu et al. (2024b) melting models have not been tested at high spatial resolutions (< 100 m). As such, it is unknown whether the PFO and associated melting models can accurately resolve small-scale features in simulated polarimetric radar signatures. Implementing the PFO at higher spatial resolutions can extend its applicability to the study of supercells, which are known to involve processes that occur at small scales (e.g., tornadogenesis). Furthermore, while multiple microphysics schemes have been implemented with the PFO (e.g., Liu et al. 2024b), it is unknown what the ideal combination of melting model and microphysics scheme is for high-resolution simulations of severe convection. Thus, this study aims to answer the following:

- How can melting models be improved to better represent mixed-phase precipitation in supercells?
- What melting model best represents polarimetric radar signatures common to supercells at high spatial resolutions?
- Which microphysics scheme produces polarimetric radar signatures comparable to supercell observations?

To answer these questions, idealized simulations of supercells at high spatial resolution (75 m) will be compared to observations of the 24 May 2011 supercell that produced the prolific El Reno tornado. The PFO from Zhang et al. (2021) will be used to derive polarimetric variables and to test the J08 and L24 melting models, as well as a new melting model, to determine which best represents melting precipitation in tornadic supercells. Three microphysics schemes will also be tested with the Zhang et al. (2021) PFO – the Morrison 2-moment, NSSL 2-moment, and NSSL 3-moment schemes – to assess the impact microphysics schemes have on dual-polarization radar signatures. The combined analysis of various melting models, microphysics schemes, and high-resolution polarimetric radar data from the PFO makes this study unique, as the impact of each component can be evaluated in a single study.

Section 3.2 details the selected event chosen for this study, the PFO and melting models tested, and the chosen microphysics schemes. Section 3.3 provides a comparison of the melting models, while section 3.4 compares the different microphysics schemes to observations. Finally, section 3.5 summarizes the goals and findings from this study.

3.2 Data and Methodology

For the evaluation of different melting models and microphysics schemes, the 24 May 2011 tornado outbreak in central Oklahoma was selected. This case was selected because the sounding used yields a simulation that produces simulated tornadic supercells with violent tornadoes (see Orf et al. 2017). In Orf et al. (2017), it is described that the sounding was taken from a Rapid Update Cycle (Benjamin et al., 2004) model forecast from the inflow of the El Reno supercell. Additionally, continuous polarimetric radar observations of the El Reno supercell were collected by the KOUN research WSR-88D radar in Norman, OK. The dataset from KOUN allows for the analysis of the broad

supercell structure and comparison to simulations. For a more detailed description of the kinematics and evolution of the El Reno supercell during tornadogenesis, the reader is referred to Tanamachi et al. (2015), Houser et al. (2015), and French et al. (2015), as well as Chapter 2.

3.2.1 Description of Observations

Radar observations from KOUN and KTLX were used to compare with the simulated radar data. Before the data could be compared, the observed radar data were first quality-controlled.

For the KOUN radar, K_{DP} was calculated using the default configuration of the Python ARM Radar Toolkit (Py-ART) (Helmus and Collis, 2016) Vulpani algorithm (Vulpiani et al., 2012). Additionally, the Z_{DR} field was corrected by 0.1 dB by comparing the Z_{DR} field above the freezing level (approximately 4.5 km AGL from Orf et al. (2017) environmental sounding) to the expected value of Z_{DR} for dry snow (0.2 dB). Only the Z_{DR} field in regions of relatively low Z_H (< 30 dBZ) were considered to help remove bins contaminated by hail. To better compare KOUN data with the simulated radar data, the KOUN dataset was gridded using Py-ART's Barnes interpolation with a constant radius of influence of 1 km. KOUN data were gridded to a 1 km x 1 km x 0.5 km grid.

For the comparison of supercell size across the simulated and observed supercells, the observed supercell that produced the EF5 El Reno tornado was manually outlined using the Python lasso selector tool. Finally, each strongly tornadic supercell on 24 May 2011 in central Oklahoma was manually outlined using the Python lasso selector tool. The 20-dBZ contour was used as a guideline for the lasso. The outline of the lasso was manually interpolated across regions without a closed 20-dBZ contour in cases of interactions with nearby convection. The number of bins within the lasso was

saved and then multiplied by the bin size to obtain the area of the supercell. This analysis was performed at the time of tornadogenesis for the observed supercell, which was defined by NWS storm reports (NOAA, 2011). The lasso method was not used for the simulated supercells, as there was no influence of nearby convection to impact the supercell size calculations. A 20-dBZ threshold was applied to the simulated data, and the number of bins that met the threshold criteria was saved. Like with the observed data, the number of bins was multiplied by the area of each bin, producing the area of the supercell. Again, this analysis was performed at the time of tornadogenesis for the simulated dataset, which was defined to be the first time the Okubo–Weiss parameter (Eq. 3.1 Okubo, 1970; Weiss, 1991) was greater than 0.1 s^{-1}.

$$OW = \zeta^2 - (S_n^2 + S_s^2) \tag{3.1}$$

3.2.2 Melting Models

In the following subsection, three melting models are described in detail: the J08 model, the Liu et al. (2024b) (hereafter L24) model, and a new model proposed to better represent supercell convection. In each melting model, a fixed density is assumed for all dry hydrometeors and rain, while the density of the mixed phase particles is given by $\rho_m = \rho_x(1 - f_w^2) + \rho_w f_w^2$, where ρ_x is the density of the ice species, ρ_w is the density of liquid water, and f_w is the liquid water fraction $f_w = q_r/(q_r + q_i)$. Given the density equation for mixed-phase particles, the density of each ice species ranges from ρ_x for $f_w = 0$ to ρ_w for $f_w = 1$. Table 3.1 gives the values of ρ for each hydrometeor type used in this study.

Table 3.1: List of densities for each hydrometeor category.

Hydrometeor Type	Density (kg/m^3)
Rainwater	1000
Hail	913
Melting Hail	913 – 1000
Graupel	400
Melting Graupel	400 – 1000
Snow	100
Melting Snow	100 - 1000

3.2.2.1 J08 Melting Ice Model

The three ice hydrometeors considered are hail, graupel, and snow. In Jung et al. (2008), the rain-ice mixture is only allowed to exist where the model predicted q_r and q_i coexist. The fraction of the rain-ice mixture is assumed to be

$$F = F_{max}[min(q_x/q_r, q_r/q_x)]^{0.3} \tag{3.2}$$

where F_{max} represents the maximum fraction of ice or rainwater mixing ratio that can exist in the rain-ice mixture and $x \in [s, g, h]$. In Jung et al. (2008), $F_{max} = 0.5$. With F defined, the mixing ratio of rainwater within the mixture can be obtained using:

$$q_{r,a} = Fq_r \tag{3.3}$$

and the mixing ratio of dry ice within the mixture can be obtained using:

$$q_{x,a} = Fq_x. \tag{3.4}$$

The water fraction of the mixture can be calculated using $f_w = q_r/(q_r + q_i)$, and the total mixing ratio of the mixture is

$$q_{mx} = q_{x,a} + q_{r,a} = F(q_r + q_x). \tag{3.5}$$

To retain mass conservation, the rainwater within the rain-ice mixture is subtracted from the predicted total q of rainwater. Thus, the q of pure rainwater becomes $q_{pr} = q_r - q_{r,a}$. For multiple ice species, this equation is expanded to include the rainwater used by each ice species. For instance, for simulations with both hail and graupel, the equation becomes: $q_{pr} = q_r - q_{r,a_{hail}} - q_{r,a_{graupel}}$. Likewise, the dry ice within the rain-ice mixture must be subtracted from the predicted total q of the ice species (e.g., $q_{px} = q_x - q_{x,a}$). It should be noted that the number concentration (N_t) and reflectivity factor (Z) are not conserved, such that $N_{t,pr} = N_{t,r}$ and $Z_{pr} = Z_r$.

3.2.2.2 L24 Geometric Mean

An update to the Jung et al. (2008) melting model was introduced in Liu et al. (2024b). In this updated melting method, the mixing ratio, number concentration, and reflectivity moment are obtained for a melting ice species using a geometric mean of the rain and dry ice species. The total q, N_t, and Z are given as:

$$q_{mx} = \sqrt{q_r q_x}\ , \tag{3.6}$$

$$N_{t,mx} = \sqrt{N_{t,r} N_{t,x}}\ , \tag{3.7}$$

$$Z_{mx} = \sqrt{Z_r Z_x}\ . \tag{3.8}$$

As in J08, the q of the liquid water ($q_{r,a}$) and dry ice ($q_{x,a}$) within the rain-ice mixture are subtracted from the original model-predicted mass of rainwater. This ensures the

mass of rainwater is not double-counted for the ice and rain hydrometeor species. The q of the dry ice in the rain-ice mixture is also subtracted from the q of the model-predicted ice species. Finally, the densities are treated the same as they are in J08.

3.2.2.3 Combined Melting Model (CMM)

A new melting model is proposed herein, which will be tested on high-resolution supercell simulations. This new melting model, which we define as the Combined Melting Model (CMM), takes the method for calculating q_{mx} from J08 (Eq. 3.5) and the geometric mean (Eq. 3.7 and 3.8) from L24 for N_{mx} and Z_{mx}. The CMM essentially removes the assumption that the dry and mixed-phased hydrometeors have equivalent number concentrations. Finally, the calculation of f_w, ρ_x, q_{pr}, and q_{px} are the same as in J08.

3.2.3 Polarimetric Forward Operator

The PFO used in this study is described in detail in Zhang et al. (2021) and is applicable for S-band wavelengths (2-4 GHz). When using the PFO, it is assumed that all hydrometeors are spherical. Also, the PFO sets an upper limit to the maximum mass weighted mean diameter hydrometeor (D_m) sizes for the ice categories – 35 mm for hail and 18 mm for snow and graupel – as beyond these sizes the results are not reliable. The PFO uses a set of parameterized equations to represent the relationship between radar variables and D_m, water fraction (W = $\rho_a q_r$), and the reflectivity factor (Z_x). The derivation of these fitted polynomials is described in Mahale et al. (2019), but the relationships for rain are provided in Eq. 3.9 – 3.12 and the relationships for ice hydrometeors are given in Eq. 3.13 – 3.16.

$$Z_h \approx W(-0.3078 + 20.87D_m + 46.04D_m^2 - 6.403D_m^3 + 0.2248D_m^4)^2 \tag{3.9}$$

$$Z_{dr} \approx 1.019 - 0.1430D_m + 0.3165D_m^2 - 0.06498D_m^3 + 0.004163D_m^4 \tag{3.10}$$

$$K_{DP} \approx W(0.00926 - 0.0870D_m + 0.1994D_m^2 - 0.02824D_m^3 + 0.001772D_m^4) \tag{3.11}$$

$$\rho_{hv} \approx 0.9987 + 0.008289D_m - 0.01160D_m^2 + 0.0035138D_m^3 - 0.0003187D_m^4 \tag{3.12}$$

$$Z_h(x) \approx Z_x[a_{Z0}(\gamma_x) + a_{Z1}(\gamma_x)D_m + a_{Z2}(\gamma_x)D_m^2 + a_{Z3}(\gamma_x)D_m^3]^2 \tag{3.13}$$

$$Z_{dr}(x) \approx a_{d0}(\gamma_x) + a_{d1}(\gamma_x)D_m + a_{d2}(\gamma_x)D_m^2 \tag{3.14}$$

$$K_{DP} \approx \rho_a q_x[a_{K0}(\gamma_x) + a_{K1}(\gamma_x)D_m + a_{K2}(\gamma_x)D_m^2]/\rho_x \tag{3.15}$$

$$\rho_{hv} \approx a_{\rho 0}(\gamma_x) + a_{\rho 1}(\gamma_x)D_m + a_{\rho 2}(\gamma_x)D_m^2 \tag{3.16}$$

In Eq. 3.13 – 3.16, ρ_a is the density of air, q_x is the mixing ratio of the ice hydrometeor, and ρ_x is the density of the ice hydrometeor. The coefficients ($a_{x,m}$) are given in Eq. 3.17 and are dependent on the percentage of melting ($\gamma_x = q_r/(q_r + q_i)$) and fitting coefficients ($c_{x,mn}$) which are provided in Tables 1 - 3 in Zhang et al. (2021).

$$a_{x,m} = \sum_{n=1}^{N} c_{x.mn} \gamma_x^n, \tag{3.17}$$

The DSD parameters used in Zhang et al. (2021) are derived for 2-moment microphysics schemes, which assume a shape parameter of $\mu = 0$. However, for a 3-moment scheme a gamma distribution is assumed (3.18), meaning μ is variable and therefore must be taken into account in the derivation of λ and D_m. The resulting equations for the relevant DSD parameters become:

$$N(D) = N_0 D^{\mu} exp(-\lambda D), \tag{3.18}$$

$$M_k = \int N_0 D^{\mu+k} e^{-\lambda D} dD, \tag{3.19}$$

$$\lambda = [\frac{\pi \rho_x}{8 \rho_a q_x} (\mu + 3)(\mu + 2)(\mu + 1)]^{1/3}, \tag{3.20}$$

$$D_m = \frac{\mu + 4}{\lambda}. \tag{3.21}$$

The parameter μ is obtained by first calculating M_0, M_3, and M_6 using Eq. 3.19. M_6 is equal to the reflectivity factor (Z_x), M_0 is equal to N_t, and M_3 is estimated to be equal to $\frac{6}{\pi \rho_x} q_x$. Using Eq. 3.19, μ can be arranged into the following third order polynomial:

$$\begin{gathered} \mu^3 + c_1 \mu^2 + c_2 \mu + c_3 = 0; \\ c_1 = \frac{15 - 6G}{1 - G}; c_2 = \frac{74 - 11G}{1 - G}; c_3 = \frac{120 - 6G}{1 - G}; G = \frac{M_0 M_6}{M_3^2} \end{gathered} \tag{3.22}$$

Eq. 3.22 can also be found in Morrison et al. (2025). In solving for the third-order root, it is ensured that G remains greater than 1.3, else too many roots will be produced. A threshold of 10^{-20} is also applied to M_3 such that masses near zero are removed. Eqs. 3.9 – 3.16 remain unchanged for a 3-moment scheme.

3.2.4 CM1 Model Configuration

Simulations of the EF5 El Reno tornado were run using Cloud Model 1 (CM1; Bryan and Fritsch, 2002). Apart from the selected microphysics scheme, each simulation was run with the same configuration, spatial resolution (75 m horizontal and vertical resolution), and input sounding (see Table 3.2 for details). Storm motion was subtracted from the wind field to keep the domain centered on the supercell. Each simulation produced a tornadic supercell, though the genesis of the tornado varied across each microphysics scheme. Specifically, the MORR tornado began at t = 4260 s, the NSSL2 tornado at t = 5460 s, and the NSSL3 tornado at t = 8580s. Data were saved at 1-min intervals, though this study focuses on the 15-min window before tornadogenesis.

Table 3.2: Configuration of CM1 used for each simulation.

CM1 Model Configuration
Isotropic grid spacing, no stretch (75 m)
Domain: 120x120x20 km
TKE turbulence closure
5th order WENO advection
Zero surface strain surface boundary conditions (free slip)
El Reno 24 May 2011 sounding (Orf et al., 2017)
Updraft nudging (Naylor and Gilmore, 2012)
Microphysics schemes: Morrison 2-moment ($300e^{-6}$ db), NSSL 2-moment ($0.60e^{9}$ CCN), NSSL 3-moment ($0.60e^{9}$ CCN)

To assess the impact model microphysics schemes have on simulated polarimetric

radar variables, simulations with three different microphysics schemes were performed. These three schemes are the Morrison 2-moment (MORR; Morrison et al. 2005), NSSL 2-moment (NSSL2; Mansell et al. 2010), and NSSL 3-moment (NSSL3; Mansell et al. 2020) schemes. The base state of each microphysics scheme was used, where the base state is defined as the starting configuration each microphysics scheme has in CM1 v.21.1. The MORR scheme predicts 4 hydrometeor classes: cloud droplets, cloud ice, rain, and snow. Updates to the MORR scheme in 2009 further implemented a 5^{th} category for graupel, which can be run either as a single hail category or as a combined graupel and hail category (Morrison et al., 2009). The MORR scheme simulates both homogeneous and heterogeneous ice nucleation and droplet activation. Additionally, the MORR scheme allows the index of the droplet size distribution to vary throughout the storm, though the impact of entrainment and longwave radiative cooling is not accounted for in the calculations of the droplet size distribution index (Morrison et al., 2005).

In the NSSL2 scheme, N_t and q_x are predicted for 6 hydrometeor classes (droplets, rain, ice crystals, snow, graupel, and hail). This scheme was originally introduced in Ziegler (1985) for use in simulations of electrification in thunderstorms. In Mansell et al. (2010), updates to the NSSL2 scheme include the prediction of the bulk concentration of cloud condensation nuclei and the average bulk densities of graupel and hail. Frozen rain is assigned to the graupel category, which can then serve as nuclei for hail. Both wet and dry growth for ice particles are accounted for in the NSSL2 scheme, and graupel is converted to hail when the wet growth condition is met. The effects of supercooled droplets are accounted for in the wet growth of ice particles, though there is no predicted supercooled droplet category.

The NSSL3 scheme is an update to the NSSL2 scheme and implements the hail melting and shedding results from Rasmussen et al. (1984). The updated NSSL scheme

correctly reduces the mean hail diameters for large hail and produces a narrower size distribution by allowing small ice particles to melt into drops of the same mass. The NSSL3 scheme was also created to emulate how a spectral bin scheme handles melting ice hydrometeors in a size-dependent manner (Mansell et al., 2020). The updated melting of hail and graupel in the NSSL3 scheme also impacts the size of rain. These impacts are largest when the melting hail is large enough to shed small drops. The supercells produced by each microphysics scheme are shown in Fig. 3.1 at the time of tornadogenesis. The MORR scheme produces a supercell with the largest region of $Z_H > 40$ dBZ (1287 km^2) while the NSSL2 and NSSL3 schemes produce supercells with higher maximum Z_H(74 dBZ and 71 dBZ) compared to the MORR scheme (60 dBZ). Generally, the NSSL schemes produce supercells with hook echoes that stretch to the south, while the hook of the MORR supercell wraps back into the core of the storm (Fig. 3.1a–c). All three schemes produce similarly shaped horizontal velocity fields (Fig. 3.1d–e), with the MORR scheme producing the strongest maximum horizontal wind speeds (71 m s^{-1}) and the NSSL3 scheme producing the weakest maximum horizontal wind speeds (45 m s^{-1}).

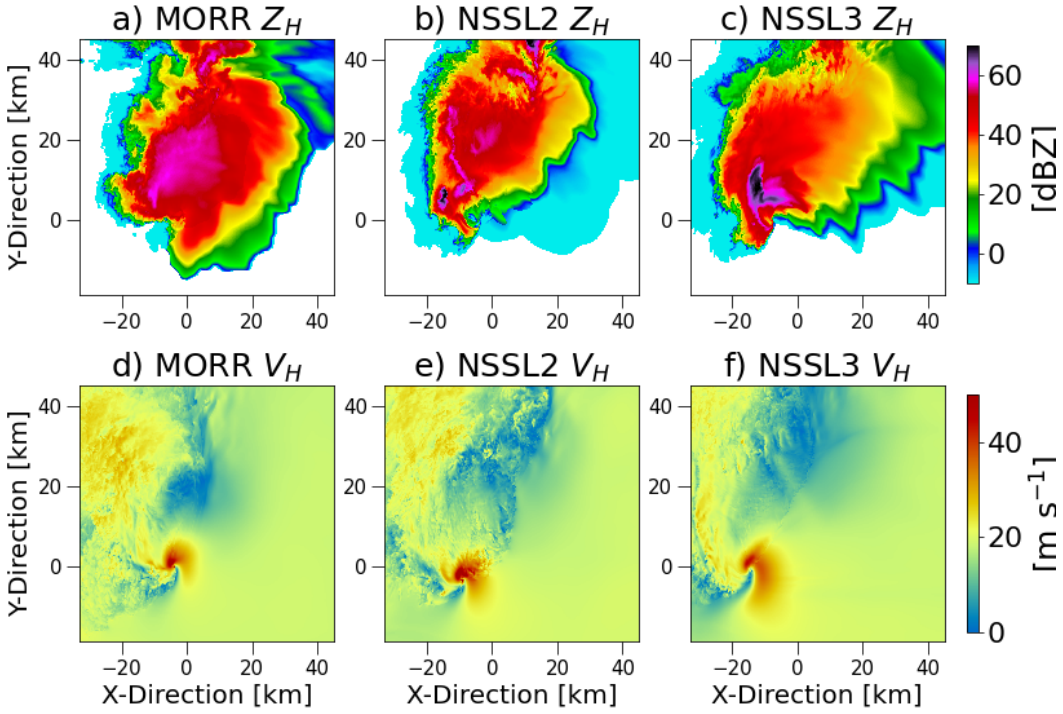


Figure 3.1: Horizontal cross-section of Z_H (a–c) and horizontal velocity (d–e) at 0.04 km AGL for the MORR, NSSL2, and NSSL3 microphysics schemes. All plots shown are taken from the time of tornadogenesis.

3.3 Results

The following results detail the output of CM1 simulations using three different melting models and microphysics schemes. The suite of simulations enables analysis of the differences in simulated polarimetric signatures and microphysics output for different PFO and melting models and intercomparisons with polarimetric radar observations.

3.3.1 Melting Model Comparison

The NSSL3 CM1 simulation was used to compare the melting models. Three different realizations of the PFO were completed at this time step, each using a different melting model. Thus, all other parameters, aside from the melting model, are the same across realizations of the PFO. The PFO was applied to one time step (the time of tornadogenesis, t = 8580 s). The time of tornadogenesis was selected to provide a comparable point of reference across the three simulations. At the time of tornadogenesis, each simulated storm is a mature supercell undergoing dynamical processes associated with tornado formation. While the internal microphysics may differ due to the different melting models tested, a similar dynamical comparison point ensures that the differences observed in each simulation are attributable to the melting models rather than to differences in supercell development.

When looking at 2D histograms of D_m and N_t, it is readily apparent that the J08 melting model has a high frequency of the maximum possible D_m allowed by the PFO for both melting hail and graupel (35 mm and 18 mm, respectively) (Fig. 3.2a,d). Meanwhile, the L24 model produces a maximum D_m of 14.7 mm for melting hail and 9.9 mm for melting graupel. The CMM model produces melting hail with a maximum D_m of 25.1 mm and 17.9 mm for graupel. The D_m of hail is often not provided in observed studies of ice hydrometeor sizes in observed supercells. However, Heymsfield

et al. (2023) obtained maximum hailstone sizes in convective updrafts, some of which were associated with supercells. Heymsfield et al. (2023) observed a maximum hail diameter of 45 mm, with the majority of hailstones having maximum diameters less than 40 mm. Given the results of Heymsfield et al. (2023), a maximum D_m of 35 mm for melting hail in the J08 simulation could imply an unrealistically large maximum hail size. However, it is challenging to definitively state the relationship between D_m and the maximum hail size without more information about the particle size distribution for hail.

According to NWS storm reports (cite), hail of 1.75" (44.5 mm) was reported in Caddo County at 1610 CST. This was approximately an hour before the genesis of the first tornado in the El Reno supercell. Storm reports during the prolific EF5 El Reno tornado were limited, but the NWS states hail sizes during the outbreak reached at least 3" (76.2 mm) in diameter. With this in mind, the J08 produces melting hail and graupel that are too large, while the L24 and CMM models better constrain the graupel and hail sizes. Between the L24 and CMM models, the CMM model primarily produces melting hail with $D_m < 10$ mm while allowing for a few occurrences of large D_m. This would generate a distribution of melting hail sizes that is mostly small, with few instances of very large hail. The L24 model generates a similar distribution, but with more limitations on the maximum hail size. For melting graupel, the CMM model likely generates values of D_m that are too large, despite these occurrences happening rarely. The L24 model is the only model that constrains the melting graupel sizes below the allowed limit for melting graupel.

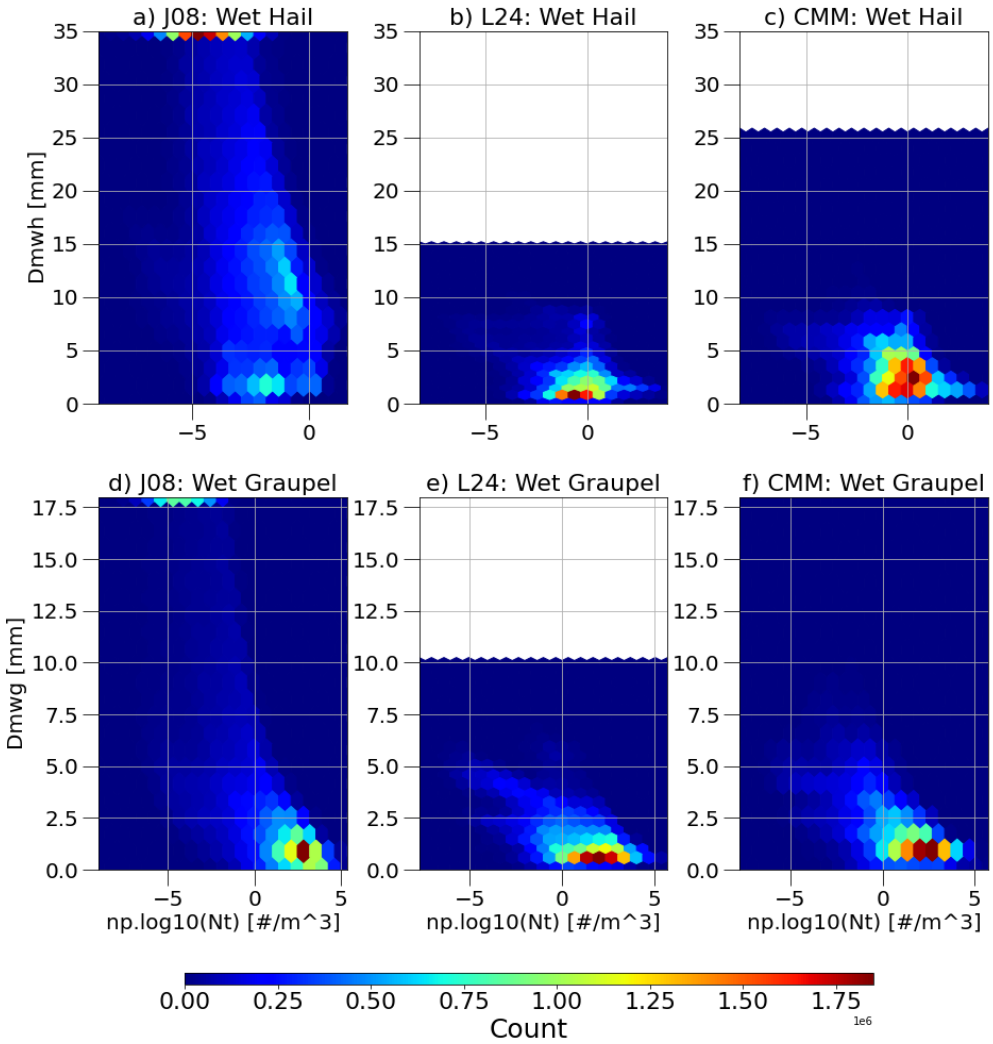


Figure 3.2: 2D histogram of the $D_{m,wh}$ (top row) and the $D_{m,wg}$ (bottom row) and N_t for the J08, L24, and CMM melting models. Values are taken from the entire depth of the supercell. Colorfill represents the frequency of the relationship between D_m and N_t.

Examining the distribution of N_t for melting graupel, the J08 model produces mixed-phase hydrometeors above the freezing level and outside the updraft core (Fig. 3.3a). The L24 and CMM models, on the other hand, limit melting graupel to below the freezing level and near the updraft core (Fig. 3.3b,c). The N_t field for melting graupel is

identical between the L24 and CMM models as they both calculate N_t using the geometric mean. A similar distribution of N_t occurs for melting hail (not shown), with J08 creating mixed-phase hydrometeors above the freezing level and the L24 and CMM models limiting the mixed-phase hydrometeors to below the freezing line.

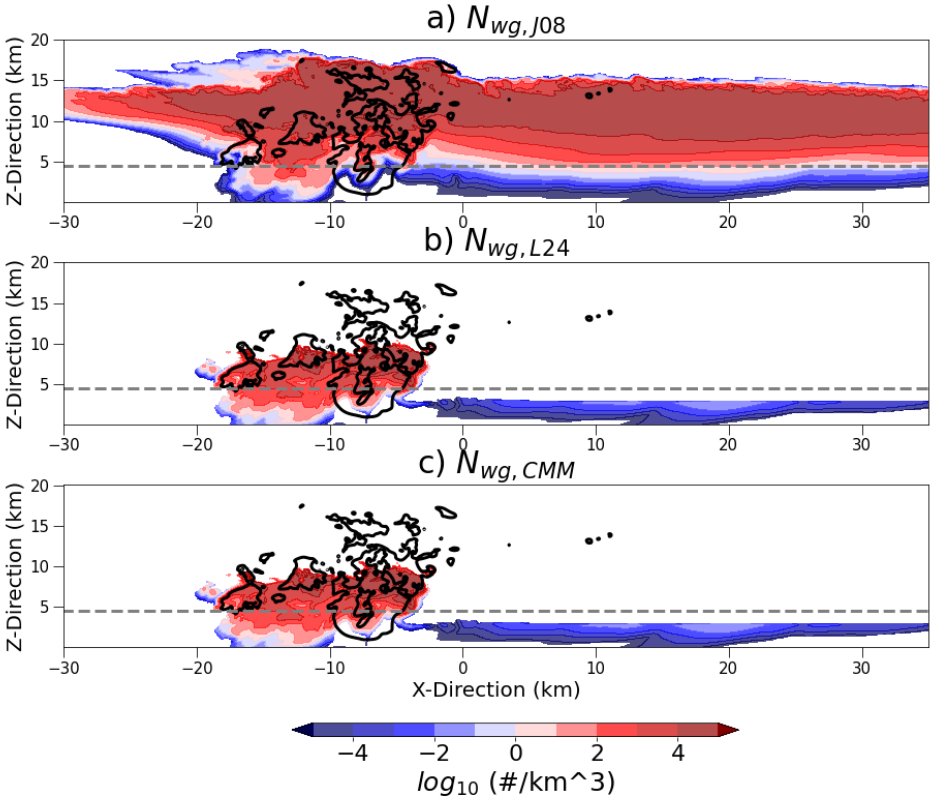


Figure 3.3: Vertical cross-section of N_{wg} on a log scale for the J08 (a), L24 (b), and CMM (c) melting models. The dashed grey line represents the freezing level. The black contour denotes the 20 ms^{-1} updraft.

Vertical cross-sections of Q_g and Q_h show the J08 and CMM models omitting dry graupel and limiting the presence of dry hail at the surface (Fig. 3.4 and 3.5). The J08 and CMM models also produce an updraft core with lower mixing ratios of dry hail and graupel compared to the L24 model (Fig. 3.4 and 3.5). The magnitude of the mixing

ratio across the three melting models is similar (Fig. 3.4 and 3.5), meaning the primary distinction is how dry ice is treated below the freezing level and within the updraft core. The distribution of Q_{wg} and Q_{wh} across each melting model is strikingly similar despite the different methods of calculating mixed-phase mixing ratios across the three models. The primary difference in the mixed-phase mixing ratios is the amount of dry ice used in the mixed ice species ($q_{x,a}$). The J08 and CMM allocate more dry ice to be used in the mixed-phase ice species in the updraft core compared to the L24 scheme. This is the reason for the reduced mass of dry ice in the updraft core, as represented in Fig. 3.5a and 3.5c.

Combining the results of Fig. 3.3 – 3.5, the CMM creates the most realistic distribution of ice hydrometeors above and below the freezing level. The CMM model restricts the melting ice species to the vicinity of the updraft core above the freezing level and reduces the mass of dry ice species below the freezing level in response to melting. The J08 and L24 models only accurately represent the distribution of the melting or dry ice species, but not both.

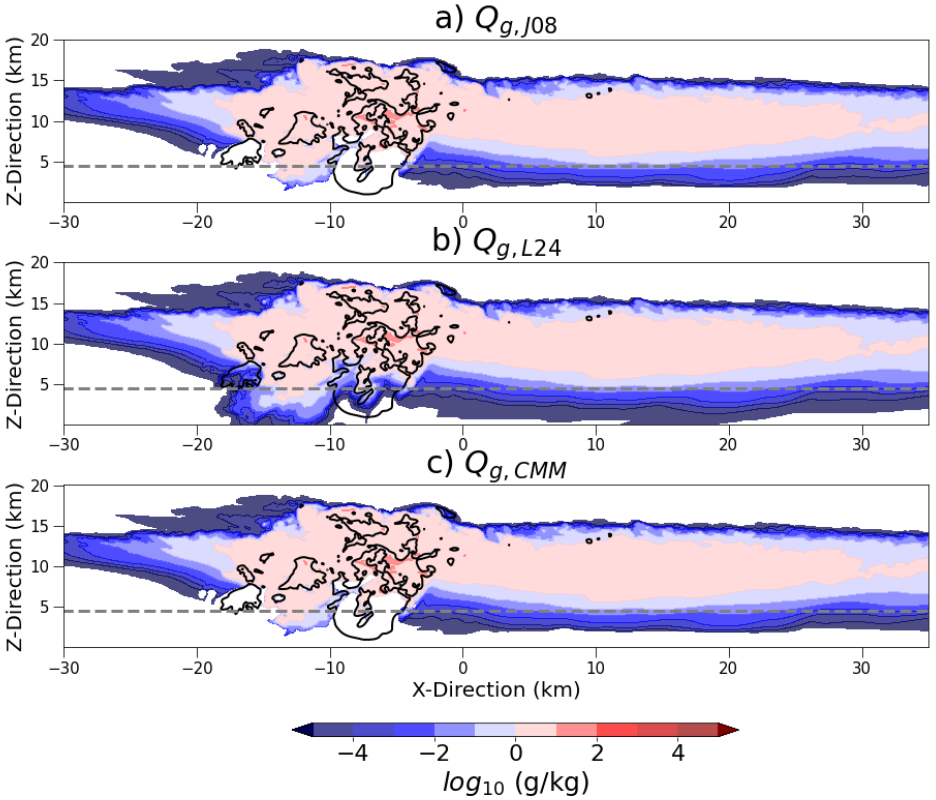


Figure 3.4: Vertical cross-section of Q_g on a log scale for the J08 (a), L24 (b), and CMM (c) melting models. The dashed grey line represents the freezing level. The black contour denotes the 20 ms^{-1} updraft.

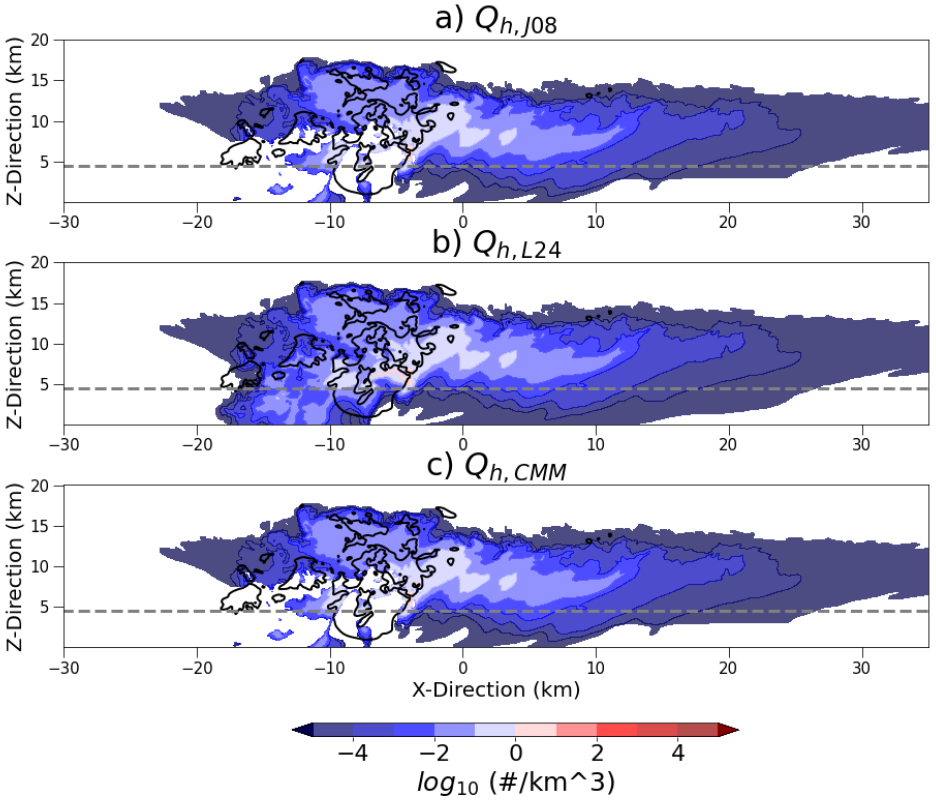


Figure 3.5: Same as Fig. 3.4 but for dry hail.

The number and size of liquid drops within the mixed-phase updraft are similar across each melting model, as the differences in the liquid water field are determined by $q_{pr} = q_r - q_{r,a}$ (Fig. 3.6). At 6-km AGL, there is a high concentration (approximately 10^6 m^{-3}) of small drops (< 0.4 mm) within the updraft core, with slightly larger drops (> 0.4 mm) in the updraft "tail" which extends from the northeastern portion of the updraft and wraps around the southwest (Fig. 3.6). In each melting model, the drop sizes decrease as they enter from the "tail" into the center of the updraft (Fig. 3.6b,d,f).

In contrast to liquid water distributions, there are notable differences in the size and number of melting hail within the updraft. The J08 scheme produces the largest

melting hail ($D_m > 6$ mm) within the updraft core, but at very low concentrations (Fig. 3.7a,b). The L24 and CMM models mostly produce melting hail with D_m less than 4 mm but at higher number concentrations (Fig. 3.7d,f). The location of wet hail curving into the updraft center reflects results from Fischer et al. (2025), which also used the MORR microphysics scheme. Dry hail entered the updraft core from the northwest corner of the updraft in each of their updraft simulations (Fischer et al., 2025). Furthermore, hail sizes grew from the northwest corner of the updraft to the updraft core, similar to what is seen in Fig. 3.7d,f.

The motion of hail into the updraft core is hard to determine from the 2D wind field; however, trajectory analyses of hail from the 24 May 2011 supercell were performed by Kumjian et al. (2021). Their trajectories showed some hail completing full circuits around the primary updraft, while other hailstones curved around the north of the updraft before falling to the surface on the western side of the updraft core (Kumjian et al., 2021). While trajectories were not calculated in this study, the path of hailstones can be inferred by the horizontal wind field, the analyses of the updraft core over time (not shown), and comparisons with the trajectories from Kumjian et al. (2021). It is evident from the horizontal wind field and the Kumjian trajectories that hail is being fed from aloft within the "tail" into the updraft center (Fig. 3.7d,f). Since the melting hail grows as it enters the updraft center in the L24 and CMM melting models, the water torus around the ice cores is likely growing as hail enters into the updraft core and melting occurs.

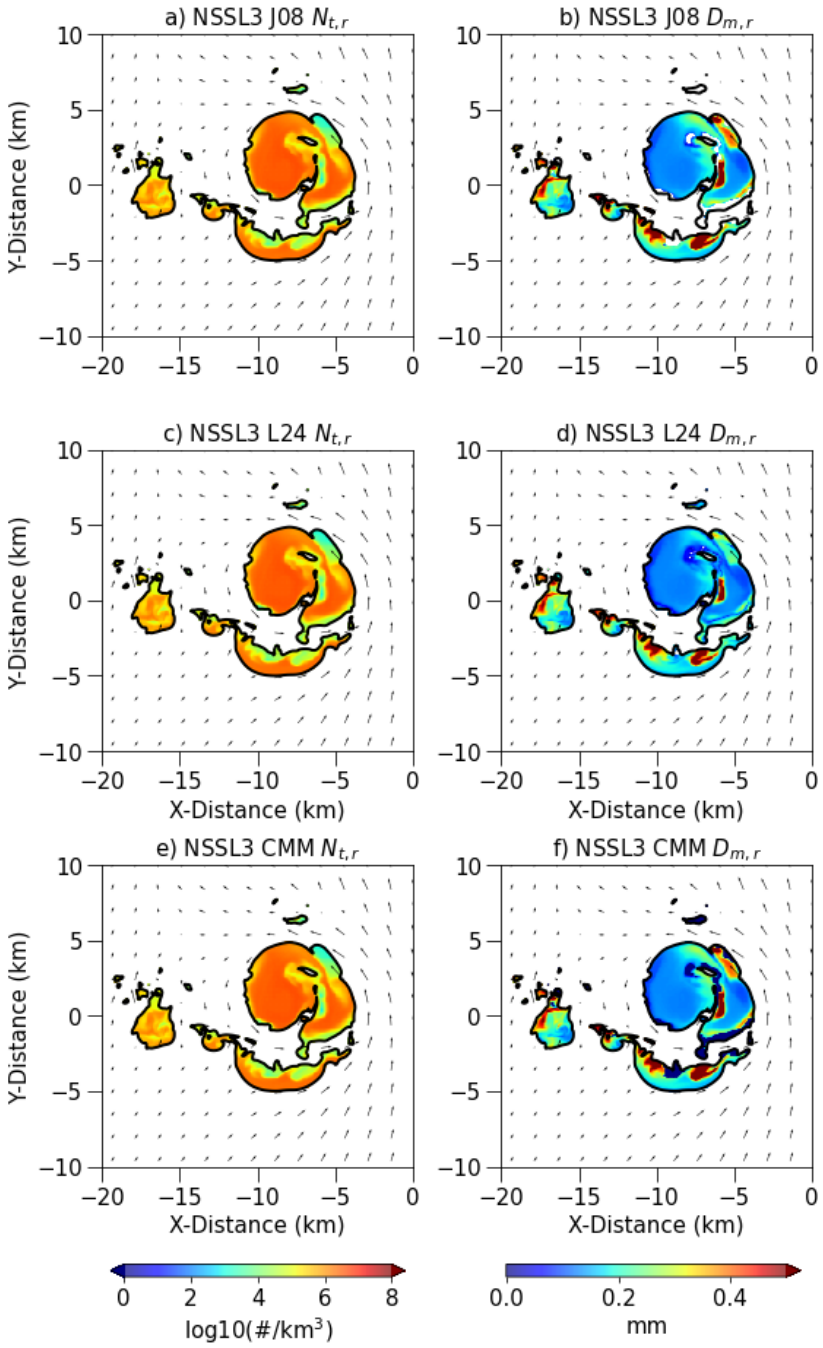


Figure 3.6: Horizontal cross sections of hydrometeor number concentration (left column) and $D_{m,r}$ (right column) for the J08 (a,b), L24 (c,d), and CMM (e,f) melting models. Black contours represent the updraft core (w > 20 ms^{-1}) and the black arrows represent the horizontal wind field. Data from 6.0 AGL is presented.

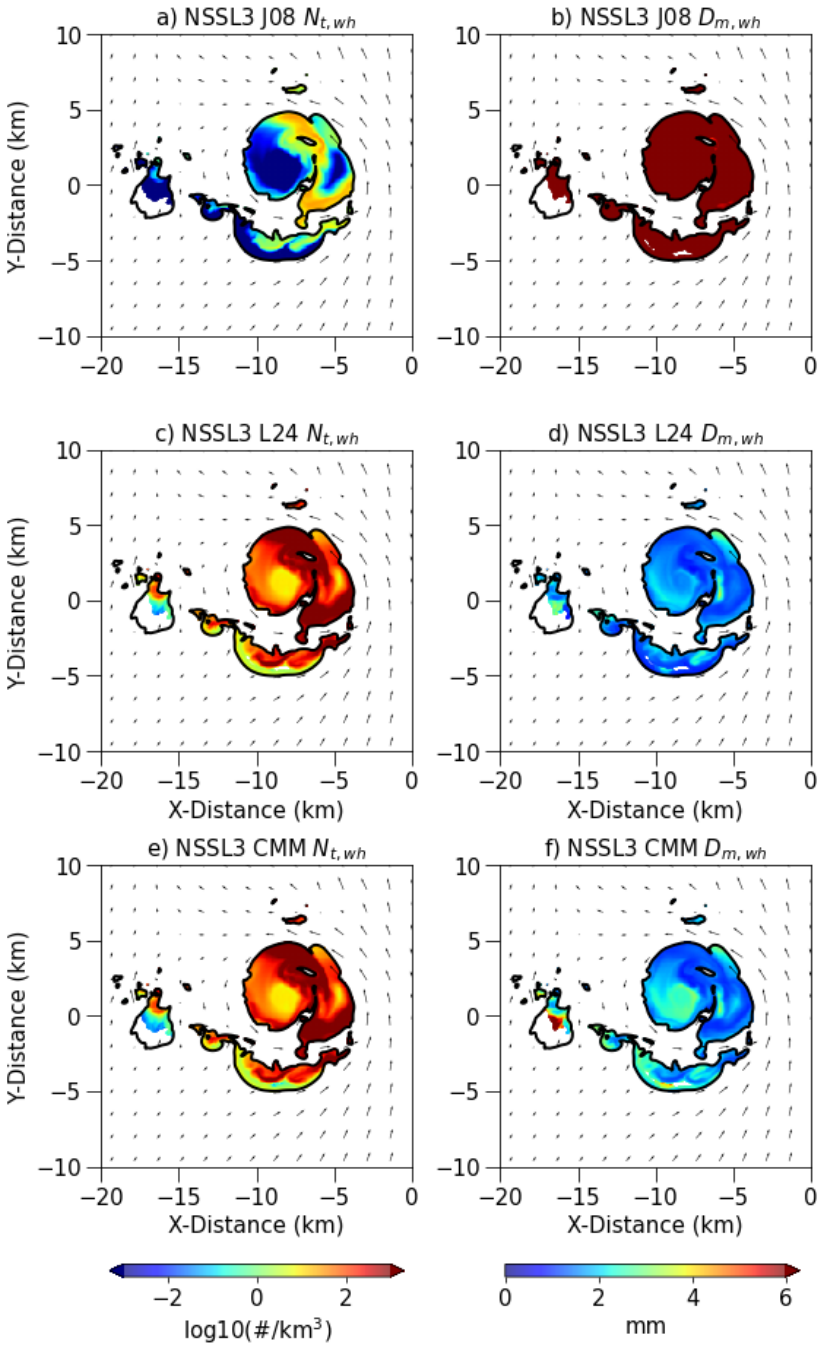


Figure 3.7: Same as Fig. 3.6 but for melting hail.

How each melting model handles the relationship between hydrometeor size and polarimetric variables can also be assessed. In reality, graupel and other rimed par-

ticles have a quasi-spherical shape (Kumjian, 2013). In the PFO, the parameterized relationships between the model output and polarimetric variables assume each rimed hydrometeor to be a sphere. For spherically shaped dry graupel, the Z_{DR} should be near 0 dB. The CMM and J08 models have Z_{DR} values that decrease with increasing graupel size (Fig. 3.8a,e). The L24 model also has this relationship, but also has higher Z_{DR} for graupel with D_m between 5 – 10 mm (Fig. 3.8c). These larger values of Z_{DR} could be occurring in bins where other hydrometeors are impacting the Z_{DR} size relationship.

In melting graupel, the presence of liquid water increases the particle's refractive index, leading to increased Z_{DR}. The Z_{DR} in small melting ice hydrometeors can exceed that of large raindrops. Increasing Z_{DR} for larger melting graupel is seen in each melting model for D_m between 0 – 5 mm (Fig. 3.8b,d,f). Larger melting ice can shed its water torus, making the liquid rim around the ice core quite thin, causing lower Z_{DR}. The thinning torus is seen in the L24 melting model, as f_g decreases as Z_{DR} decreases for melting graupel with $D_m > 5$ mm (Fig. 3.8d). The CMM model has instances of lower f_g, but primarily has f_g near 1, indicating melting graupel with a thicker liquid water torus (Fig. 3.8f). The large range of Z_{DR} for larger melting graupel in the J08 model could be due to other hydrometeors impacting the Z_{DR} relationship (Fig. 3.8b). Overall, the L24 and J08 models have a more expected relationship between D_m and Z_{DR}, with the L24 model having a more realistic relationship for dry graupel and the L24 model having a more realistic relationship for melting graupel. Similar relationships were found for dry and melting hail, with the L24 and CMM producing a more expected relationship and J08 having a larger spread of melting hail sizes (not shown).

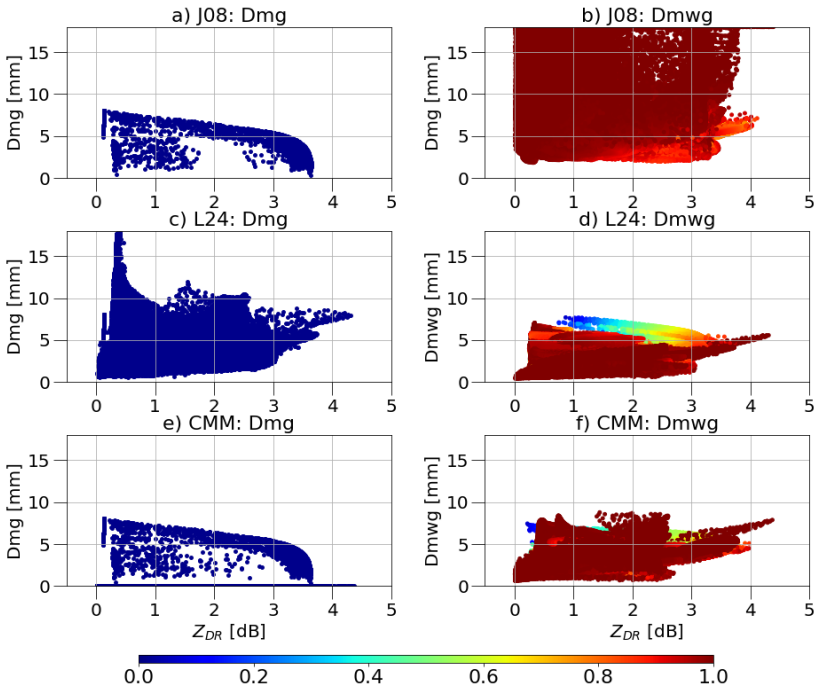


Figure 3.8: Scatter plots relating $D_{m,g}$ and $D_{m,wg}$ to Z_{DR} for the J08 (a,b), L24 (c,d), and the CMM (e,f) melting models. Colorfill represents the liquid water fraction associated with the scatter point.

The final comparison across the CMM, L24, and J08 melting models is performed across dual-polarization radar signatures each model produces (Fig. 3.9 and 3.10). Starting with the Z_{DR} arc, the L24 melting model produces an arc with 0–1 dB from -20 km to 10 km in the x-direction (Fig. 3.9b). In the J08 model, this same region exhibits higher (1–3 dB) Z_{DR} values and a sharp transition from 0–1.5 dB to 1.5–3 dB (Fig. 3.9a). The CMM produces Z_{DR} between 0–2.5 dB and a smoother transition from the lower to higher Z_{DR} values within the arc compared to the J08 model (Fig. 3.9c). Finally, each model produces a region of high (> 3 dB) Z_{DR} between 10 km and 20 km in the x-direction.

For the Z_{DR} column, the J08 model produces a column with the highest Z_{DR} values

(approximately 3 dB) compared to the other melting models (Fig. 3.10a). Also, in the "tail" of the column, the J08 model produces artifacts with negative Z_{DR}. While negative Z_{DR} is not wholly unrealistic for large hail above the freezing level, the placement of the negative Z_{DR} in the column does not line up with the location of larger hail seen in Fig. 3.7b. Meanwhile, the L24 model produces higher Z_{DR} in the "tail" of the column, with low (< 1 dB) in the core of the column (Fig. 3.10b). The CMM provides a good balance of enhanced Z_{DR} without the negative Z_{DR} artifact seen in the J08 model (Fig. 3.10c). Between the Z_{DR} arc and column, the CMM produces reasonable signatures with smoother transitions between values compared to the other melting models. The structure of the K_{DP} foot was also assessed across the three melting models, however few differences were observed in the simulated K_{DP} field (not shown).

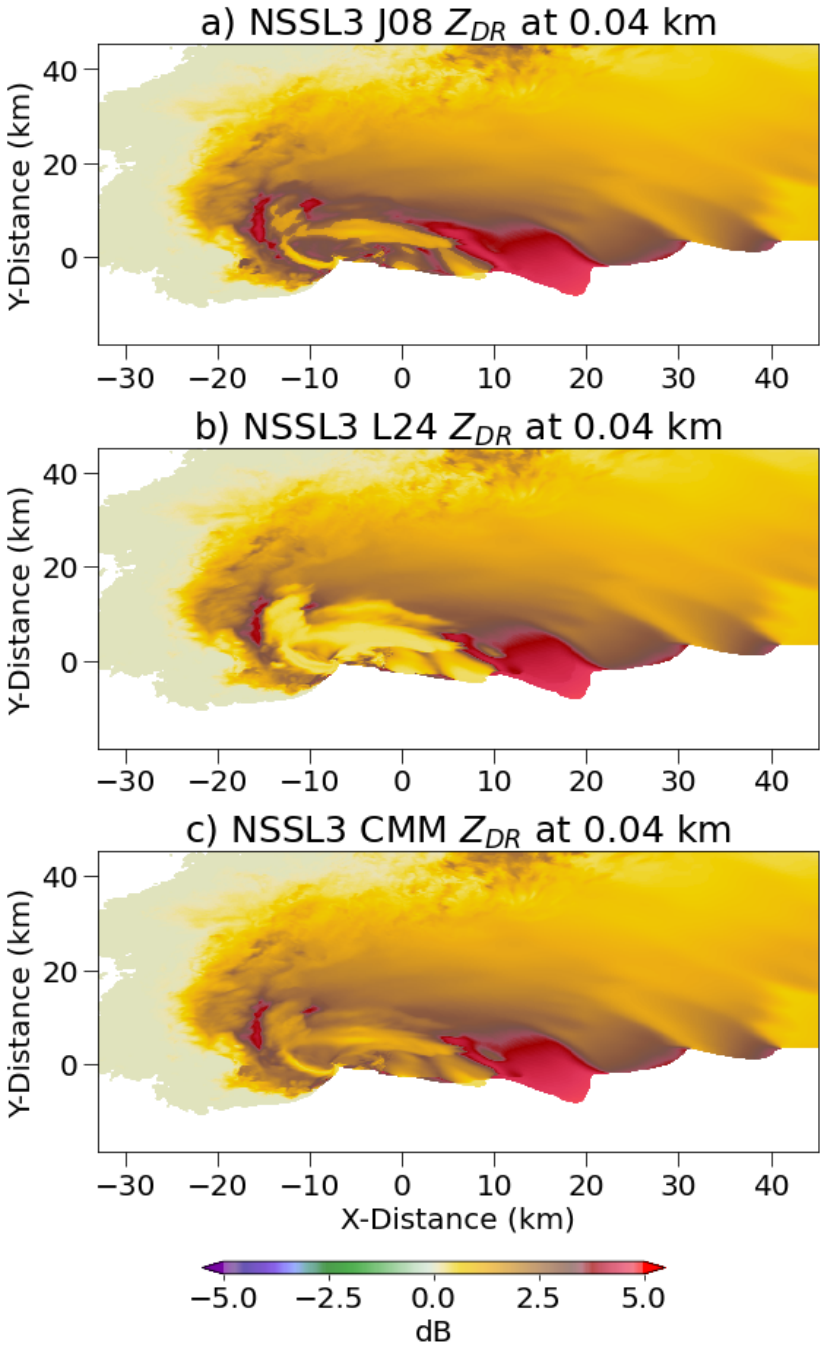


Figure 3.9: Horizontal cross-sections of Z_{DR} at 1.5 km AGL for the a) J08, b) L24, and c) CMM. Data shown are taken from the time of tornadogenesis for each melting model.

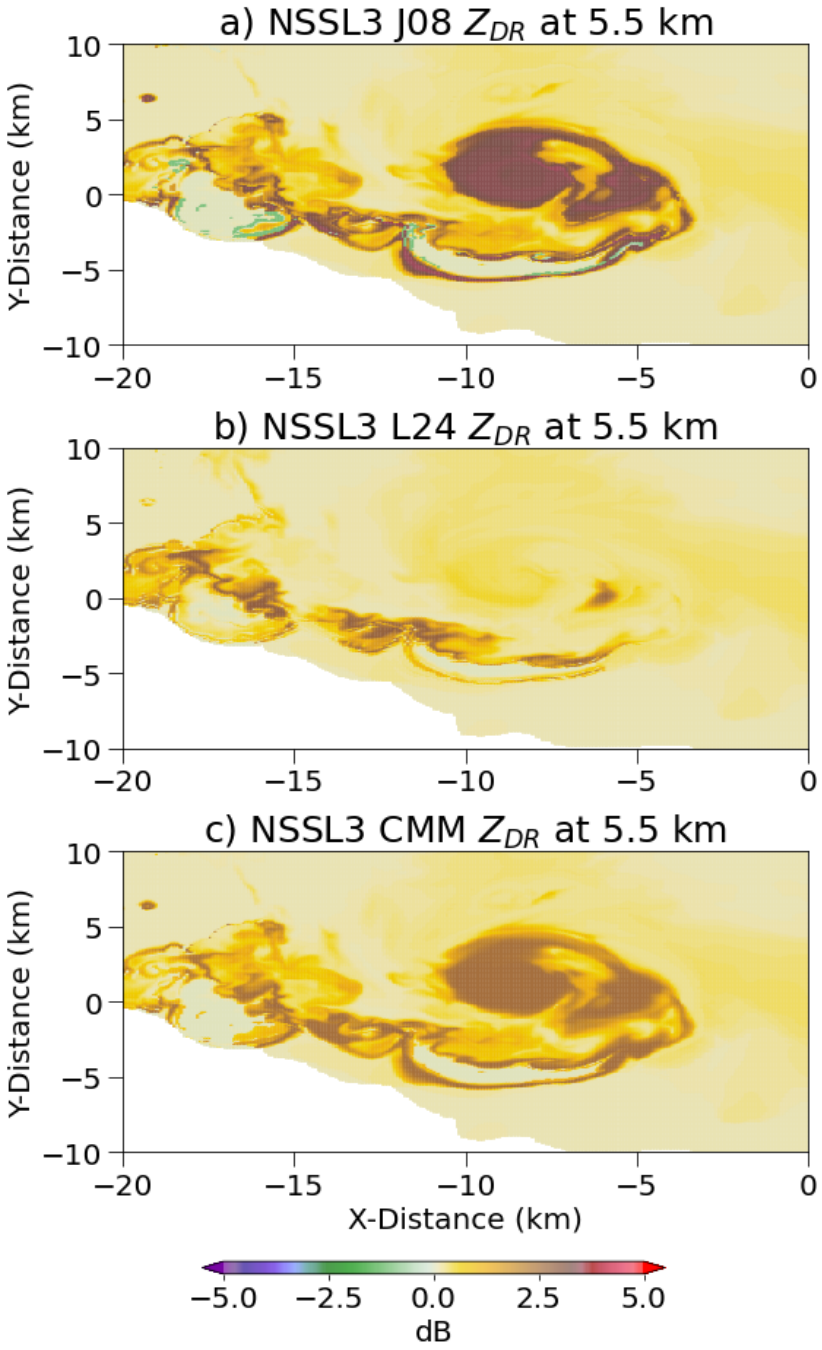


Figure 3.10: Horizontal cross-sections of Z_{DR} at 5.5 km AGL for the a) J08, b) L24, and c) CMM. Data shown are taken from the time of tornadogenesis for each melting model.

3.3.2 Microphysics Comparison to KOUN Observations

A variety of microphysics schemes are used to analyze severe convection for idealized and numerical weather prediction models. Of these microphysics schemes, the following are assessed in this study: the Morrison 2-moment, the NSSL 2-moment, and the NSSL 3-moment schemes. Polarimetric radar data from KOUN were used as a point of comparison for the output from the PFO for each microphysics scheme. In this subsection, all plots and data shown are composited over the 15-min window preceding tornadogenesis (T-15 to T-0).

In Fig. 3.11, a comparison of the 15-min composite for each microphysics scheme and three observed tornadic supercells from KOUN. Supercell B represents the supercell that produced the EF5 El Reno tornado and is the supercell from which the Orf et al. (2017) RUC sounding is taken. At the time of the genesis of the first tornado in Supercell B (2031 UTC according to NWS storm reports), the storm was approximately 80 km west of KOUN. Supercells C and D each produced an EF4 tornado up to 2 hours after the genesis of the first tornado in Supercell B. Within the 15 min window before tornadogenesis, supercells C and D were closer to KOUN and thus provided higher spatial resolution radar data of a strongly tornadic supercell during the same event as supercell B.

The MORR, NSSL2, and NSSL3 microphysics schemes produce a Z_H field with maximum $Z_H \geq 70$ dBZ, while only supercell B from the observed supercells has a maximum $Z_H \geq 60$ dBZ (Fig. 3.11). From Fig. 3.11, it is clear that the areal extent of $Z_H \geq 60$ dBZ in the simulated supercells is larger than what is seen in the observed supercells. Furthermore, the shape of each of the simulated supercells varies, with the MORR supercell having Z_H of 20 dBZ extending further south in the domain compared to the NSSL supercells (Fig. 3.11d–f). It is clear from Fig. 3.11 that

different simulations of the same supercell produce quite different outcomes in terms of the Z_H field, and a singular simulated supercell does not fully represent the storms seen in observations. Given the Orf et al. (2017) sounding was used to initiate each model run and the similarities in the Z_H field between supercell B and each microphysics scheme, only supercell B will be used as the observed comparison point for the rest of this section.

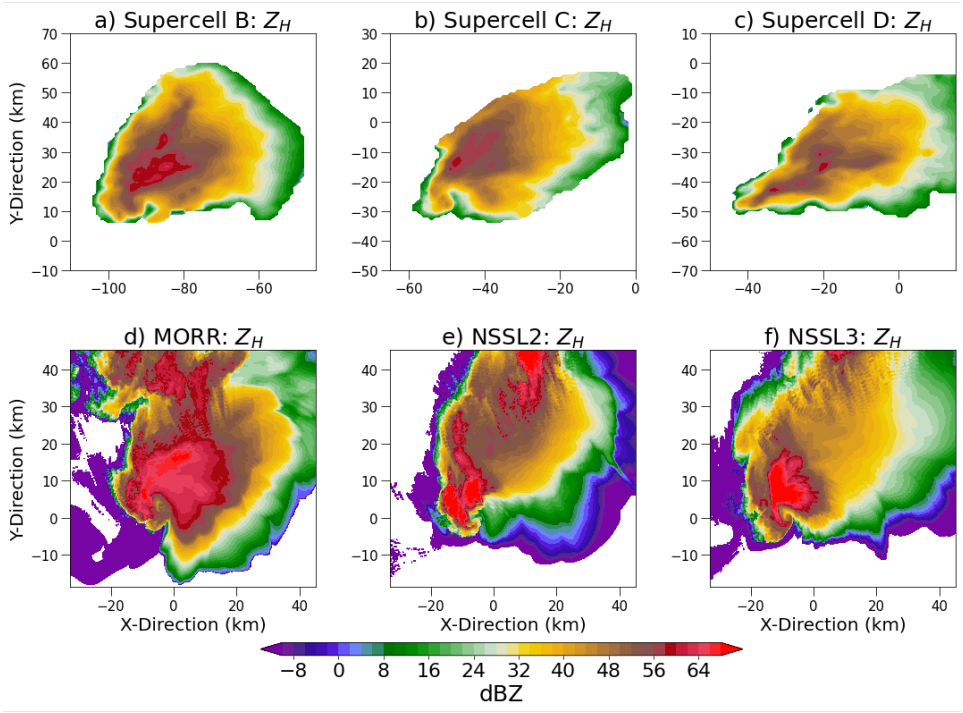


Figure 3.11: Horizontal cross sections of Z_H from KOUN (a,b,c) and from the CM1 simulations (d,e,f) at 1.5 km AGL. Both the observed and simulated supercells are shown at the time of tornadogenesis.

Each microphysics scheme handles the melting of dry graupel differently. To compare melting behavior and changes in particle size, vertical cross-sections through the center of the Z_{DR} column show the vertical profile of D_{mg} for melting and dry graupel for each microphysics scheme (Fig. 3.12). At the freezing level and above the forward flank, there is a sharp transition from larger, dry graupel (10 – 12 mm) to

larger, mixed-phase graupel (10 – 12 mm) of the same size just below the freezing level (Fig. 3.12a). The mixed-phase graupel is "created" by combining the dry graupel and liquid water fields with the assumption that the dry graupel serves as the dry ice core of the mixed-phased particle, while the liquid water forms a uniform coating around the ice core. Since the melting graupel along the freezing level matches the size of the dry graupel, it follows that the resulting mixed-phase particles have a low f_g (Fig. 3.13a). As the melting graupel falls to the surface in the MORR scheme, it reduces in size and increases its f_g (Fig. 3.12a and 3.13a). A smaller size but higher f_g indicates mixed-phase particles with smaller ice cores and more liquid water coating their surface. Thus, as the mixed-phase graupel falls to the surface, its ice core melts, effectively reducing its size and adding to the liquid water torus around its core.

In the NSSL2 and NSSL3 schemes, the mixed-phase graupel is larger at the surface compared to at the freezing level (Fig. 3.12b,c), and a growth in hail size below the freezing level is not physical. However, to the northwest of the center of the Z_{DR} column at the freezing level, a pocket of D_{mg} near 10 mm for melting graupel is present in the NSSL schemes (not shown). Given the circular trajectories of hail in Kumjian and Lombardo (2020), it is likely that the larger graupel in the NSSL simulations also followed a quasi-circular trajectory, effectively circling the north side of the updraft as it fell to the surface. This implies a minimal change in the maximum size of mixed-phase graupel between the freezing level (near 10 mm) and the surface (10 mm). Just below the freezing level, f_g is near 0, indicating the mixed-phase graupel is mostly comprised of its ice core and minimal liquid water (Fig. 3.13b,c). Unlike the MORR schemes, the f_g values transition quickly from near 0 to near 1 over a 1-km layer below the freezing level, rather than a gradual transition from the freezing level to the surface in MORR.

The largest mixed-phase graupel in the NSSL schemes occurs near the surface

and just west of the updraft core (located between -12 and 0 km in the x-direction; Fig. 3.12b,c). Meanwhile, the largest melting graupel in the MORR scheme occurs at 0 km in the x-direction and at the freezing level (Fig. 3.12a). The location of the largest mixed-phase hydrometeors is in part governed by Q_r (Fig. 3.14). The MORR scheme has a deeper layer of relatively high Q_r collocated with the region of largest melting graupel (Fig. 3.14a). In the NSSL schemes, the Q_r field is distributed more evenly along the x-axis, with higher values of Q_r extending closer to the surface in the NSSL3 scheme (Fig. 3.14b,c). The higher Q_r values in the NSSL schemes are somewhat collocated with larger dry graupel that is just west of the updraft (Fig. 3.12b,c). Therefore, the distribution of the Q_r field and the location of larger dry graupel (which serve as the ice cores for mixed-phase graupel) determine the location of the larger melting graupel in each of the three microphysics schemes.

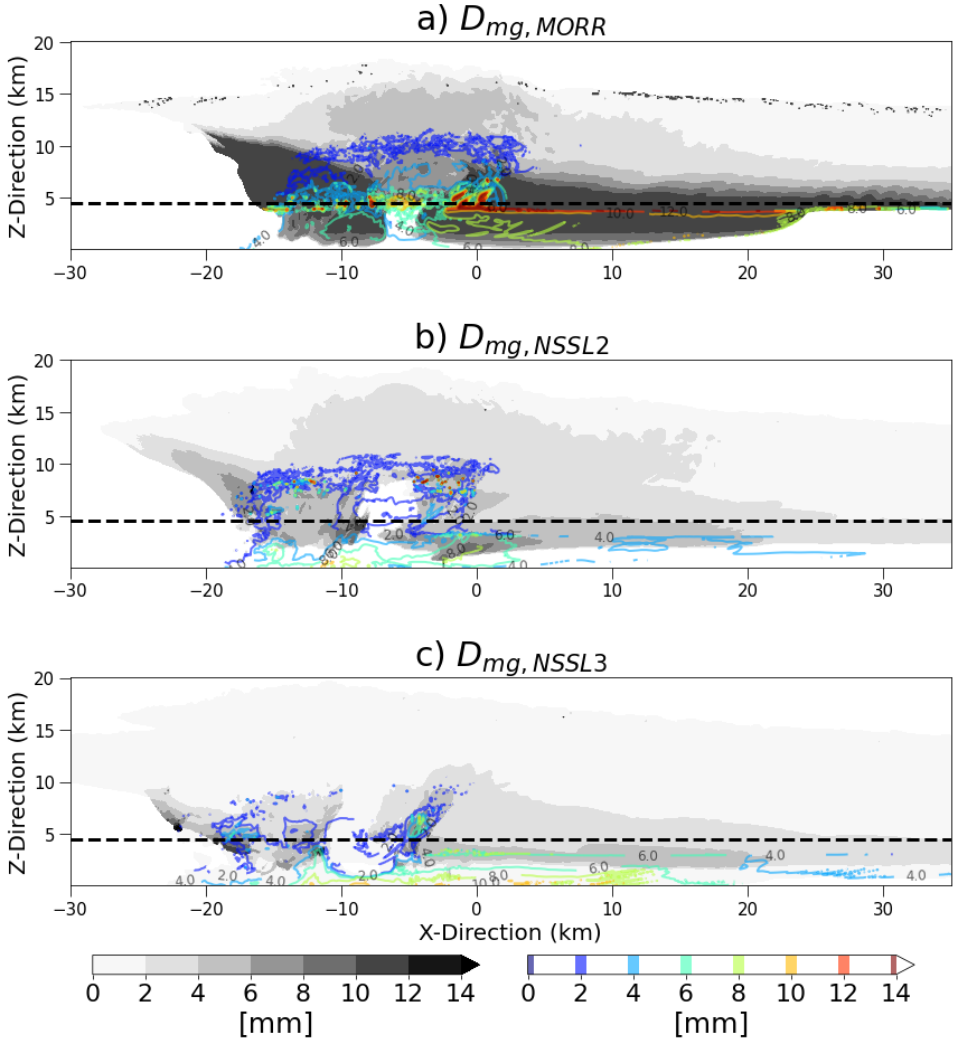


Figure 3.12: Vertical cross-section through the center of the Z_{DR} column for the MORR (a), NSSL2 (b), and NSSL3 (c) schemes. The data shown in this plot represent a 15-min composite. Grey colorfill represents the D_m for dry graupel. Colored contour lines represent the D_m of melting graupel. Black dashed line represents the freezing level at 4.5 km AGL.

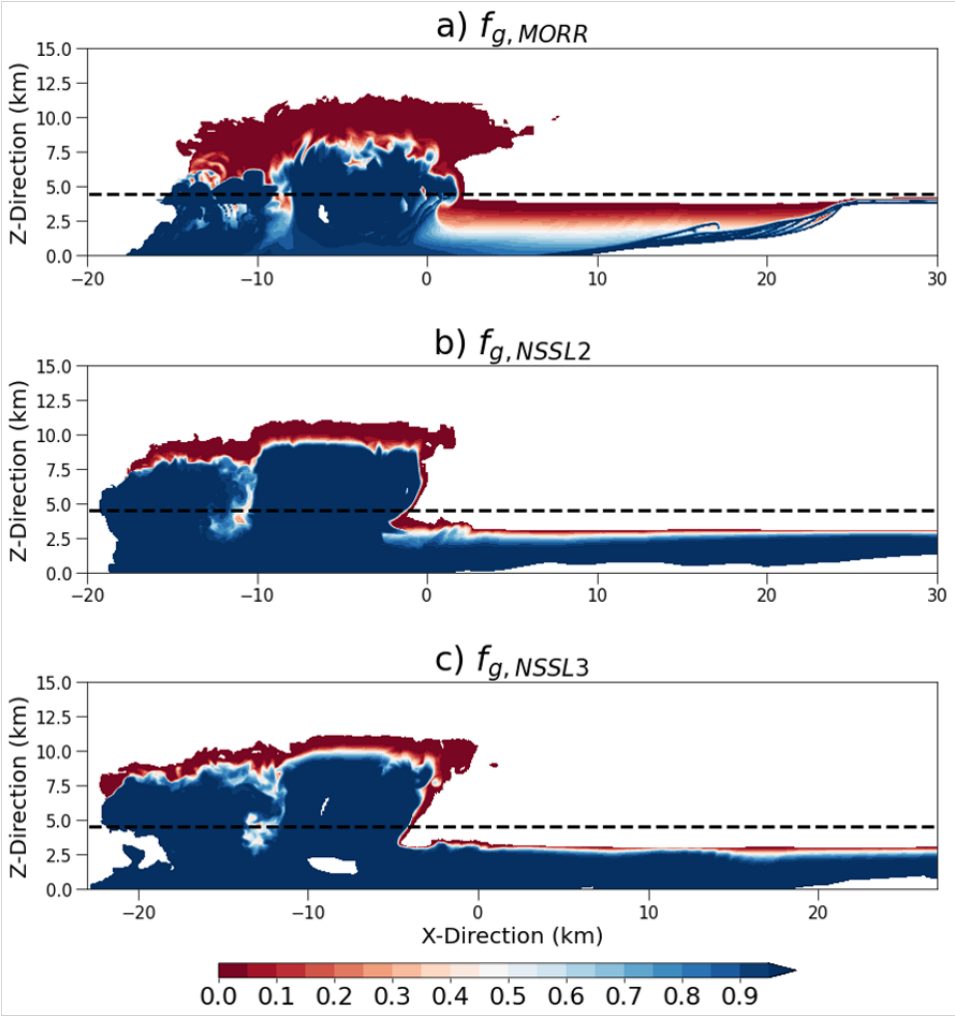


Figure 3.13: Cross-section through the center of the Z_{DR} column for the MORR (a), NSSL2 (b), and NSSL3 (c) schemes. Colorfill represents f_g, and the freezing level (4.5 km AGL) is represented by the black dashed line.

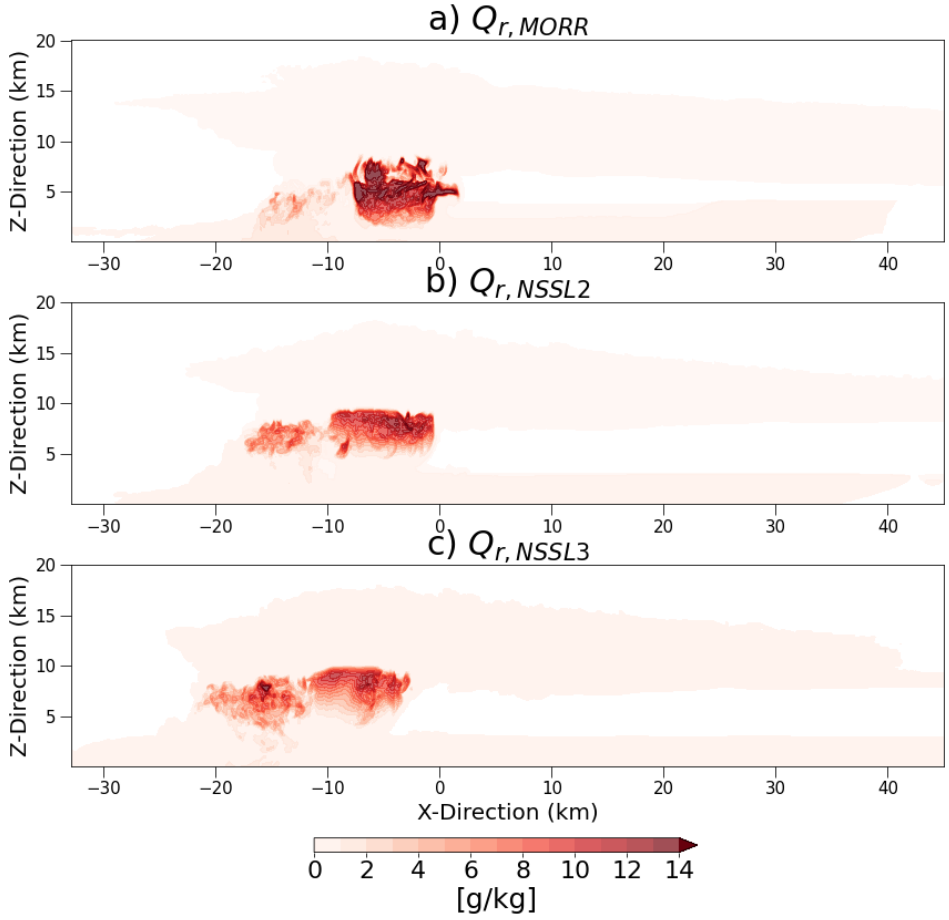


Figure 3.14: Cross-section through the center of the Z_{DR} column for the MORR (a), NSSL2 (b), and NSSL3 (c) schemes. Colorfill represents Q_r, and the freezing level (4.5 km AGL) is represented by the black dashed line.

3.3.2.1 Polarimetric Signature Intercomparison

To compare the model output from each microphysics scheme to the KOUN observations, areal calculations were made for the storm size and the size of the Z_{DR} arc, Z_{DR} column, and K_{DP} foot (Table 3.3). The calculations in Table 3.3 are performed on the 15-min composite averages of observations and model output, and the area of each supercell is based on reflectivity of $Z_H > 20$ dBZ unless noted otherwise. The 20 dBZ threshold is only used for the area calculations and not for the plots of the

composited Z_H from simulations and observations.

The MORR scheme produces the largest supercell, with a 20-dBZ area that is almost 1000 km^2 larger than the observed supercell (Table 3.3). The NSSL2 scheme matched the size of the observed storm remarkably well, with only a 5.3 km^2 difference between the simulated and observed supercell (Table 3.3). Examining the spatial extent of $Z_H = 30$ dBZ, the NSSL2 scheme extends the supercell farther to the northeast compared to the observed supercell (Fig. 3.15a). Meanwhile, the NSSL3 scheme also extends the supercell farther to the northeast, but also underestimates the width of the forward flank downdraft precipitation (Fig. 3.15a). Based on a 50-dBZ threshold of Z_H, the MORR scheme creates a forward flank with enhanced Z_H compared to observations (Fig. 3.15b). The NSSL3 scheme extends the higher Z_H values to the northeast, matching the general orientation of the 50-dBZ contour of the observed storm (Fig. 3.15b). While the NSSL2 scheme matches the east-northeast orientation of the lower Z_H values to observations, the NSSL2 scheme exhibits an east-southeast orientation of the 50-dBZ contour in the forward-flank downdraft (Fig. 3.15b). Finally, all schemes produced narrower hook echoes compared to the observed supercell, although this is possibly due to the higher spatial resolution of the model data (Fig. 3.15b).

Table 3.3: List of values of supercell and polarimetric areas. All areas were calculated using the 15-min composites of the simulated and observed data. The supercell area provided is valid for 1.5 km AGL. Each of the polarimetric signature areas are normalized by storm size at 1.5 km AGL (or 5.5 km AGL for the Z_{DR} column).

	Supercell Area (km^2)	Ratio of $Z_{DR} > 3$ dB to Storm Size	Ratio of $K_{DP} > 3$ deg/km to Storm Size	Ratio of $Z_{DR} > 1$ dB to Storm Size
MORR	2780.0	0.78	0.027	0.085
NSSL2	1865.3	0.83	0.080	0.175
NSSL3	2490.0	0.13	0.0027	0.181
OBS	1860.0	0.25	0.0	0.090

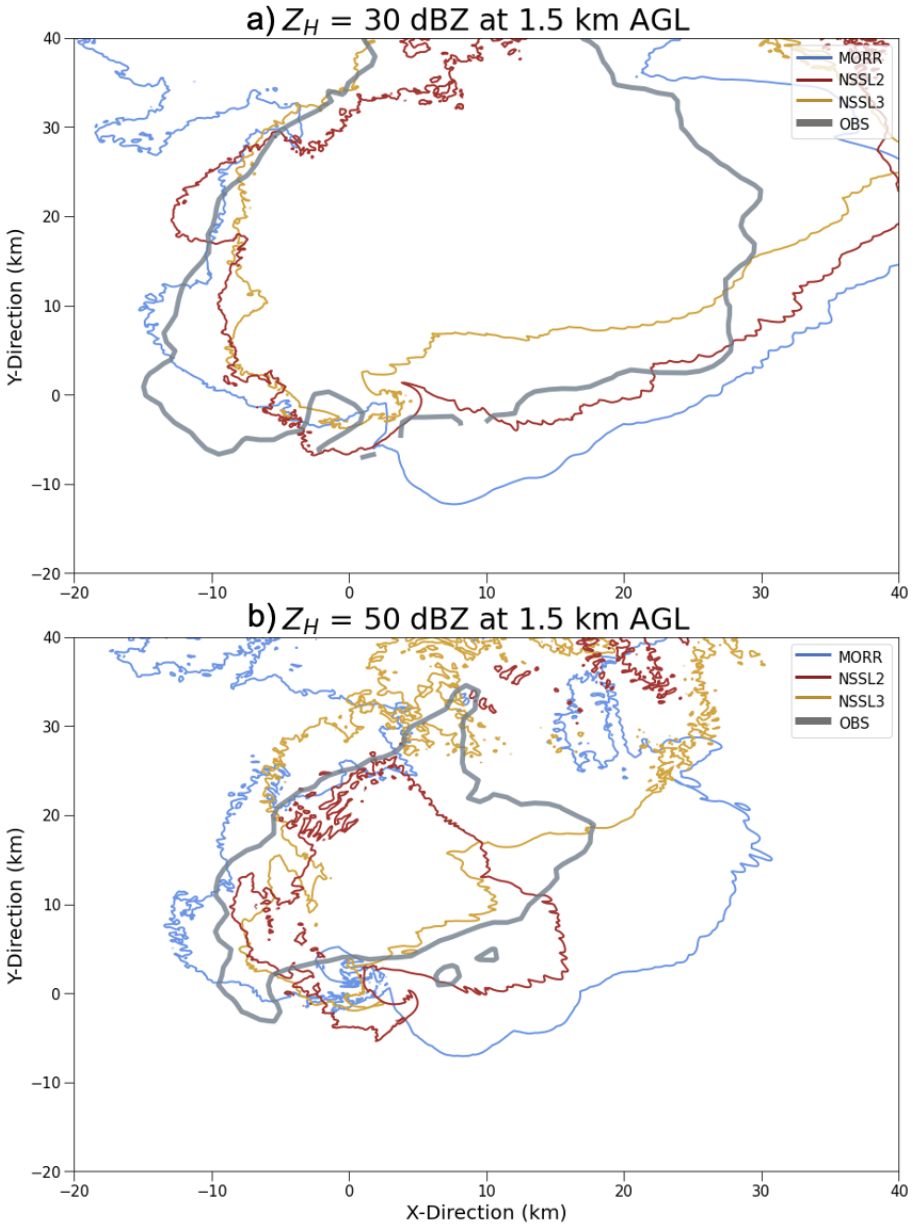


Figure 3.15: Contours of Z_H = 30 dBZ (a) and Z_H =50 dBZ (b) at 1.5 km AGL from the MORR (blue), NSSL2 (red), NSSL3 (gold), and observed (grey) datasets.

The individual polarimetric signatures from the model data can also be compared to the KOUN observations. The Z_{DR} column is a region of enhanced Z_{DR} ($>$ 1 dB) above the freezing level that represents supercooled drops that have been lofted above

the freezing level by the updraft. Vertical cross-sections through the Z_{DR} column are provided in Fig. 3.16 for each microphysics scheme and radar observations.

The observed Z_{DR} column extends to 8.0 km AGL and the region of $Z_{DR} > 3$ dB becomes narrower with height (Fig. 3.16g). Meanwhile, the MORR column reaches a height of 8.3 km AGL, the NSSL2 column reaches 9.6 km AGL, and the NSSL3 column reaches 10.7 km AGL (Fig. 3.16a,c,e). Each of these heights was calculated as the highest height where $Z_{DR} > 1$ dB and was vertically continuous. While the MORR scheme best captures the observed Z_{DR} column height, it does not reproduce the narrowing of the $Z_{DR} > 3$ dB region with height (Fig. 3.16a,g). The NSSL3 column does not produce $Z_{DR} > 3$ dB above the freezing level, which is seen in the observed column, and the NSSL2 column produces a near uniform field of $Z_{DR} > 4$ dB throughout the primary column between x = -10 km and x = 0 km (Fig. 3.16c,e,g).

At 1 km above the freezing level, the area of the Z_{DR} columns is compared (Table 3.3). The MORR scheme best represents the area of the observed Z_{DR} column, while the NSSL schemes create larger Z_{DR} columns than the observations. As shown in Fig. 3.16, each simulated supercell produces a secondary column to the west of the primary column. Evidence of a smaller region of enhanced Z_{DR} is present in the observations at -100 km, but this feature is overrepresented in the simulations (Fig. 3.16). Thus, none of the simulated columns fully represent the observed column, though the MORR scheme best reproduces the height and area of the observed column.

The distribution of q_r and q_{g+h} is examined to assess the hydrometeor distributions in the Z_{DR} column (Fig. 3.17). The distribution of q_r and q_{g+h} is given in Fig. 3.17. A combined mixing ratio for graupel and hail (q_{g+h}) is used since the MORR scheme combines graupel and hail into one ice category. Based on previous simulation research, the Z_{DR} column is expected to consist partition these hydrometeor types separately. From previous simulation research, it is expected that the Z_{DR} column is composed of

rain, supercooled drops, graupel, and hail (Kumjian et al., 2014). In Kumjian et al. (2014), the simulated column had rain primarily throughout its core with supercooled drops at the top of the column. In each of the simulated columns in this study, there is no supercooled drop field. Thus, it is primarily a combination of hail, graupel, and rain at the top of each of the columns (Fig. 3.17).

In Kumjian et al. (2014), the q_h field descends 1 – 2 km into the top of the Z_{DR} column. The majority of the q_h field in Kumjian et al. (2014) is located to the west of the column. In our study, the q_{g+h} field in the MORR simulation descends 3 – 4 km into the top of the simulated column (Fig. 3.17a). The q_{g+h} field in the NSSL2 simulation only descends approximately 1 km into the top of the column, though descends deeper into the eastern and western portions of the column and creates an arc-like shape at the top of the column (Fig. 3.17b). This arc feature is more pronounced in the NSSL3 simulation, with the q_{g+h} field penetrating near 6 km into the core of the column (Fig. 3.17c). It is possible that the updraft in the NSSL schemes pushes the hail and graupel to the sides of the column, as it is thought that the largest hailstones have a small residency time in the updraft core (Heymsfield et al., 2023).

To examine the vertical distribution of Z_H, vertical cross-sections are provided in Fig. 3.16b,d,f,h. The x-axis in these cross-sections differs from those in Fig. 3.16a,c,e,g as the view is expanded for the Z_H field to observe the entire supercell. When examining vertical cross-sections of the Z_H field, the MORR scheme produces a larger region of $Z_H > 55$ dBZ compared to observations (Fig. 3.16b,h). The NSSL schemes capture the vertical column of $Z_H > 55$ dBZ that then spreads eastward and into the supercell anvil (Fig. 3.16d,f,h). The arch-like structure of $Z_H > 60$ dBZ enveloping a local minimum of Z_H is referred to as a bounded weak echo region (BWER; Pal et al., 2006). A BWER is a radar signature often associated with a strong updraft and results from hydrometeors being "pushed" out of the updraft core by strong vertical winds, effectively reducing

Z_H and creating the local Z_H minimum. The NSSL schemes best reproduce the BWER observed in the supercell, with the MORR scheme producing high values (> 60 dBZ) that are likely within the updraft core (Fig. 3.16b,d,f,h). Finally, the NSSL2 scheme produces Z_H > 30 dBZ that stretches into the anvil of the supercell, similar to what is seen in the observed storm (Fig. 3.16d,h).

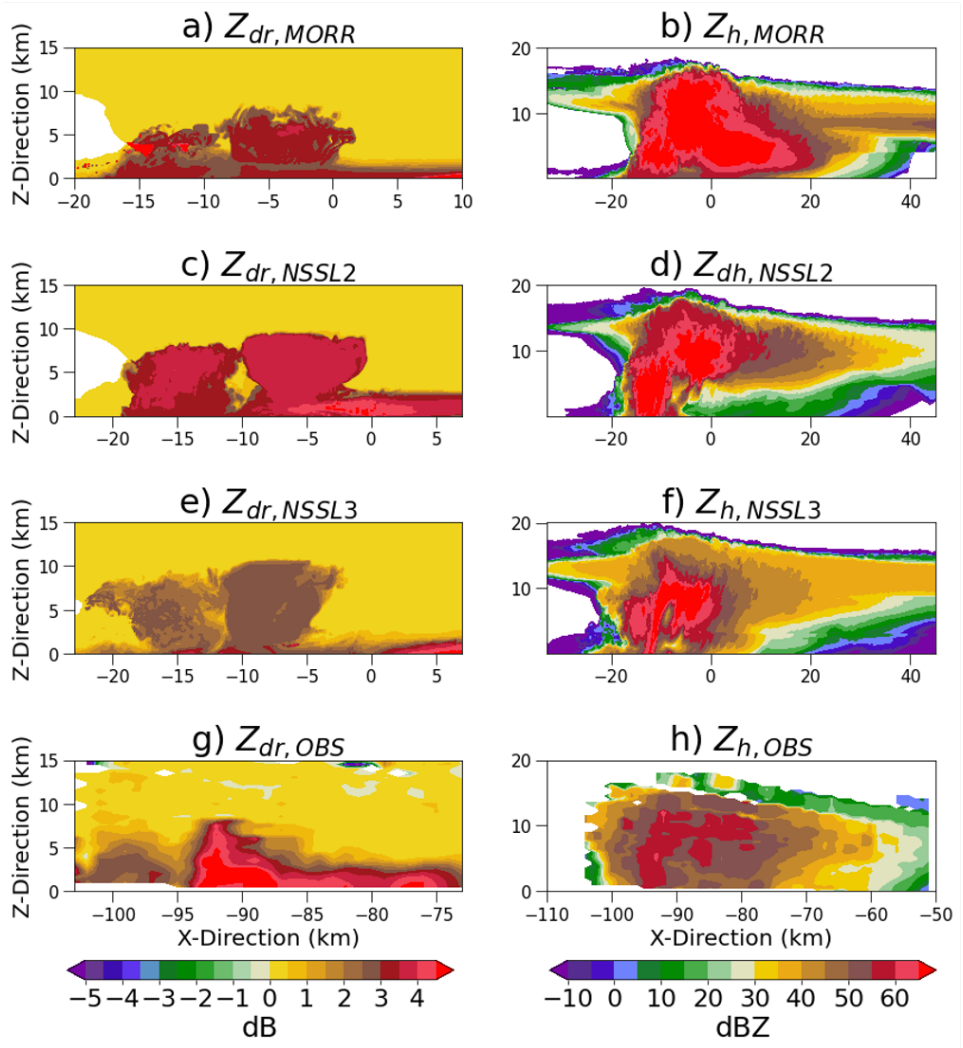


Figure 3.16: Vertical cross-sections through the center of the Z_{DR} column for the MORR (a,b), NSSL2 (c,d), NSSL3 (e,f), and observed (g,h) composited datasets. Cross-sections in the left column are zoomed in to focus on the Z_{DR} column.

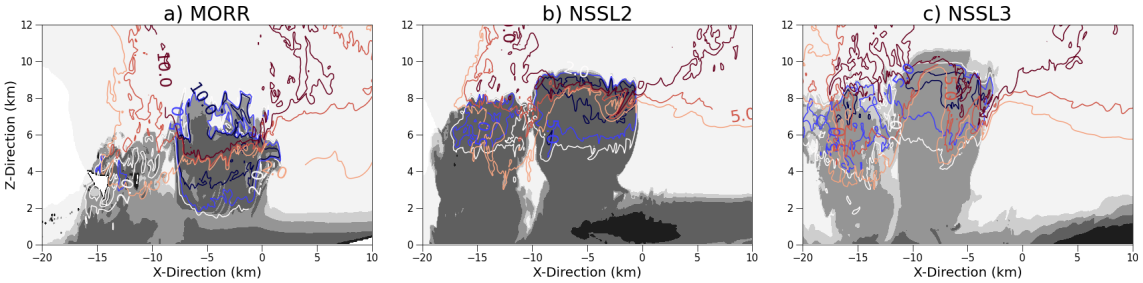


Figure 3.17: Cross-section through the Z_{DR} column for the a) MORR, b) NSSL2, and c) NSSL3 schemes. Red contours represent the q_{g+h} field. Blue contours represent the q_r field. Contour lines represent the 2, 5, and 10 g/kg levels.

When comparing the areal extent of K_{DP} foot and Z_{DR} arc, the NSSL3 scheme produces polarimetric signatures with comparable sizes to the observed signatures (Table 3.3). The NSSL2 and MORR schemes create Z_{DR} arcs and K_{DP} foots that are too large, while the observed K_{DP} foot does not exceed values of 3 deg/km. The lower K_{DP} values in observations are likely due to two factors: 1) the smoothing of the peak magnitudes from a combination of K_{DP} estimation and Cartesian gridding, and 2) the lower spatial resolution of the observed data.

Visually, the large Z_{DR} arcs can be seen in Fig. 3.18. The MORR scheme produces both excessively high values of Z_{DR} (>5 dB) and an arc that stretches into the northeastern corners of the supercell (Fig. 3.18a), which is not observed here or in other ZDR arc cases (Kumjian and Ryzhkov, 2008; Palmer et al., 2011). This distribution of Z_{DR} is largely due to the excessive size sorting that occurs within the MORR scheme, essentially producing a region of lower Z_{DR} primarily comprised of graupel (x=0–20 km, y=0–10 km) and a large region of higher Z_{DR} comprised mostly of larger drops (x=0–43 km, y=-30–40 km).

The NSSL3 scheme produces an arc with the lowest Z_{DR} values across the three simulated arcs (Fig. 3.18a,c,e). The NSSL3 arc has a consistent Z_{DR} "hole," which is a region of low Z_{DR} (near 1 dB) that consists primarily of relatively low concentrations

of large melting hail (D_m=5.0 – 10.0 mm) and graupel (D_m=5.0–9.0 mm) (Fig. 3.18e). While a Z_{DR} "hole" is seen in the observed supercell, it appears earlier than the 15-min window before tornadogenesis (not shown). Due to the large presence of hail within the Z_{DR}arc, the enhanced Z_{DR} is primarily constrained to the eastern side of the forward flank (Fig. 3.18e). Thus, the observed arc is best represented by the NSSL2 and NSSL3 schemes, though each NSSL scheme contains elements of the arc that are either not captured by observations or are unrealistic.

The NSSL2 scheme implements more constraints on size sorting compared to the MORR scheme, producing a more realistic Z_{DR} arc shape (Fig. 3.18b). However, the arc in the NSSL2 scheme extends too far to the east of the supercell compared to the observed storm (Fig. 3.18c,g). Examining the Z_{DR} arc at each time step (not shown), the NSSL2 Z_{DR} arc begins near the mesocyclone and moves eastward in a storm-relative sense. When looking at the composite in Fig. 3.18c, the eastward propagation of the arc appears as a large region of enhanced Z_{DR} along the entire forward flank. This eastward propagation of the Z_{DR}arc is not captured in the observed supercell (Fig. 3.18g). However, this could be attributed to the coarser temporal resolution of the KOUN compared to the simulated data.

The K_{DP} foot represents the region within the lower levels of a supercell with high liquid water content and subsequent negative buoyancy (Carlin and Ryzhkov, 2019). Each of the simulated K_{DP} fields produces a K_{DP} foot that stretches from the hook echo of the supercell up to the northeast corner of the supercell (Fig. 3.18b,d,f). Although at lower spatial resolution, this southwest-to-northeast orientation is also seen in KOUN observations K_{DP} foot (Fig. 3.18h). As previously mentioned, the magnitude of K_{DP} is lower in the observed supercell compared to the simulated storms due to differences in the spatial resolution of the data and the interpolation of the observed data to a Cartesian grid. That being said, the NSSL3 scheme produces a K_{DP} foot with generally

lower K_{DP} than in the MORR and NSSL2 K_{DP} foots (Fig. 3.18b,d,f).

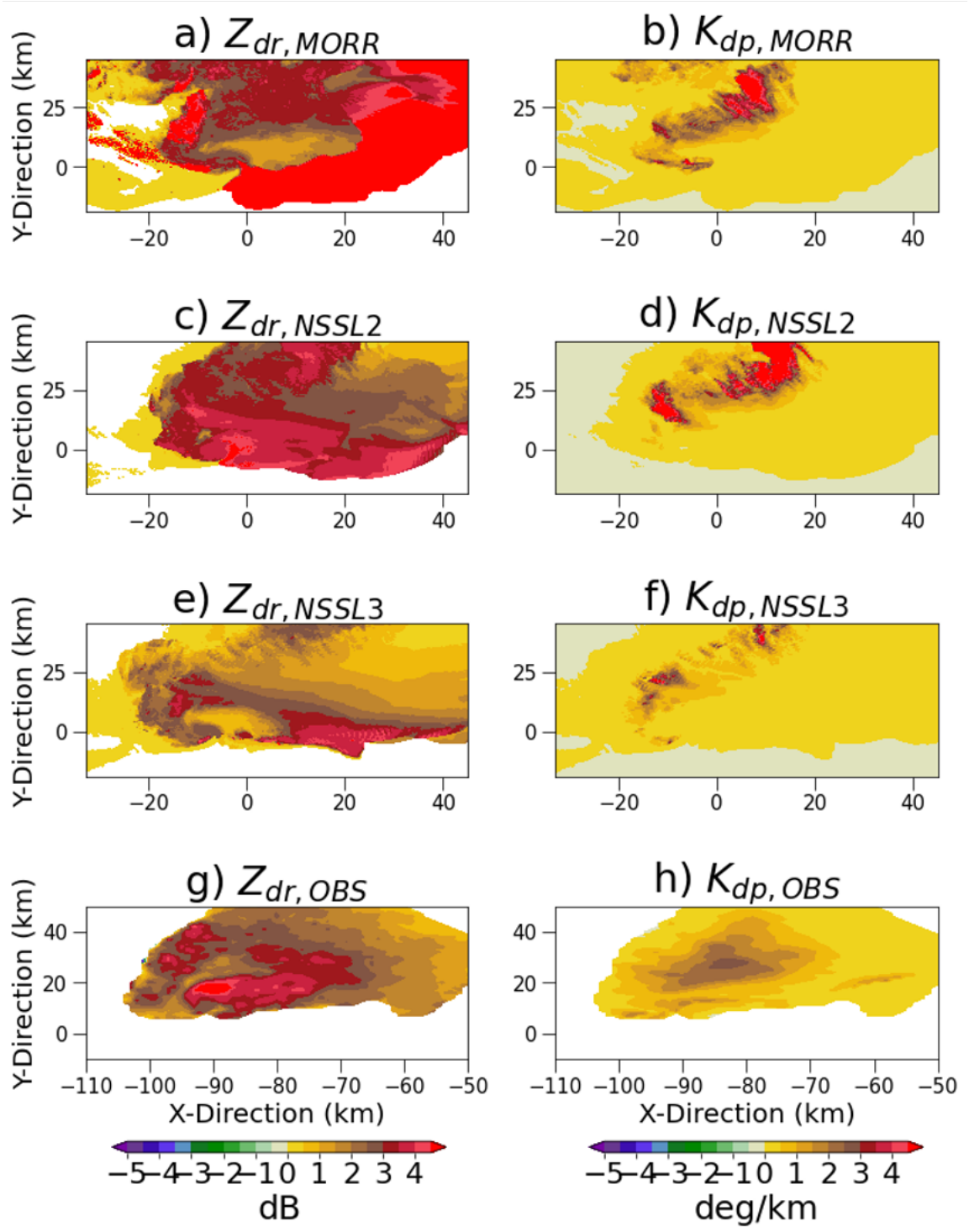


Figure 3.18: Horizontal cross sections of Z_{DR} (a,c,e,g) and Z_H (b,d,f,h) at 1.5 km AGL for the MORR (a,b), NSSL2 (c,d), NSSL3 (e,f), and the observed (g,h) composited datasets.

Contoured Frequency by Altitude Diagrams (CFADs; Yuter and Houze, 1995) are a way to view the statistical distribution of radar-derived parameters as a function of height. In Figs. 3.19, 3.20, and 3.21, CFADs of Z_H, Z_{DR}, and K_{DP} in each of the simulated and observed supercells are provided. Each CFAD is from the composited supercell over the 15-min window prior to tornadogenesis.

Below the freezing level, the observed supercell has a relatively even distribution of Z_H while the MORR and NSSL2 schemes produce values of Z_H >50 dBZ more frequently (Fig. 3.19a,b,c). The NSSL3 scheme produces a supercell with fewer instances of $Z_H > 50$ dBZ than are observed (Fig. 3.19a,d). However, the NSSL3 scheme better captures the distribution of Z_H at lower reflectivities (10–40 dBZ).

In the observed supercell, a large vertical gradient in radar reflectivity factor is not seen across the environmental freezing level, representing the non-instantaneous nature of freezing and melting of hydrometeors (Fig. 3.19a). Conversely, the transition from lower to higher values of Z_H across the freezing level in the simulated supercells acts more like a step function (Fig. 3.19b,c,d). The sharp offset from higher to lower Z_H is most prominent in the MORR and NSSL3 schemes (Fig. 3.19b,d). The NSSL2 scheme best reflects the observed supercell, as it produces a supercell with a more gradual transition from large regions of 50 dBZ below freezing to large areas with near 30 dBZ at 10 km AGL (Fig. 3.19a,c). All simulated supercells capture the high frequency of Z_H <10 dBZ above 15 km AGL, though only the MORR and NSSL2 schemes have the secondary peak in frequency at and below 15 km AGL (Fig. 3.19).

Investigating the vertical distribution of Z_{DR}, the NSSL3 scheme best represents observations at and below the freezing level (Fig. 3.20). While the NSSL2 and NSSL3 schemes have similar distributions of Z_{DR}, the NSSL3 scheme has a confined region of enhanced Z_{DR} (0–2 dB) below the freezing layer (Fig. 3.20d). The NSSL2 scheme also presents a region of enhanced Z_{DR}, but occurs at higher Z_{DR} values (2–4 dB)

compared to the NSSL3 scheme (Fig. 3.20c). Furthermore, both the NSSL schemes show a maximum frequency of Z_{DR} that increases beneath the melting layer, consistent with melting of hail and graupel. However, the transition from near 0 dB Z_{DR} above the freezing level to higher values near the surface in the NSSL schemes is still not as gradual as the observed storm (Fig. 3.20). This discrepancy is due to limitations in the melting processes in bulk microphysics schemes and the PFO.

Above the freezing level, each of the simulated supercells is nearly identical (Fig. 3.19b,c,d). The observed supercell has a broader distribution of Z_{DR} compared to the simulated supercells (Fig. 3.19). The more narrow distribution of Z_{DR} in the simulations is due to a number of factors, including but not limited to the assumption of spherical hydrometeors. In observations, it is possible for ice hydrometeors to have slightly negative or positive Z_{DR} when ice crystals are vertically aligned. Additionally, positive Z_{DR} is possible when large ice crystals are the dominant scatterer. Ice crystals are not included in the simulated supercells, resulting in a peak closer to 0 dB in Z_{DR} above the freezing level.

Of all the polarimetric variables, the simulated supercells do not represent the observed K_{DP} field well (Fig. 3.21). Below the freezing level, the MORR and NSSL2 schemes better represent the range of K_{DP} seen in observations, as the NSSL3 scheme has too narrow a range of K_{DP} (Fig. 3.21a,b,c). Above the freezing level, none of the simulated supercells capture the full range of K_{DP} seen in the observed storm (Fig. 3.21). Since K_{DP} is also 0 deg/km for spherical or tumbling hydrometeors, the assumption of spherical particles in the simulated supercells limits the possible range of K_{DP}. Additionally, none of the simulated supercells capture the immediate increase in K_{DP} beneath the freezing level (Fig. 3.21).

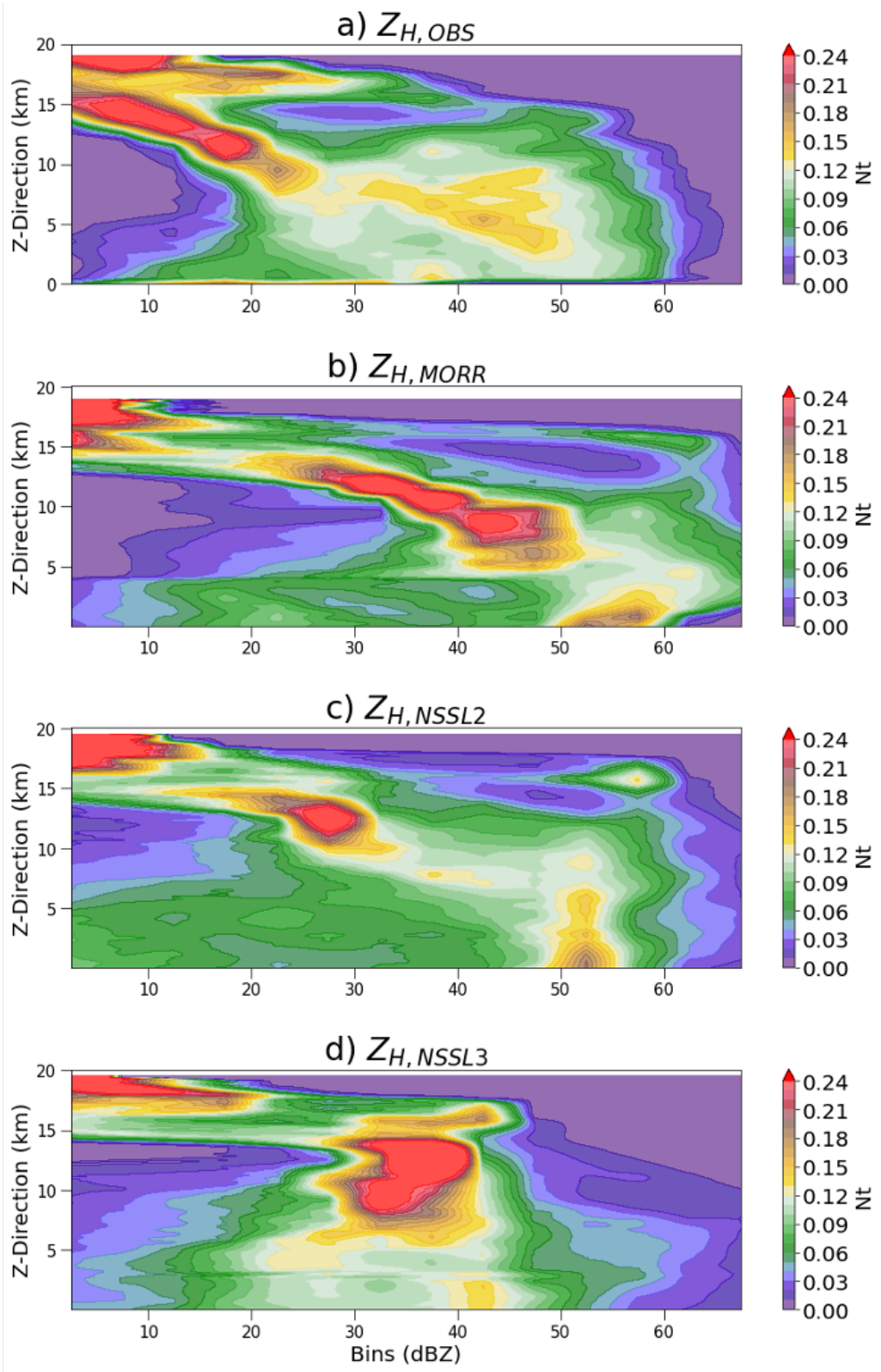


Figure 3.19: CFADS of Z_H for the (a) observed, (b) MORR, (c) NSSL2, and (d) NSSL3 datasets.

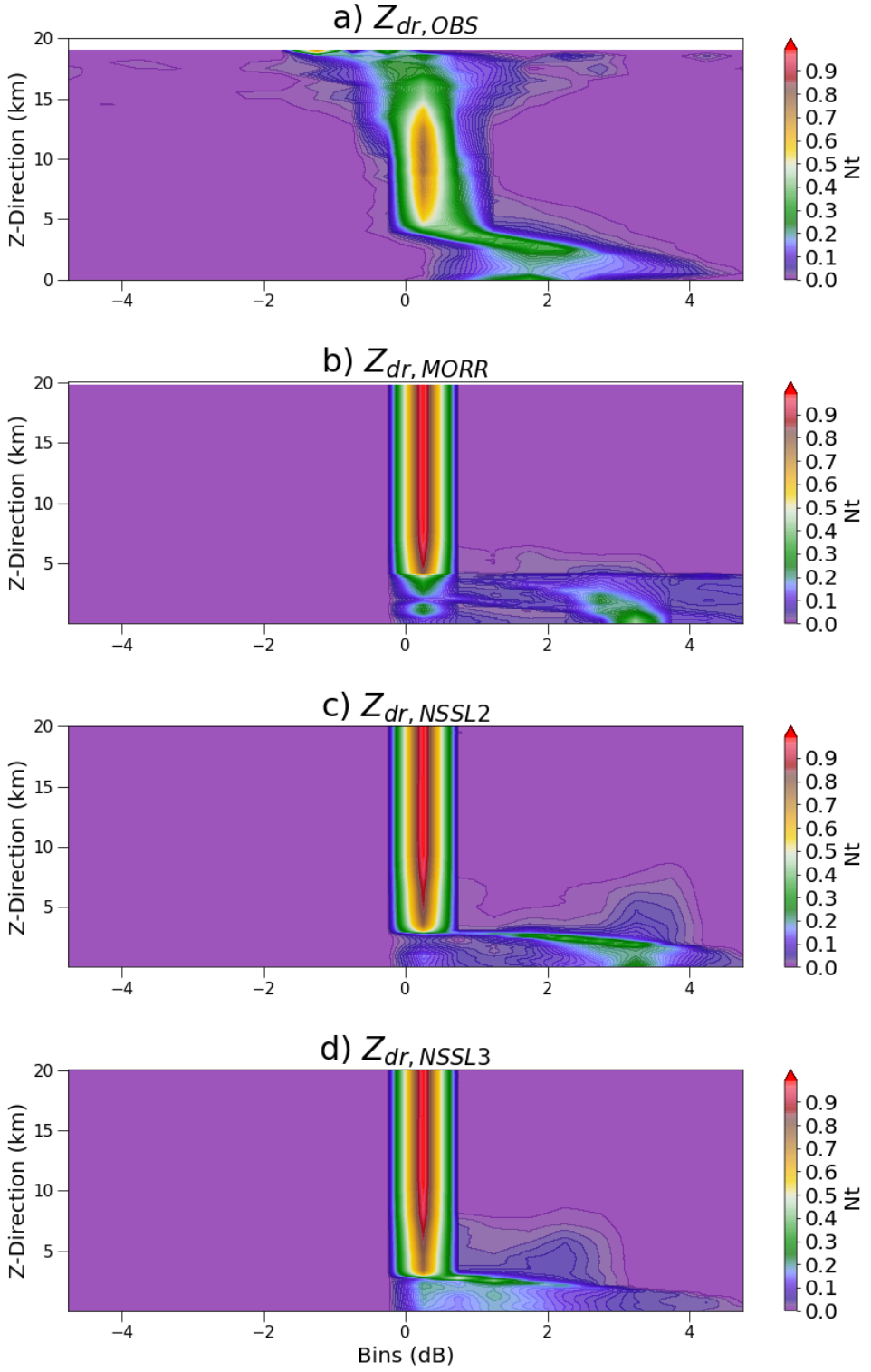


Figure 3.20: Same as in Fig. 3.19 but for Z_{DR}.

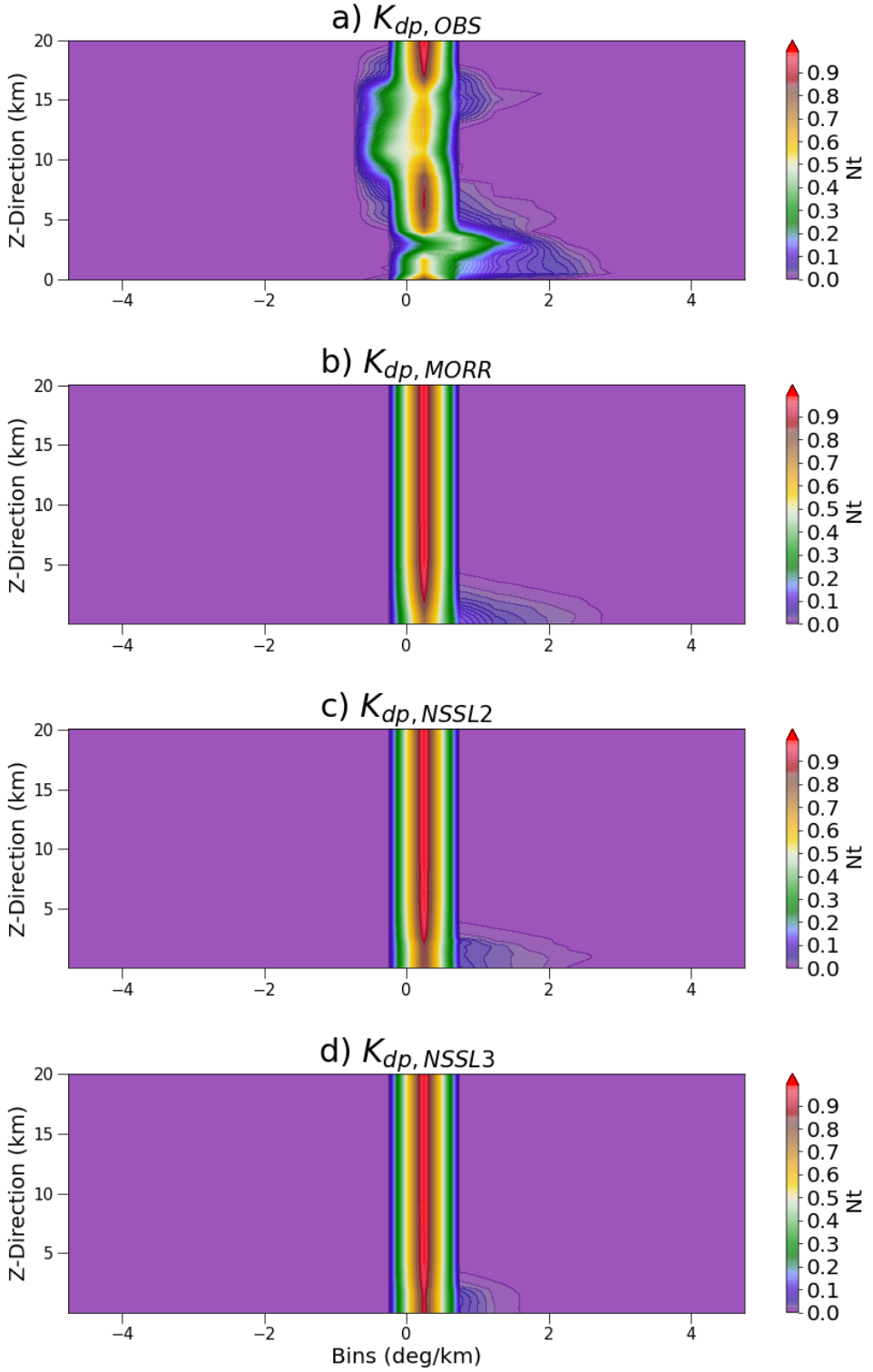


Figure 3.21: Same as in Fig. 3.19 but for K_{DP}.

3.4 Conclusions

Polarimetric forward operators serve as a bridge between cloud resolving model output and polarimetric radar variables. The majority of recent PFOs implement the T-matrix scattering approximation (Waterman, 1965) and an approximated melting model to calculate polarimetric radar observables (e.g., Jung et al., 2010; Ryzhkov et al., 2011; Dawson II et al., 2014; Matsui et al., 2019; Oue et al., 2020). The T-matrix approach can be computationally expensive at higher spatiotemporal resolutions and for operational applications such as the NOAA National Severe Storms Laboratory's Warn-On-Forecast System. To address this, Zhang et al. (2021) implemented parameterized equations that provide a more efficient method of using the T-matrix method. The resulting PFO in Zhang et al. (2021) has yet to be implemented in high-resolution (< 100 m) supercell simulations, so it remains unknown how the PFO handles polarimetric signatures at smaller spatial scales. Furthermore, when using the PFO, it is unknown what the ideal combination of melting model and microphysics scheme is for high-resolution simulations of supercell thunderstorms.

With these research gaps in mind, the goal of this study was to evaluate the performance of different melting models and microphysics schemes in producing polarimetric radar signatures comparable to observations. To achieve this, idealized CM1 simulations at 75 m horizontal and vertical resolutions were run using three microphysics schemes: Morrison 2-moment, NSSL 2-moment, and NSSL 3-moment. Furthermore, the Jung et al. (2008) (J08) and Liu et al. (2024b) (L24), and a novel Combined Melting Model (CMM) developed in this study, were compared. Simulations were run using the Orf et al. (2017) 24 May 2011 sounding, so that the model output could be compared with KOUN observations of a nearby tornadic supercell.

Results of the melting model comparison show that the new CMM creates the

most realistic distribution of ice hydrometeors throughout the supercell. The CMM limits the mass of dry ice below the freezing level and confines the mass of melting ice above the freezing level to the vicinity of the updraft. The L24 and J08 either accurately represent the distribution of melting or dry ice hydrometeors, not both. The J08 model produced the largest dry and melting ice sizes, whereas the CMM and L24 models limit the maximum size of ice hydrometeors. The CMM produced a distribution of D_m that primarily yielded $D_m < 10$ mm, while still allowing a few instances of larger ice hydrometeors. The L24 model behaves similarly to the CMM, and was the only model to constrain the D_m of melting graupel to smaller sizes. Finally, the L24 produced D_m, which decreases with decreasing Z_{DR} for melting graupel hydrometeors, while J08 produced D_m, which increases with decreasing Z_{DR} for dry graupel. The CMM combines the D_m and Z_{DR} relationships from L24 and J08, yielding a melting model that captures realistic relationships between D_m and Z_{DR} for both dry and melting ice hydrometeors. However, the L24 still produced better results for melting ice hydrometeors with a thin water torus. Finally, the CMM produced reasonable polarimetric signatures and removed the negative Z_{DR} artifact above the freezing level observed in the J08 model.

Supercell simulations with different microphysics schemes were compared using the CMM as the melting model. In the NSSL schemes, it was found that larger mixed-phase graupel falls from the north side of the updraft to the surface with little change in size. Conversely, the melting graupel in the MORR scheme decreases in size as it descends to the surface as the ice core melts and a liquid water torus envelops the core. It thus follows that, in the NSSL schemes, the melting of mixed-phase graupel below the freezing level occurs more slowly than in the MORR scheme. The largest mixed-phase ice also occurs in different locations across the NSSL and MORR schemes, with the largest melting ice occurring near the freezing level in the MORR scheme and

near the periphery of the bottom of the updraft in the NSSL schemes.

No single microphysics scheme best captured the polarimetric signatures in the observed supercell on 24 May 2011. Table 3.4 provides a summary of some of the metrics used to assess the performance of each microphysics scheme in reproducing polarimetric radar signatures. The MORR scheme best represented the height of the Z_{DR} column and Z_{DR} gradient at the top of the column, captured the size of the Z_{DR} column at 5.5 km AGL well, and best represented the range and distribution of K_{DP} values below the freezing level despite not capturing the size of the K_{DP} foot well. The NSSL2 scheme best represented the size of the supercell, had a distribution of rain and ice through the Z_{DR} column similar to that of Kumjian et al. (2014), and best reproduced the range and distribution of Z_H throughout the supercell compared to observations. Finally, the NSSL3 scheme best captured the size of the K_{DP} foot and Z_{DR} arc compared to observations, produced the most realistic-looking Z_{DR} arc, and produced the best distribution of Z_{DR} below the freezing level. In summary, *the NSSL3 scheme best captures polarimetric signatures below the freezing level while the MORR scheme best recreates signatures above the freezing level.* Which scheme should be selected for a given study depends heavily on the study's focus. From the results of this work, studies evaluating the low-level signatures in supercells should use the NSSL3 scheme, studies focusing on signatures above the freezing level should use the MORR scheme, while studies assessing the full supercell structure should likely use the NSSL2 or NSSL3 schemes.

Table 3.4: Comparison of microphysics scheme performance in representing the observed supercell and polarimetric signature area and depth.

	Least Representative of Observations		Most Representative of Observations
Storm Area	MORR	NSSL3	NSSL2
Z_{DR} Column Area	NSSL2	NSSL3	MORR
Z_{DR} Column Height	NSSL3	NSSL2	MORR
Z_{DR} Arc Area	NSSL2	MORR	NSSL3
K_{DP} Foot Area	NSSL2	MORR	NSSL3

Overall, due to the added predicted field (Z_x), the NSSL3 scheme better constrains the size sorting of hydrometeors. This is evident by the more realistic-looking shape of the Z_{DR} arc. However, each microphysics scheme produced high magnitudes of Z_H at low-levels compared to the observed supercells (Fig. 3.11). These regions of high Z_H are often dominated by melting hail and graupel (not shown). It has been shown that the size of hail in BMPs is largely governed by the number concentration (Wu et al., 2022). However, since the number concentration is the most difficult variable to observe, it contains large amounts of uncertainty. Future work should focus on finding improved ways to parameterize the number concentration in BMPs to mitigate the overestimation of maximum hail sizes.

Despite these current limitations of BMPs, the structure and location of polarimetric signatures can still be well captured by BMPs and the PFO. Thus, there is potential to use the PFO to study the evolution of polarimetric signatures in supercells. In such studies, the limitations of the selected melting model and microphysics scheme on the PFO output should be clearly outlined.

The results of this work help establish a framework for comparing a realistic (albeit idealized) supercell simulation to the observed storm using more quantitative methods (CFADs, comparison of signature areas, etc). Furthermore, this study highlights the

impact that microphysics schemes have on supercell structure. Given the numerous studies that have evaluated supercell dynamics in CM1 (e.g., Orf et al., 2017; Flournoy et al., 2020; Markowski, 2020; Coffer et al., 2023), future work should examine how these microphysics schemes affect both storm dynamics and the relationship between supercell dynamics and polarimetric radar signatures. Furthermore, given the computational expense of bin microphysics schemes, BMPs are still used in high-resolution ensemble studies of supercells and tornadoes (e.g., Orf et al., 2017; Markowski, 2020; Flournoy et al., 2020; Coffer et al., 2023). Thus, it is important to continually improve BMPs to better represent the microphysical processes that subsequently affect the dynamics and structure of observed convection.

Chapter 4

The Impact of Microphysics Schemes on the Dynamics, Thermodynamics, and Polarimetric Radar Signatures in Simulated Tornadic Supercells

4.1 Introduction

Numerous studies have used idealized numerical models to evaluate tornadic supercell dynamics and thermodynamics in different environments (e.g., Dahl, 2015; Coffer et al., 2017a; Orf et al., 2017; Yao et al., 2018; Flournoy et al., 2020; Vich and Romero, 2023; Fischer and Dahl, 2023), many of which have had a large impact on the trajectory of research within the severe weather community. For example, the results of numerical models have helped drive large field campaign efforts, such as the simulated streamwise vorticity current work in Orf et al. (2017) supporting one of the key research questions in the Targeted Observation by Radars and UAS of Supercells field campaign (Houston et al., 2026). Using numerical models to investigate tornadic supercells enables

detailed analysis of the relationships between storm dynamics, microphysics, and thermodynamics, which is challenging to comprehensively measure with observations alone. One aspect of modeling that must be accurately parameterized is the microphysics, as changes in the microphysics impact the modeled supercell through changes in enthalpy due to phase transitions. Studies have shown that these updraft and downdraft characteristics are important for tornadic supercells: the negative buoyancy of the storm outflow (Markowski et al., 2002; Grzych et al., 2007; Hirth et al., 2008; Snook and Xue, 2008; Markowski and Richardson, 2014), the strength of the updraft (Markowski and Richardson, 2014; Yokota et al., 2018), and the proximity of low-level rotation to the updraft (Markowski and Richardson, 2014). Since supercell thermodynamics and dynamics are interconnected, it follows that the changes in enthalpy from the simulated microphysics can alter the simulated cold pool, updraft, and vorticity field of the supercell.

The impact of model microphysics schemes on supercell cold pools has been documented in previous studies. In Dawson et al. (2010), it was shown that, due to the better representation of size sorting in multi-moment schemes, the triple- and double-moment schemes produced weaker and smaller cold pools that were consistent with observations from Markowski (2002). Furthermore, Morrison and Milbrandt (2011) showed that the strength of the cold pool was highly sensitive to the raindrop breakup parameterizations in the Morrison et al. (2009) 2-moment bulk scheme. However, this same sensitivity of the cold pool to the raindrop breakup parameterizations was not seen in the 2-moment bulk scheme from Milbrandt and Yau (2005a,b). In fact, the stronger cold pool seen in the Milbrandt and Yau (2005a,b) simulations for weaker drop breakup parameterizations was attributed to smaller mean hail sizes near the freezing level and more autoconversion from cloud water to rain water (Morrison and Milbrandt, 2011). Finally, it has been shown that cold pools are stronger in simula-

tions with higher fall speeds for rimed ice species due to the greater flux of rimed ice hydrometeors into the melting layer (Morrison and Milbrandt, 2011; Van Weverberg et al., 2012; Van Weverberg, 2013).

As described in Snook and Xue (2008), the impacts of the microphysics schemes on the cold pool influence tornadogenesis by altering the vertical alignment between low- and mid-level vorticity. It has also been shown that increasing the moment of bulk schemes affects the simulated tornado. In Dawson et al. (2015b), variations of a single-, double-, and triple-moment microphysics scheme were used for the numerical prediction of the 3 May 1999 Oklahoma tornado. The numerical data were compared with surface observations to verify the model output. It was found that the triple-moment scheme best predicted the tornado track, had less evaporation of rain and subsequent weaker downdrafts compared to the single-moment schemes, and produced longer-lived and stronger tornado-like vortices (Dawson et al., 2015b). In addition, the inclusion of ice in the microphysics parameterization increases updraft speeds due to the positive buoyancy created by the release of latent heat from fusion (Johnson and Straka, 1993; Gilmore and Rasmussen, 2004a). Aside from Dawson et al. (2015b), few studies have directly evaluated the impact of BMPs on tornado and updraft characteristics in simulated supercells.

It is clear from previous work that bulk microphysics schemes (BMPs) have a large impact on supercell thermodynamics and dynamics. According to Ryzhkov et al. (2020), polarimetric radar data can serve as a source of needed information for improving cloud models, as polarimetric data can distinguish between different hydrometeor types and thus identify "polarimetric fingerprints" caused by microphysical processes. Some studies have examined how BMPs affect these "polarimetric fingerprints" at select time steps (e.g., Johnson et al., 2016; Liu et al., 2024b); however, these studies have not evaluated the impact of BMPs on both polarimetric radar signatures and

supercell dynamics relative to observations. From observational studies, an important relationship between polarimetric signatures and supercell updrafts is the documented correlation between the Z_{DR} column height and width with updraft size and strength (often evaluated in observations by tornado intensity or mesocyclone width) (Van Den Broeke, 2017; Snyder et al., 2017; French and Kingfield, 2021). Previous work has examined the relationships between polarimetric radar signatures and storm dynamics in a simulated quasi-linear convective system for a single BMP (e.g., Healey and Broeke, 2025), but the impact of BMPs on these relationships remains relatively unknown for tornadic supercells.

This study seeks to evaluate how different BMPs impact the following in tornadic supercells:

1. tornado intensity and longevity,
2. updraft and cold pool structure and intensity, and
3. the relationships between polarimetric signatures and supercell dynamics.

The polarimetric signatures that will be evaluated are the Z_{DR} column, the K_{DP} foot, the Z_{DR} arc, and the Z_{DR} arc-K_{DP} foot separation vector. Each of these signatures has been shown through radar observations to exhibit distinct patterns before tornadogenesis. The Z_{DR} column width should increase for more intense updrafts (French and Kingfield, 2021), and the Z_{DR} arc-K_{DP} foot separation vector should be 90°to the right of storm motion in a pre-tornadic supercell. Given K_{DP} scales with liquid water content and subsequent negative buoyancy (Carlin and Ryzhkov, 2019), it is expected that the magnitude and location of the K_{DP} foot should scale with the intensity and location of the cold pool.

This study uses Cloud Model 1 (Bryan and Fritsch 2002; CM1) to simulate high-resolution ensembles of tornadic supercells. To obtain the polarimetric radar data, a

modified version of the polarimetric forward operator (PFO) from Zhang et al. (2021) is used. By combining the dynamic and thermodynamic outputs from CM1 with the polarimetric variables from the PFO, this study can uniquely assess the performance of each BMP in simulating the observed relationships among supercell dynamics, thermodynamics, and polarimetric radar signatures. Furthermore, this study uses ensembles of simulated supercells, which better represent supercell outcomes than a single simulation. Each ensemble is run with a different BMP, and each ensemble member is created by varying microphysical parameters to capture variability within each BMP. The configuration of CM1, the forward operator used to retrieve the polarimetric signatures, and other methodologies are described in Section 4.2. Section 4.3 presents the simulation results, while Section 4.4 summarizes the work herein.

4.2 Methodology

The impacts of model microphysics schemes on tornadic supercell dynamics, thermodynamics, and polarimetric signatures are assessed through simulations performed using three microphysics schemes in CM1: the Morrison 2-moment (MORR; Morrison et al. 2005), NSSL 2-moment (NSSL2; Mansell et al. 2010), and NSSL 3-moment (NSSL3; Mansell et al. 2020) schemes. To create an ensemble for each microphysics scheme, the drop breakup parameter for the MORR scheme and the cloud condensation nuclei (CCN) concentration for the NSSL schemes were varied (see Table 4.1 for the range of values). While the changes in the drop breakup and CCN parameters do not provide a one-to-one comparison between the MORR and NSSL schemes, the two parameters are related: a larger drop breakup parameter leads to a higher number of smaller drops, and a higher CCN concentration in the NSSL schemes yields a similar outcome. Changing the drop breakup and CCN parameters resulted in 43 simulations: 17 for the

MORR scheme, 13 for the NSSL2 scheme, and 13 for the NSSL3 scheme. Aside from changes to the drop breakup and CCN parameters, each simulation was run with the same configuration (Table 4.1). Each ensemble member has a spatial resolution of 75 m x 75 m x 75 m, and the output was saved every 1 min. The environmental sounding from the inflow of the El Reno EF5 tornado on 24 May 2011 was used to initialize the simulation's base state (Orf et al., 2017).

Table 4.1: Configuration of CM1 used for each simulation.

CM1 Model Configuration
Isotropic grid spacing, no stretch (75 m)
Domain: 120x120x20 km
TKE turbulence closure
5th order WENO advection
Zero surface strain surface boundary conditions (free slip)
El Reno 24 May 2011 sounding (Orf et al., 2017)
Microphysics schemes: Morrison 2-moment ($300e^{-6}$ – 800^{-6} db), NSSL 2-moment ($0.40e^{9}$–$1.00e^{9}$ CCN), NSSL 3-moment ($0.40e^{9}$–$1.00e^{9}$CCN)

The Okubo–Weiss (OW) parameter (Okubo, 1970; Weiss, 1991) was used to identify the presence of a coherent vortex. The equation for the OW parameter is given in Equation 4.1, where S_n^2 is the stretching deformation, S_s^2 is the shearing deformation, and ζ is the vertical vorticity. Positive values of the OW parameter indicate that rotation dominates over the deformation of the flow. It was discussed in Zovko-Rajak et al. (2023) that averaging the OW parameter over a vertical layer was a good way to identify a coherent vortex. With this in mind, the OW parameter was calculated and then averaged over the 0-4 km layer. If the layer-averaged OW parameter was greater than 0.1 s^{-1}, a coherent vortex was considered present. The first time a coherent vortex was present was documented as the time of tornadogenesis.

An adaptation of the tornadogenesis criteria from Flournoy et al. (2020) was also

tested. In Flournoy et al. (2020), tornadogenesis was defined as the first time the 10-m AGL vertical vorticity is > 0.3 s^{-1}, the 0-1 km AGL pressure perturbations $<$ -10 hPa, and the 10-m AGL wind speeds > 35 m s^{-1}. Since the pressure field was unavailable at the time of this analysis, the 10-hPa criteria were replaced with the co-location of the 99^{th} percentile horizontal and vertical wind magnitude. Assuming an incompressible, hydrostatic flow, a region with surface convergence and an updraft will have mass evacuation and a local minimum in pressure. Using the adapted Flournoy et al. (2020) tornadogenesis criteria, the time of tornadogenesis was often 1-2 min later than the OW parameter method (not shown). In some ensemble members, the time of tornadogenesis varied beyond the 1-2 min difference. For example, the difference in time for the MORR ensemble ranged from 1 – 18-min, the NSSL2 ensemble ranged from 0 – 51-min, and the NSSL3 ensemble ranged from 1 – 47-min. The OW parameter method was chosen because, without the pressure field, the Flournoy et al. (2020) method was unable to be accurately replicated. However, for future iterations of this work, the sensitivity of the results to different thresholds of the OW parameter should be tested. Furthermore, given the 75 m horizontal resolution of these simulations, we are unable to fully resolve the tornado vortex. However, we can still capture increases in rotation and obtain a general time window of tornado formation.

$$OW = \zeta^2 - (S_n^2 + S_s^2) \tag{4.1}$$

To simulate polarimetric radar data, the forward operator from Zhang et al. (2021) was coupled with a melting model adapted from Jung et al. (2008) and Liu et al. (2024b). Details of the melting model – hereafter referred to as the Combined Melting Model (CMM) – are described in Section 4.2.2.3. The adaptation of the forward operator to a 3-moment BMP is described in Section 4.2.3.

4.2.1 Polarimetric Signature Identification

An automated algorithm was employed to identify the polarimetric signatures evaluated in this study. Due to the splitting nature of the simulated supercell, a spatial threshold of $y < 20$ km was applied to the algorithm to remove data from the left split of the supercell. The Z_{DR} column was defined to be any bin with $Z_{DR} > 1$ dB at 5.5 km AGL (1 km AFL) (French and Kingfield, 2021); the Z_{DR} arc was defined to be any bin with $Z_{DR} > 3$ dB at 1 km AGL, which is between the 2 dB and 3.5 dB thresholds used in Van Den Broeke (2017); and the K_{DP} foot was defined to be any bin with $K_{DP} > 3$ deg/km at 1 km AGL. The area of these signatures was calculated by summing the areas of each bin flagged by the algorithm as part of the signature. A ρ_{hv} threshold of 0.93 was used in the identification of each signature to help remove non-meteorological scatterers as done in Loeffler and Kumjian (2018).

For the calculation of the Z_{DR} arc- K_{DP} separation vector, the adaptive threshold methodology from Loeffler and Kumjian (2018) was followed. A ρ_{hv} threshold of 0.93 was also used in this portion of the analysis to identify the Z_{DR} arc and K_{DP} foot in addition to the Z_{DR} and K_{DP} thresholds previously mentioned to keep consistent with the Loeffler and Kumjian (2018) methodology. The storm motion vector used in the calculation of the Z_{DR} arc- K_{DP} separation vector was obtained from the Orf et al. (2017) sounding.

4.3 Results

4.3.1 Tornado Characteristics

The time of tornadogenesis was defined as the first time that the vertically averaged OW parameter (Equation 4.1) is greater than 0.1 s^{-1}. The tornadogenesis times for

each ensemble are shown in Fig. 4.1. On average, the MORR ensemble produced tornadoes 5.9 min earlier than the NSSL2 ensemble and 10.5 min earlier than the NSSL3 ensemble. However, aside from the outlier at approximately 6000 s in the MORR ensemble, the range of genesis times is smaller for the MORR ensemble compared to the NSSL ensembles. Across all ensembles, the majority of the tornado-like vortices formed between 4000 – 6000 s.

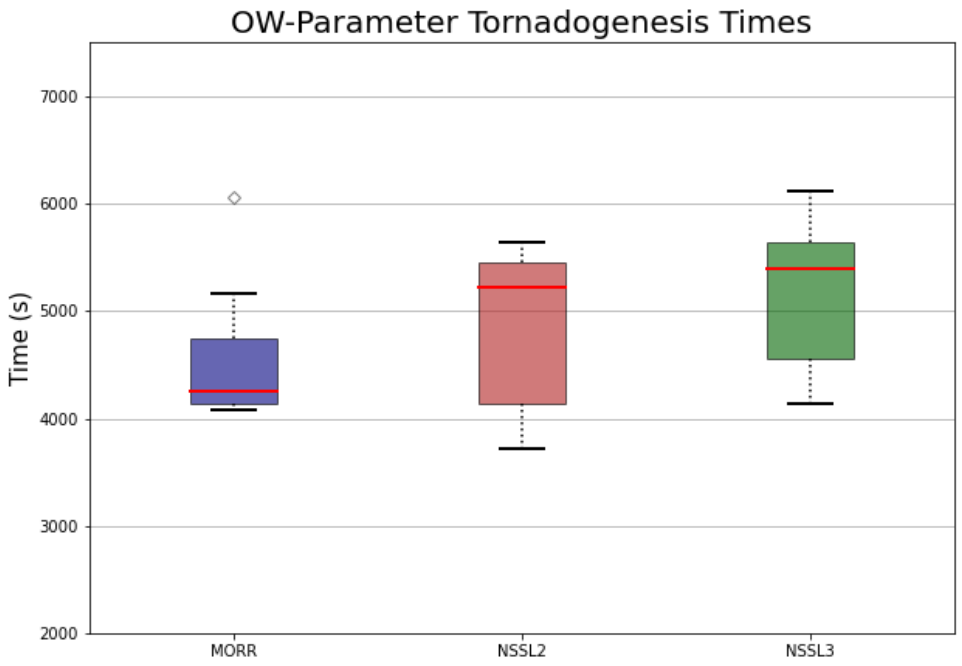


Figure 4.1: Time of tornadogenesis as defined by the OW parameter for each ensemble.

The longevity of the peak intensity of the tornado also varied across the three ensembles (Fig. 4.2a). To evaluate this, the fraction of time the horizontal surface winds exceeded 90 m s^{-1} (EF5 intensity) during the tornado was calculated. The surface winds were taken from the lowest vertical level output from the model, which is 0.04 km AGL. Again, on average, the NSSL ensembles produced vortices that persisted at

EF5 intensity for longer than the vortices produced by the MORR ensemble (Fig. 4.2a). However, when looking at the maximum horizontal surface winds ($V_{h,max}$), the MORR ensemble tended to produce higher peak winds both at tornadogenesis and during the tornado compared to the NSSL schemes (Fig. 4.2b, c). This means that, while the time of peak intensity was shorter for the MORR tornadoes, the tornadoes produced by the MORR ensemble were, on average, stronger than those produced by the NSSL ensembles.

It should be noted that the range of $V_{h,max}$ at tornadogenesis for the NSSL3 ensemble was relatively small, especially compared to the large range of $V_{h,max}$ in the NSSL2 ensemble (Fig. 4.2b). Also, a small number (3) of the tornadoes produced by the NSSL ensembles never reached EF5 intensity while all of the MORR tornadoes reached EF5 intensity at some point in the tornado's lifecycle (Fig. 4.2a).

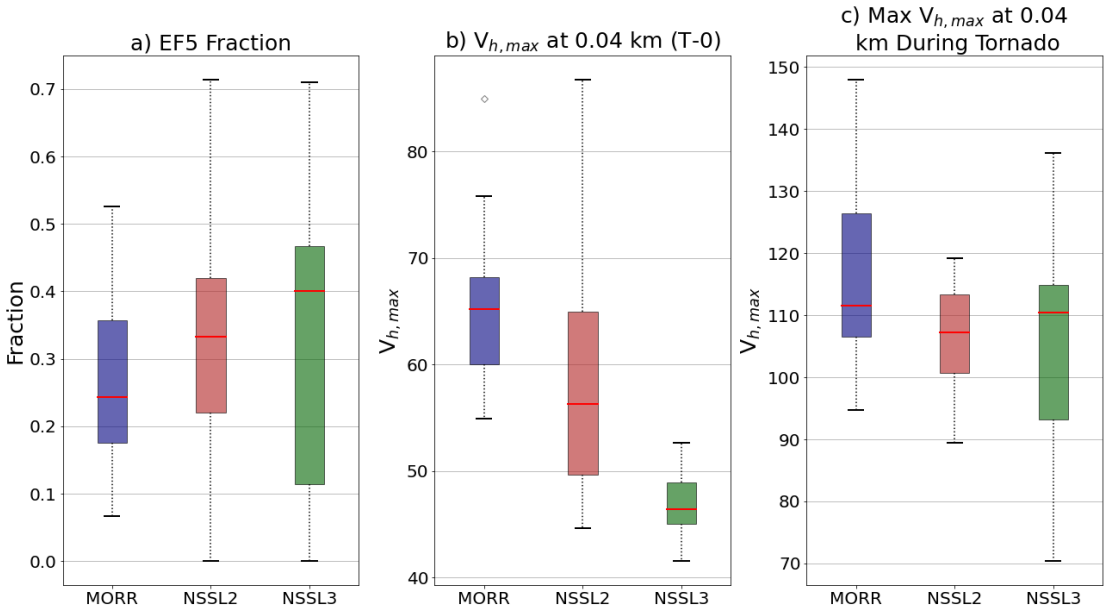


Figure 4.2: Box plots of a) the fraction of time a supercell had an EF5 tornado, b) $V_{h,max}$ at 0.04 km, and c) maximum $V_{h,max}$ during the tornado for the MORR (blue), NSSl2 (red), and NSSL3 (green) microphysics schemes. Black lines represent the range of the data; red horizontal lines show the location of the median; and the color-filled boxes range from the 25th to 75th percentile.

The impact of changing the drop breakup parameter in the MORR ensemble and the CCN concentration in the NSSL ensembles on the tornadogenesis time and $V_{h,max}$ was assessed. In the MORR and NSSl2 ensembles, the fluctuations in tornadogenesis time and $V_{h,max}$ across an increasing drop breakup parameter were seemingly random with no discernible correlation (Fig. 4.3a,b,d,e). In the NSSL3 ensemble, the time of tornadogenesis generally increased and $V_{h,max}$ decreased with increasing CCN concentration (Fig. 4.3c,f). It is unclear why the 3-moment scheme had a quasi-linear trend across these parameters, but it is possible that the wind speeds in the NSSL3 scheme are more sensitive to the selected CCN concentration.

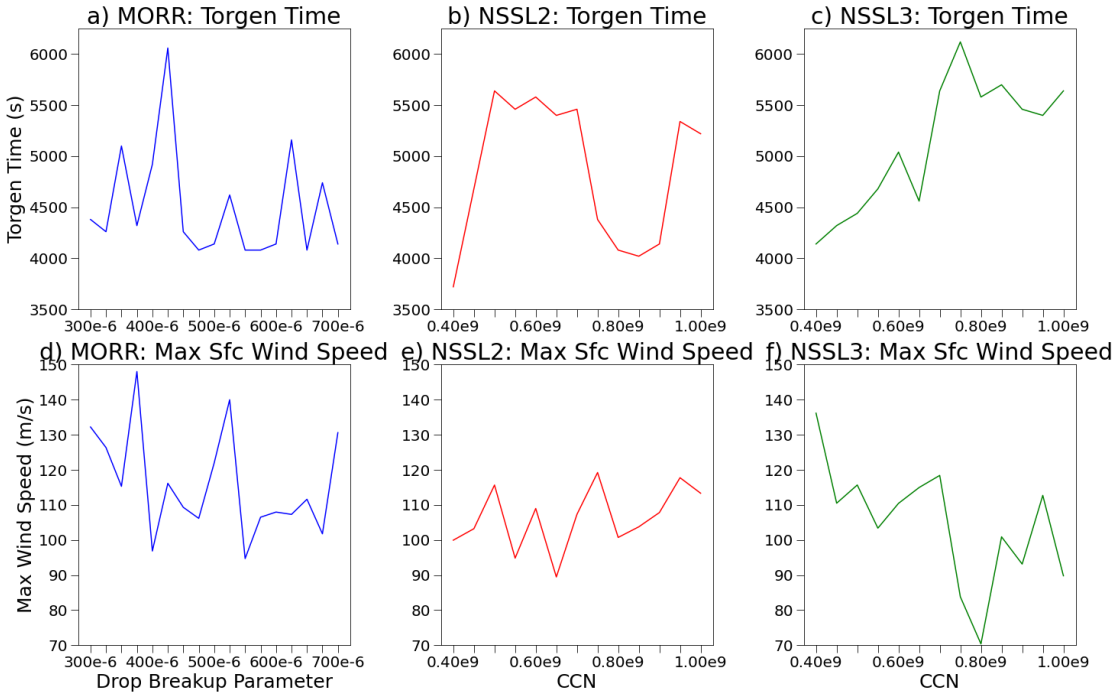


Figure 4.3: Plots of the time of tornadogenesis (a–c) and $V_{h,max}$ at 0.04 km AGL (d–f) for the MORR (a,e), NSSL2 (b,e), and NSSL3 (c,f) microphysics schemes.

In addition to $V_{h,max}$, the ensemble average maximum vertical vorticity ($\bar{\zeta}_{max}$) was evaluated over the 30 min period leading up to tornadogenesis (Fig. 4.4). Despite the 75 m horizontal resolution of these simulations, $\bar{\zeta}_{max}$ still provides information

about increases (decreases) in rotation that can then be used to make inferences about tornado intensification (weakening).

From Fig. 4.4a showing the MORR ensemble, it is clear that increases in $\bar{\zeta}_{max}$ begin between T-15 and T-20 near the surface. The intensifying rotation between T-15 and T-10 spans the lowest 0.5 km before deepening to the lowest 1 km layer between T-10 and T-5. It is within the last 5 min prior to tornadogenesis in the MORR ensemble that $\bar{\zeta}_{max}$ at the surface intensifies to 0.5 s^{-1} and extends the full lowest 3 km layer (Fig. 4.4a).

The evolution of $\bar{\zeta}_{max}$ in the NSSL2 ensemble begins with a "pulse" of higher $\bar{\zeta}_{max}$ values at T-15 (Fig. 4.4b). This "pulse" spans approximately 3 min with $\bar{\zeta}_{max} > 0.25$ s^{-1} in the lowest 1.5 km. Values of $\bar{\zeta}_{max}$ then weaken, followed by another "pulse" at T-10 (Fig. 4.4b). The second "pulse" of $\bar{\zeta}_{max}$ extends deeper through the lowest 3 km compared to the first "pulse." These "pulses" are seen in 8 out of the 12 ensemble members in the NSSL2 ensemble. After the second intensification of $\bar{\zeta}_{max}$ at T-10, values of $\bar{\zeta}_{max} > 0.25$ s^{-1} gradually begin to extend through the 3 km layer (Fig. 4.4b). Within the final 1-3 min prior to tornadogenesis, values of $\bar{\zeta}_{max}$ increase to near 0.5 s^{-1} at the surface before forming a cohesive column of intense $\bar{\zeta}_{max}$ up to 2 km AGL (Fig. 4.4b).

In the NSSL3 ensemble, the values of $\bar{\zeta}_{max}$ throughout the lowest 3 km are generally lower than what was seen in the MORR and NSSL2 ensembles (Fig. 4.4). Between T-15 and T-10, there is a slight increase of $\bar{\zeta}_{max}$ through the 3 km layer (Fig. 4.4c). There is a brief decrease in $\bar{\zeta}_{max}$ before values begin to continuously increase through the 3 km layer from T-10 to T (Fig. 4.4c).

While the MORR and NSSL2 ensembles displayed vertical vorticity that gradually increased from the surface up to 3 km AGL, the NSSL3 ensemble showed an instantaneous intensification throughout the layer (Fig. 4.4). In Houser et al. (2015), Doppler

velocity observations from the rapid scanning, X-band, polarimetric, Doppler radar (RaXPol) were used to assess the development of rotation in the El Reno EF5 on 24 May 2011. The observed maximum rotational velocity was shown to increase simultaneously through a column above the pre-existing low-level rotation (see Houser et al. (2015), their Fig. 12). When comparing the results of Houser et al. (2015) to our simulations of the El Reno tornado, the NSSL3 moment ensemble seemingly best captures the simultaneous intensification of rotation through the low-levels (Fig. 4.4c).

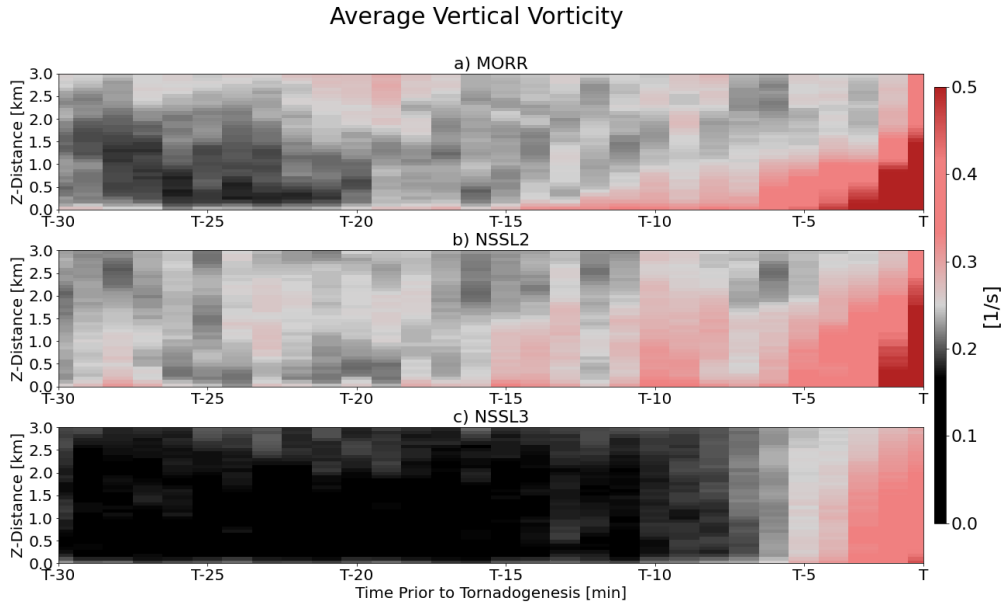


Figure 4.4: Time-height plot of ζ_{max} for the a) MORR, b) NSSL2, and c) NSSL3 microphysics schemes. Values of ζ_{max} are averaged across ensemble members.

4.3.2 Updraft Characteristics

In this study, both the low-level (1 km AGL) and mid-level (5.5 km AGL) updraft characteristics are assessed. The height of 5.5 km AGL was chosen as it is 1 km above the freezing level and allows for the comparison of the updraft and Z_{DR} column

characteristics (Section 4.3.4). Two different velocity thresholds were used to define the updraft: 5 m s^{-1}, which captures the broad updraft area, and 20 m s^{-1}, which is used to define the updraft core.

When investigating the updraft area defined by the 5 m s^{-1} threshold at 1 km AGL, the NSSL ensembles generally have larger updraft areas (between 61 km^2 and 62 km^2) compared to the MORR ensemble (48 km^2) (Fig. 4.5a). The same holds true at the same height but with the 20 m s^{-1} velocity threshold, with the NSSL schemes having an average area of 6 km^2 and the MORR scheme having an average area of 4 km^2 (Fig. 4.5b). At 5.5 km AGL, the NSSL ensembles once again produce wider updrafts at both velocity thresholds compared to the MORR ensemble (Fig. 4.5c,d). The range of updraft areas for the NSSL ensembles is larger at 5.5 km AGL than at 1 km AGL, producing more overlap in updraft areas across the three ensembles (Fig. 4.5). Overall, the NSSL2 ensemble produces the largest updraft areas at 5.5 km with a 5 m s^{-1} threshold (87 km^2 for NSSL2 and 94 km^2 for NSSL3) while the MORR ensemble produces the smallest at each height and updraft threshold (Fig. 4.5).

The differences in updraft area are somewhat contrary to what was shown in Sessa and Trapp (2020), who showed there is a linear relationship between stronger tornadoes and wider, low-level mesocyclones (which was used as a proxy for updraft width). Given the MORR ensemble produced, on average, stronger tornadoes (Fig. 4.2c), it was expected that the MORR ensemble would produce wider updrafts than what was produced by the NSSL ensembles. However, Sessa and Trapp (2020) assessed tornado intensity through the EF scale rather than $V_{h,max}$, which could explain the difference in results.

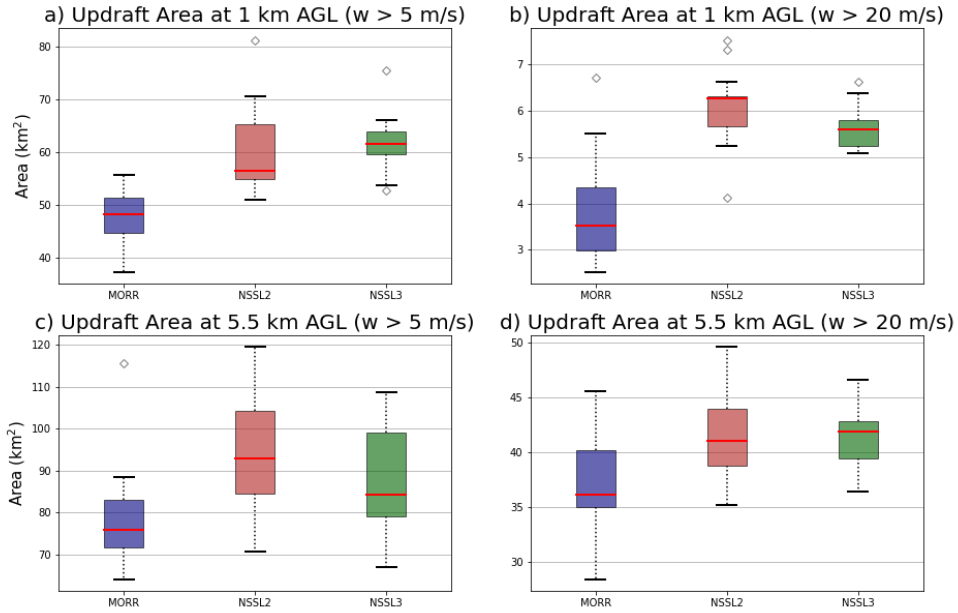


Figure 4.5: Box plots of the updraft area at T-0 at 1 km AGL (a–b) and 5.5 km AGL (c–d) for the MORR (blue), NSSL2 (red), and NSSL3 (green) microphysics schemes. Black lines represent the range of the data; red horizontal lines show the location of the median; and the color-filled boxes range from the 25$^{\text{th}}$ to 75$^{\text{th}}$ percentile.

The time evolution of the maximum vertical velocity (W_{max}) at 1 km AGL was evaluated across the 30-min period prior to tornadogenesis (Fig. 4.6). For all ensembles, values of the 50^{th} percentile W_{max} between T-30 and T-15 are between 20 m s^{-1} and 40 m s^{-1} (Fig. 4.6). It is within the last 15 min period leading up to tornadogenesis where the ensembles diverge from one another. The MORR ensemble exhibits the largest increase in W_{max} from T-15 to T, intensifying by approximately 40 m s^{-1} over 15 min (Fig. 4.6a). The NSSL2 and NSSL3 ensembles exhibit a less drastic increase in W_{max}, intensifying by approximately 10 m s^{-1} during this period (Fig. 4.6b,c). The NSSL3 ensemble also shows the smallest spread in W_{max} across the ensemble (Fig. 4.6c).

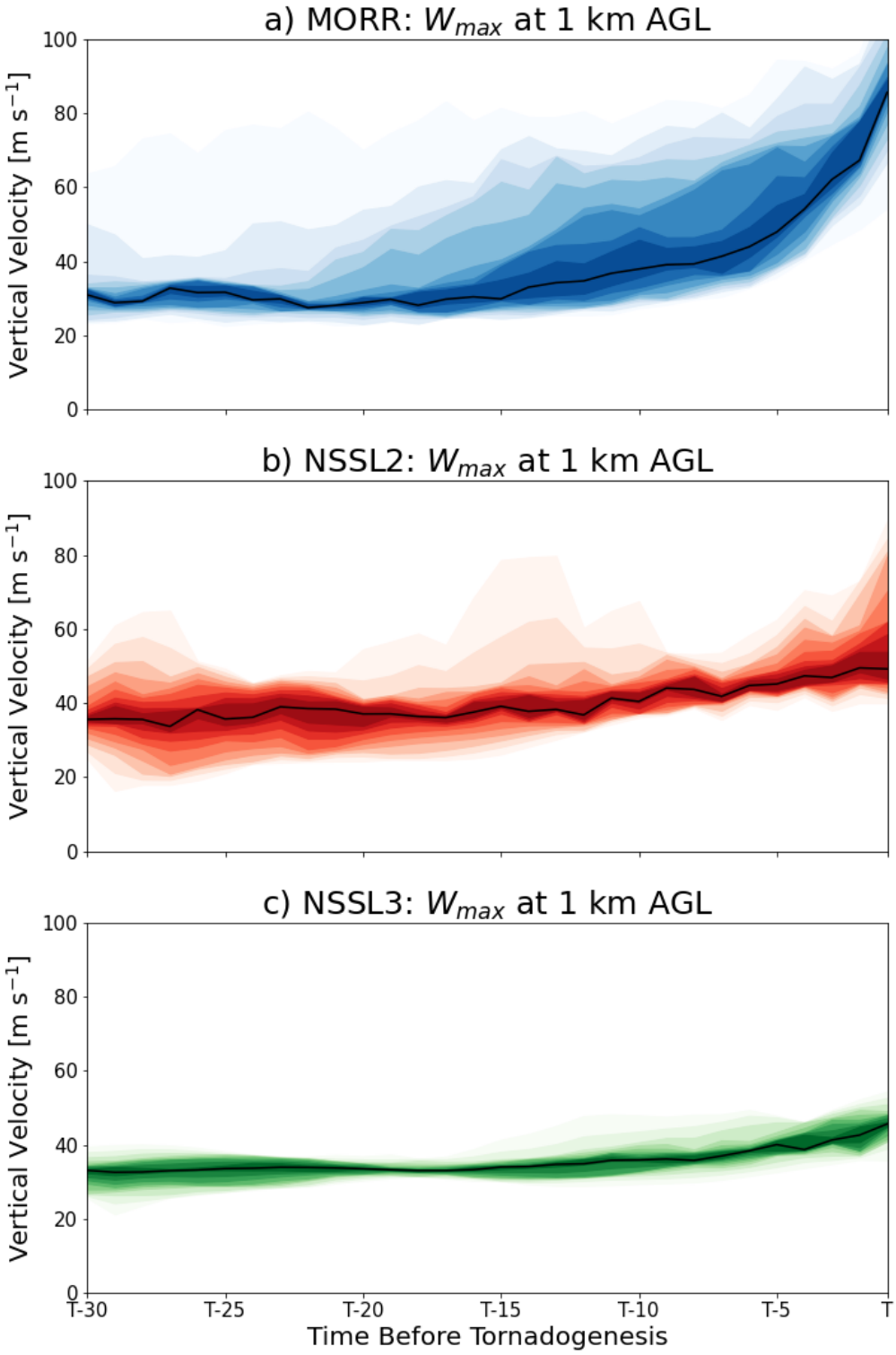


Figure 4.6: Time series of w_max at 1 km AGL for the a) MORR, b) NSSL2, and c) NSSL3 ensembles. Black lines represent the 50$^{\text{th}}$ percentile while the colorfill ranges from the 0$^{\text{th}}$ to the 100$^{\text{th}}$ percentile.

In addition to the intensity and area of the updraft, the structure of the updraft was also evaluated. The updraft core ($w > 20$ m s^{-1}) at 1 km AGL is collocated with the region of maximum surface convergence for each ensemble, indicating that the low-level wind field plays a direct role in the location and size of the 1 km updraft (Fig. 4.7). The structure of the average $w = 20$ m s^{-1} updraft at 1 km AGL for the MORR ensemble exhibits a small tail extending from the eastern portion of the updraft toward the southwest, consistent with a rear-flank gust front (Fig. 4.7a). Meanwhile, the structure of the 1 km AGL updraft for the NSSL ensembles is quite similar (Fig. 4.7b,c). The average 5.5 km AGL updraft across each ensemble was quite similar, with the NSSL ensembles producing a small tail at the southern end of the updraft (Fig. 4.7).

The 5.5 km AGL updraft is much broader than the region of surface convergence, meaning that processes other than the surface convergence drive the size of the updraft core above the freezing level (Fig. 4.7). In fact, Fig. 4.8 shows that the 5.5 km AGL updraft in each ensemble is largely governed by the region of maximum θ'_ρ. The region of $\theta'_\rho > 8$ K is almost twice as large in the NSSL2 and NSSL3 ensembles (16.9 km^2 and 17.0 km^2) than the MORR ensemble (8.9 km^2), with the NSSL3 ensemble producing the warmest maximum average temperatures (12.5 K) and the MORR ensemble producing the coldest maximum average temperature (10.2 K) (Fig. 4.8).

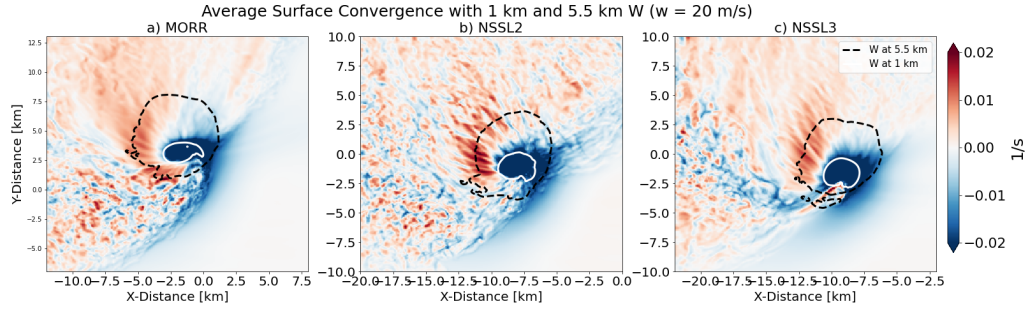


Figure 4.7: Horizontal cross-section of surface (0.04 km AGL) convergence with the 1 km (white solid) and 5.5 km (black dashed) updraft contours at w = 20 m s^{-1} for the a) MORR, b) NSSL2, and c) NSSL3 ensembles. Values of convergence and W are averaged across ensemble members at T-0.

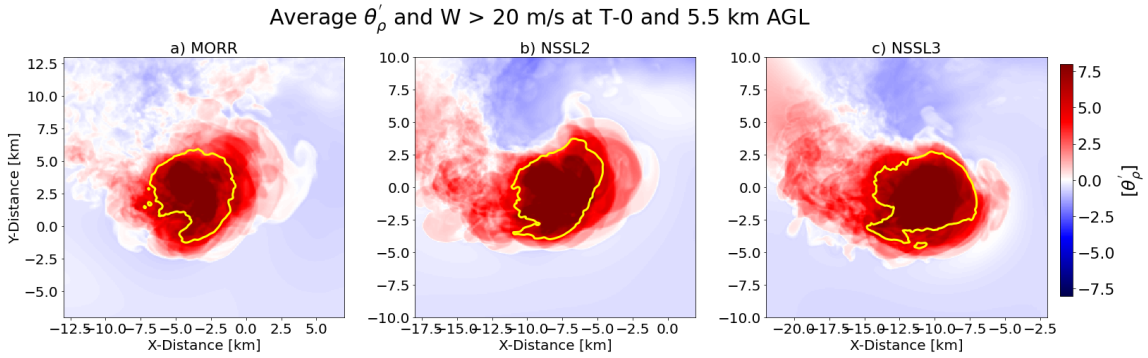


Figure 4.8: Horizontal cross-section of θ_p' and W at 5.5 km AGL and at T-0 for the a) MORR, b) NSSL2, and c) NSSL3 ensembles. Values of convergence and W are averaged across ensemble members. Yellow contour represents W = 20 m s^{-1}.

The updraft at 5.5 km AGL was examined in more detail in Fig. 4.9. To create Fig. 4.9, the regions of $w > 20$ m s^{-1} and $Z_{DR} > 1$ dB were identified for each ensemble member. The flagged bins were then summed across the ensemble members, resulting in a count of the location of $w > 20$ m s^{-1} across the full ensemble. Note that Fig. 4.9 does not provide information about the magnitude of w, only the spatial distribution of $w > 20$ m s^{-1}.

From T-30 to T-0, the $w > 20$ m s^{-1} updraft in the MORR ensemble becomes more

spatially coherent in the center of the updraft (Fig. 4.9a,d,g) and Z_{DR} values increase within the Z_{DR} column. There is more variability in the structure of the updraft away from the core region. Across the MORR ensemble in the eastern extent of the updraft at each time step shown in Fig. 4.9, the eastern region has greater variability. Also, a tail extending from the western edge of the updraft appears at T-15 in approximately 20% of the MORR ensemble (Fig. 4.9d).

In the NSSL2 ensemble, the updraft is generally more circular compared to the MORR ensemble at T-30 and T-15 (Fig. 4.9b,e). There is also a larger region of agreement within the updraft center at T-15 in the NSSL2 ensemble compared to the MORR ensemble (Fig. 4.9d,e). The updraft tail in the NSSL2 ensemble appears at T-0 and is generally more prominent across the ensemble members at this time compared to the MORR ensemble (Fig. 4.9g,h). While it is not shown, the updraft tail in the NSSL2 ensemble is generally collocated with the rear flank gust front at the surface and a region of warmer θ'_{ρ} at 5.5 km AGL.

The NSSL3 ensemble exhibits the highest level of agreement across the ensemble at T-30 compared to the other ensembles (Fig. 4.9c). The structure of the updraft at T-30 was generally circular with some ensembles producing regions of $w > 20$ m s^{-1} to the west and northeast of the updraft core (Fig. 4.9c). At T-15, the updraft in the NSSL3 ensemble resembles that in the NSSL2 ensemble, but with a smaller area of spatial coherence within the updraft core (Fig. 4.9e,f). Like in the NSSL2 ensemble, the updraft tail appears at T-30 in the NSSL3 ensemble (Fig. 4.9i). In the NSSL3 ensemble, the updraft tail is collocated with the leading edge of the rear flank downdraft as seen in the NSSL2 ensemble (not shown). Generally, the updraft in the NSSL ensembles takes on a comma-like shape at tornadogenesis, while the updraft in the MORR ensemble remains quasi-circular (Fig. 4.9).

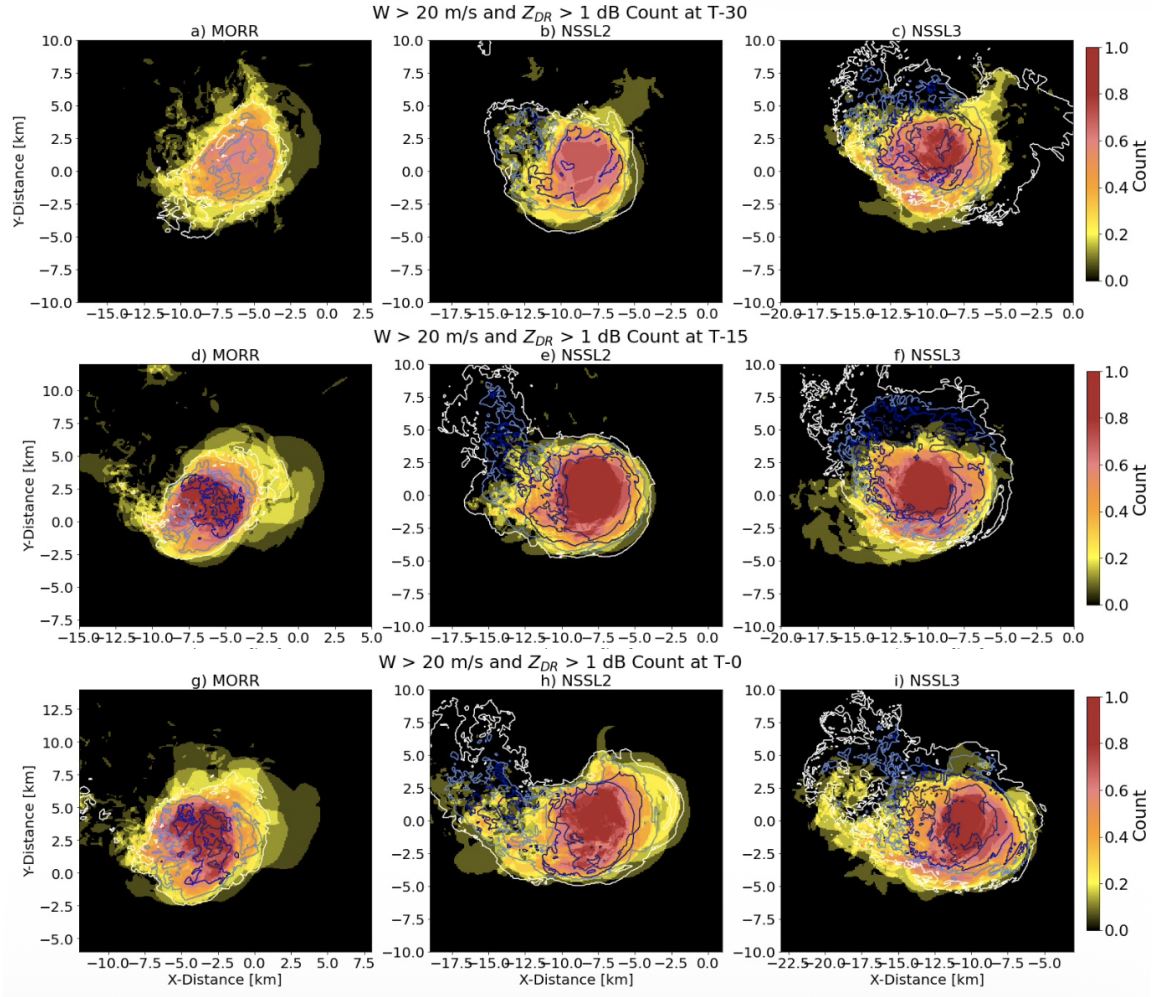


Figure 4.9: Horizontal cross-section of the frequency $w > 20$ m s^{-1} (colorfill) and $Z_{DR} > 1$ dB (contours) at 5.5 km AGL occurs across all ensemble members. The blue contours are plotted for the following levels: 0.2, 0.4, 0.6, and 0.8 dB, with darker blues representing a higher frequency of occurrence of $Z_{DR} > 1$ dB.

Finally, the impact of the microphysics scheme on the vertical alignment of $\zeta_{sfc,max}$ and $w_{1km} > 20$ m s^{-1} was tested, since the alignment between the near-surface vertical vorticity and low-level updraft has been shown to be important for tornado formation (Markowski and Richardson, 2014). To do this, the horizontal displacement of $\zeta_{sfc,max}$ and the center of the region of $w_{1km} > 20$ m s^{-1} for each ensemble member were calculated and then plotted over time in Fig. 4.10.

Between T-15 and T-0, the 1 km updraft and $\zeta_{sfc,max}$ converge in the MORR ensemble (Fig. 4.10a). There are exceptions to this, as seen in the higher percentile contours (light blue) which do not approach 0 km even near T-0 (Fig. 4.10a). In the NSSL2 ensemble, the 50^{th} percentile (black line) of horizontal displacement of $\zeta_{sfc,max}$ and the updraft remains near 0 km from T-30 to T-0 (Fig. 4.10b). However, there is variability across the NSSL2 ensemble in the displacement as shown by the red colorfill in Fig. 4.10b. What is clear is that there is no single time in the NSSL2 ensemble when the location of $\zeta_{sfc,max}$ converges with the 1 km updraft as seen in the MORR ensemble (Fig. 4.10b). Finally, the NSSL3 ensemble shows $\zeta_{sfc,max}$ aligning with the low-level updraft between T-10 and T (Fig. 4.10c). Thus, the selected microphysics scheme has a clear impact on the alignment of surface rotation and the low-level updraft prior to tornadogenesis.

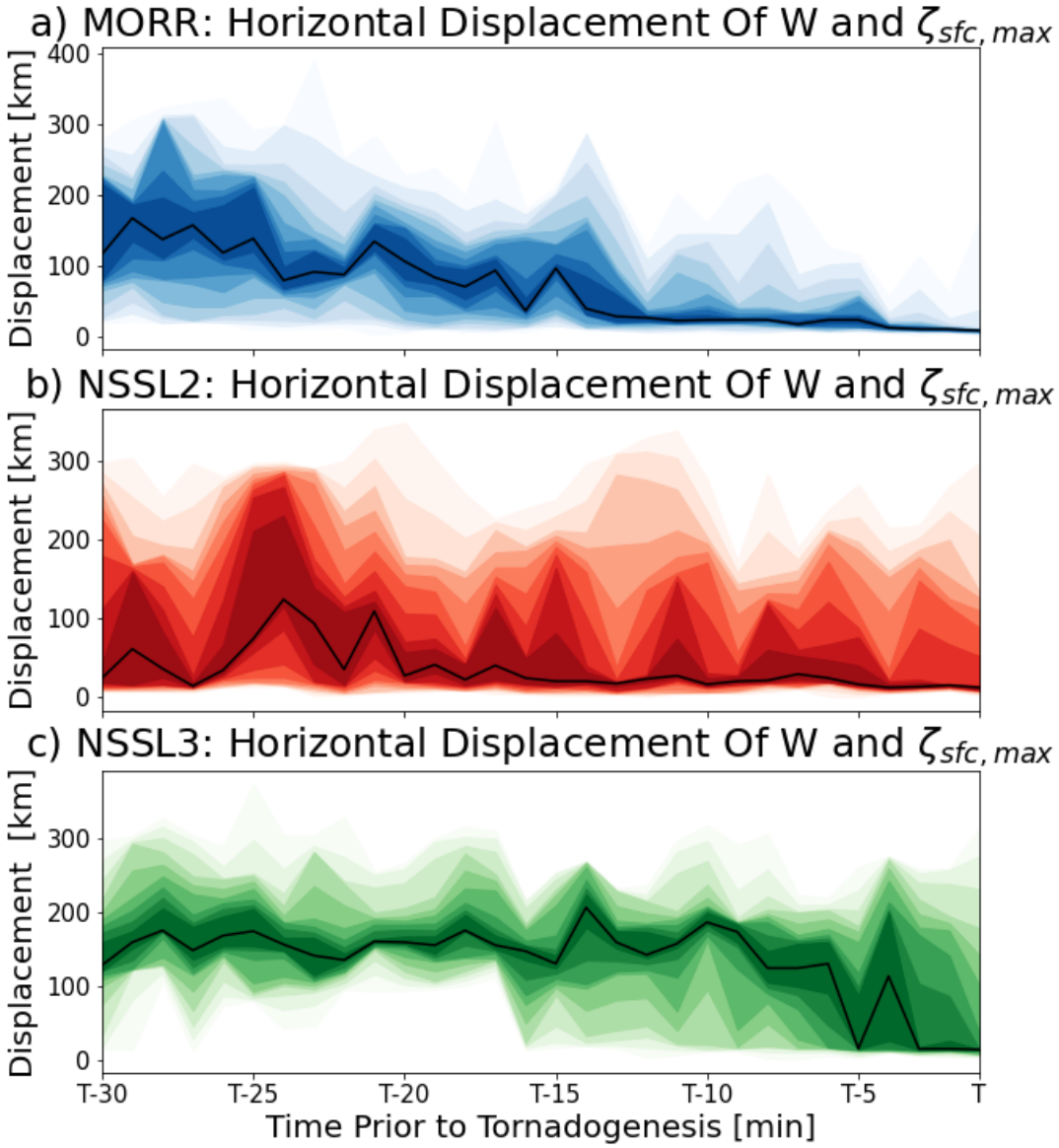


Figure 4.10: Time series of the horizontal displacement of w_max at 1 km AGL from $\zeta_{sfc,max}$ for the a) MORR, b) NSSL2, and c) NSSL3 ensembles. Black lines represent the 50$^{\text{th}}$ percentile while the colorfill ranges from the 0$^{\text{th}}$ to the 100$^{\text{th}}$ percentile.

4.3.3 Cold Pool Characteristics

The areal extent and temperature of the cold pool are another important feature of a supercell, as the gradients along the edge of the cold pool are thought to be responsible for the horizontal generation of baroclinic vorticity Wicker and Wilhelmson (1995); Markowski et al. (2002). Additionally, the strength of the cold pool has been shown to impact tornado potential (Fischer and Dahl, 2020). In general, it is thought that a stronger cold pool creates a stronger horizontal temperature gradient that, in turn, produces baroclinically generated vorticity. However, if the cold pool is too cold, it generates excessive negative buoyancy, which inhibits vertical motion and tornado potential.

It is clear that the MORR ensemble produces the largest average cold pool size of the three ensembles, followed by the NSSL2 ensemble, and then the NSSL3 ensemble which produced the smallest cold pool on average (Fig. 4.11b). Notably, the NSSL3 cold pool is nearly an order of magnitude smaller than the MORR ensemble. In terms of the strength of the cold pool, the NSSL2 ensemble produced the strongest cold pools, while the NSSL3 ensemble produced the weakest (Fig. 4.11d). The differences seen in minimum cold pool temperatures and sizes between the 3-moment and 2-moment microphysics schemes match what was found in Dawson et al. (2010), who showed that higher-moment schemes had smaller, weaker cold pools that were more consistent with observations. In their study, the warmer temperatures in the cool pools of the triple-moment scheme are attributed to the extra constraint that the reflectivity moment places on size sorting.

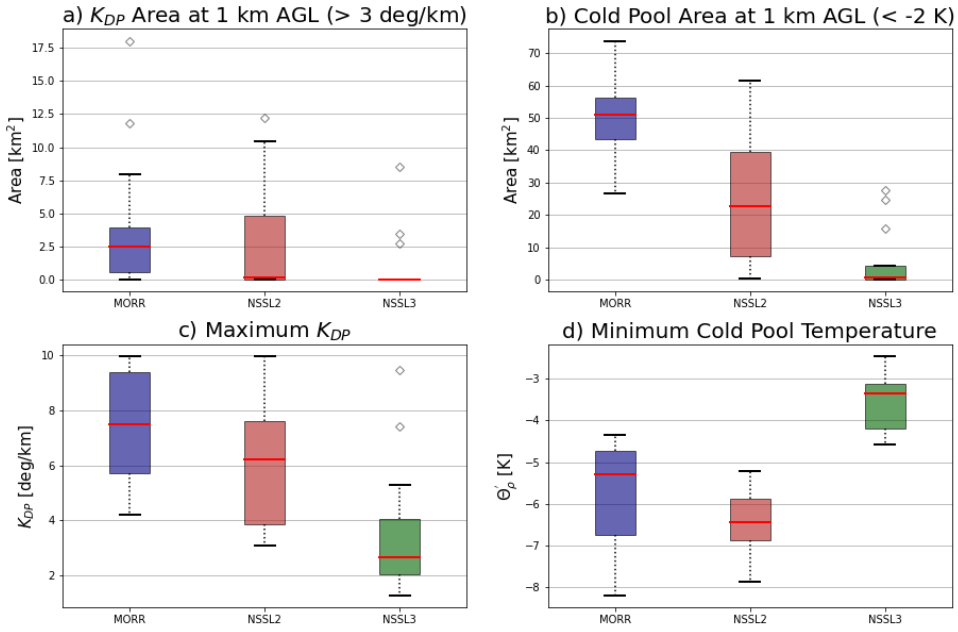


Figure 4.11: a) K_{DP} foot area area, b) cold pool area, c) maximum K_{DP}, and d) minimum cold pool temperature at T-0 at 1 km AGL the MORR (blue), NSSL2 (red), and NSSL3 (green) microphysics schemes. Black lines represent the range of the data; red horizontal lines show the location of the median; and the color-filled boxes range from the 25$^{\text{th}}$ to 75$^{\text{th}}$ percentile.

The structure of the cold pool was evaluated in a similar manner as the updraft in Fig. 4.9, but with a threshold of θ'_ρ < -2 K for the cold pool at the surface. In general, the cold pool across all ensembles became more spatially coherent between T-30 and T-0 (Fig. 4.12). This means that, despite the differences in the drop breakup parameters in the MORR ensemble and the CCN concentration in the NSSL ensembles, the location of θ'_ρ < -2 K was generally the same at the time of tornadogenesis. The MORR ensemble at T-30 had signals of the rear flank downdraft in some of the ensemble members and generally had the largest region of spatial coherence across the ensembles, though this is likely due to the MORR ensemble having the largest cold pools (Fig. 4.11b).

Also, the cold pool area decreased over the 30-min window prior to tornadogenesis (Fig. 4.13). The decrease in cold pool area occurred gradually between T-30 and T-0 in the MORR ensemble (Fig. 4.13a). The NSSL2 ensemble had a decrease in cold pool area between T-30 and T-25 before slightly increasing between T-25 and T-10 (Fig. 4.13b). From T-10 to T-0, the cold pool area in the NSSL2 ensemble decreased once more, reaching its minimum value in the 30 min period at T-0 (Fig. 4.13b). Finally, the cold pool area in the NSSL3 ensemble decreased between T-22 and T-17 (Fig. 4.13c). Since the cold pool in the NSSL3 ensemble was warmer than the MORR and NSSL2 ensembles, it is challenging to assess the temporal trend of the cold pool area past T-15 at a θ'_ρ < -2 K threshold. What is certain, however, is that microphysics schemes impact the area, strength, structure, and evolution of the cold pool.

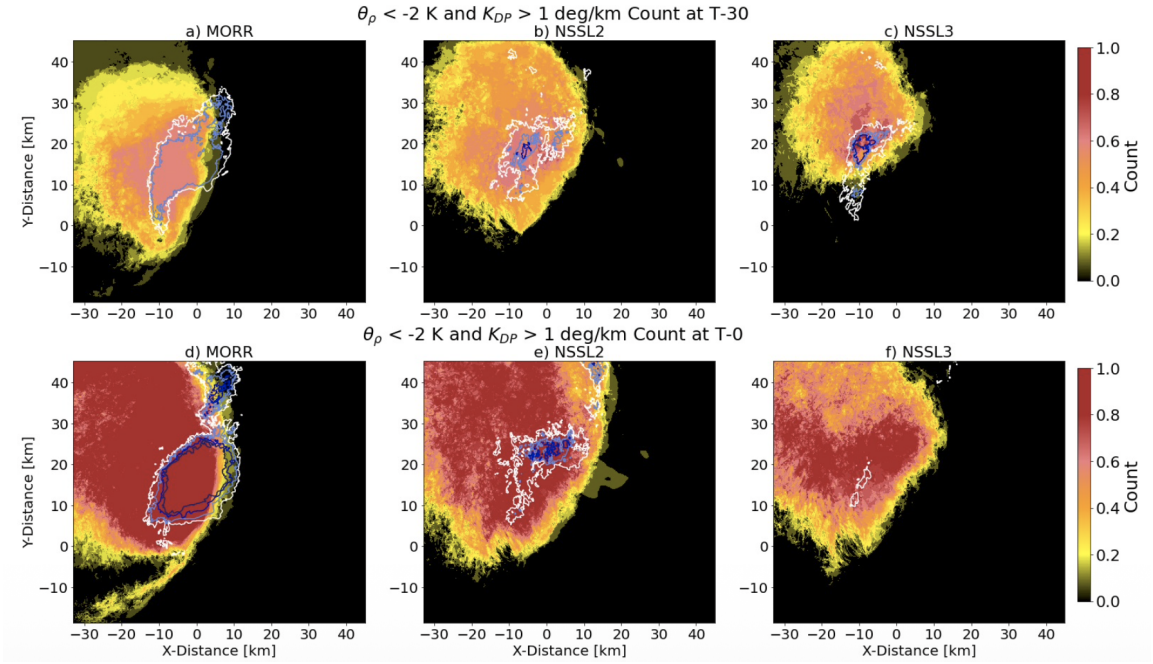


Figure 4.12: Horizontal cross-section of the frequency θ'_p < - 2 K (colorfill) and $K_{DP} > 1$ deg/km (contours) at 0.04 km AGL occurs across all ensemble members. The blue contours are plotted for the following levels: 0.2, 0.4, 0.6, and 0.8, with darker blues representing a higher frequency of occurrence of $K_{DP} > 1$ deg/km.

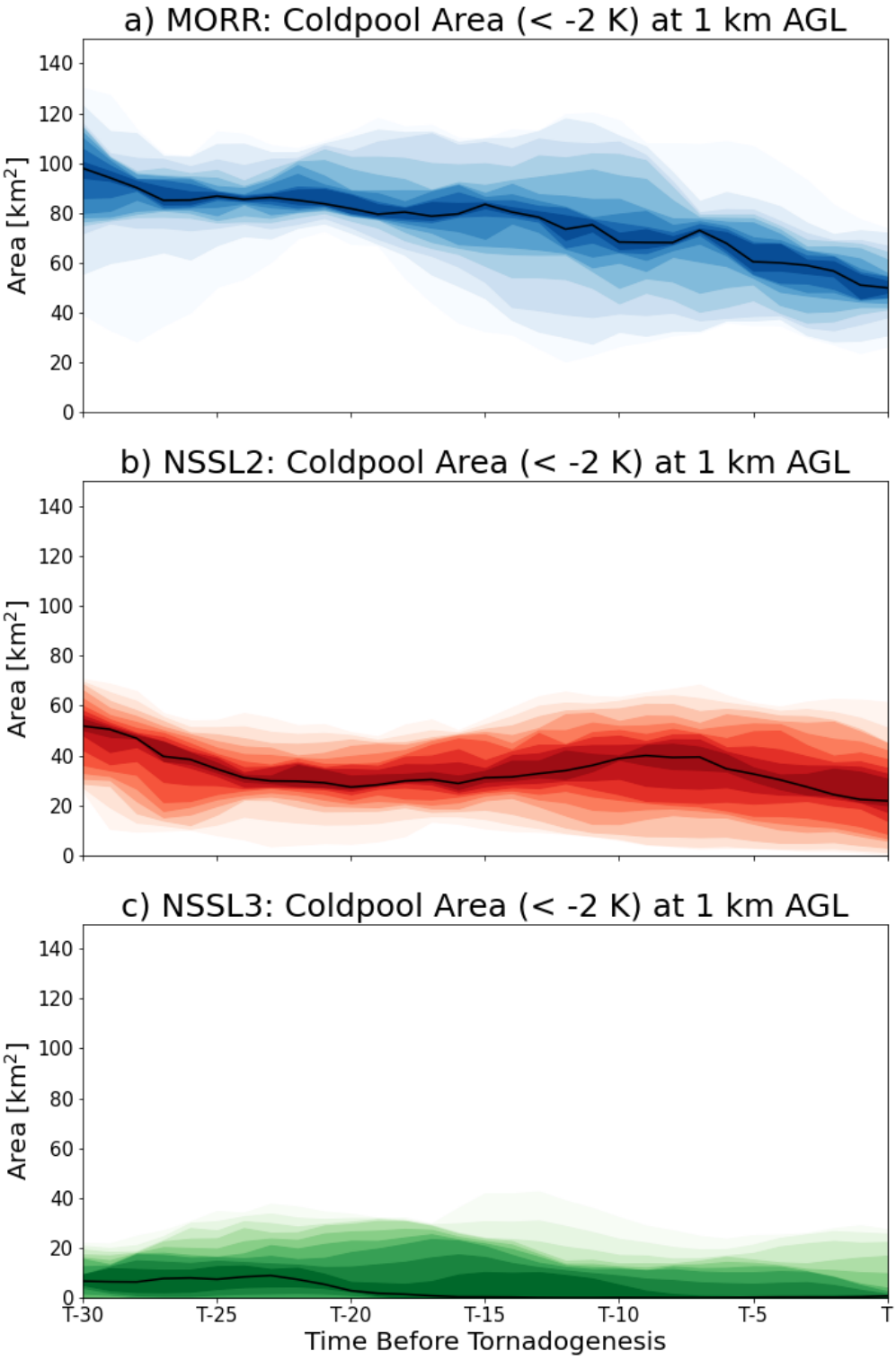


Figure 4.13: Time series of the cold pool area at 1 km AGL for the a) MORR, b) NSSL2, and c) NSSL3 ensembles. Black lines represent the 50$^{\text{th}}$ percentile while the colorfill ranges from the 0$^{\text{th}}$ to the 100$^{\text{th}}$ percentile.

4.3.4 Relationships Between Polarimetric Signatures and Supercell Dynamics

In this section, the modeled relationships between polarimetric radar signatures and supercell dynamics will be explored, starting with the spatial relationship between the Z_{DR} column and updraft. To assess this relationship, the count of $Z_{DR} > 1$ dB was overlaid atop the count of $w > 20$ m s^{-1} in Fig. 4.9.

In the MORR ensemble, the Z_{DR} column is most often collocated with the region of $w > 20$ m s^{-1} between T-30 and T-0 (Fig. 4.9a). At T-30, some MORR ensemble members produce a Z_{DR} column that extends to the southwest, where the updraft extends southwestward (Fig. 4.9a). At T-0, the Z_{DR} column extends into the updraft tail in some of the MORR ensemble members, while the majority of the MORR ensemble has the Z_{DR} column in a north-to-south line (see dark blue contours in Fig. 4.9g).

The NSSL2 ensemble at T-30 has a Z_{DR} column that is mostly quasi-circular, with some ensemble members producing a column that extends to the northwest (Fig. 4.9b). At T-15, the Z_{DR} column produces a stream of Z_{DR} to the northwest of the updraft core (Fig. 4.9b). This stream or "tail" of Z_{DR} persists to T-0 where the "tail" widens (Fig. 4.9e,h). Most ensemble members, however, produce a column that widens over time and remains quasi-circular (Fig. 4.9b,e,h).

At T-30, the NSSL3 ensemble has the largest region of low agreement across the ensembles (Fig. 4.9c). This means that few realizations of the NSSL3 ensemble produced columns that extended to the northwest and east of the updraft core (Fig. 4.9c). Like the NSSL2 ensemble, the region of highest agreement across the NSSL3 ensemble is collocated with the $w > 20$ m s^{-1} updraft and is quasi-circular (Fig. 4.9c). At T-15, the region of low agreement extends to the north and is not collocated with the updraft tail seen in Fig. 4.9f. These two features become more collocated at T-0 as

the expanse of the Z_{DR} column extends more to the northeast (Fig. 4.9i). Finally, the region of high agreement across the NSSL3 ensemble is quite variable, with multiple, smaller regions of high spatial coherence within the $w > 20$ m s^{-1} updraft (Fig. 4.9i). Overall, each ensemble produces a Z_{DR} column that is generally collocated with the 20 s^{-1} updraft. Also, the high-frequency area of $Z_{DR} > 1$ dB generally matches the high-frequency area of $w > 20$ m s^{-1}, especially in the MORR and NSSL2 ensembles (Fig. 4.9).

Examining the previously observed relationship between tornado intensity and Z_{DR} column area in French and Kingfield (2021), a plot of w_{max} and Z_{DR} column area is shown in Fig. 4.14. Generally, the microphysics schemes that produce more intense updrafts at tornadogenesis produce, on average, wider Z_{DR} columns (Fig. 4.14). The NSSL3 scheme had, on average, the largest columns (80 km^2) while the MORR scheme produced the smallest on average (40 km^2). It is interesting to note that the MORR scheme creates the largest $V_{h,max}$ at T-0 (Fig. 4.2), yet the Z_{DR} columns of the MORR scheme are smaller than those produced by the NSSL3 scheme, which produces the lowest $V_{h,max}$ at T-0 (Fig. 4.14b). This implies that the size of the Z_{DR} columns in the simulated supercells is modulated more by the 5.5 km AGL updraft strength than the intensity of the tornado at tornadogenesis. However, it should be noted that each ensemble produced significant (EF3+) tornadoes, and it is probable that the size of the Z_{DR} column shows more correlation with tornado strength across a wider range of tornado intensities.

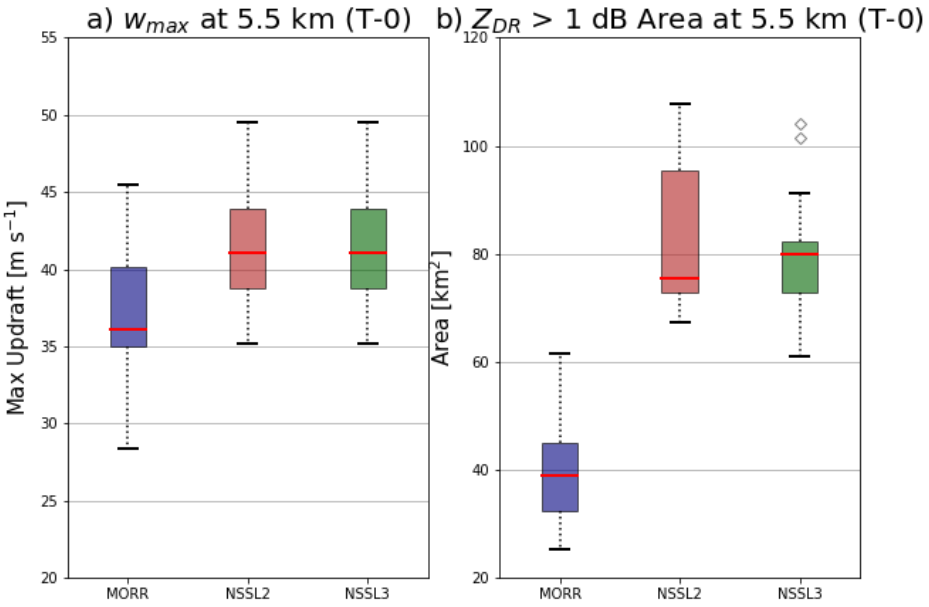


Figure 4.14: Box plots of a) w_{max} and b) Z_{DR} column area at T-0 and 5.5 km AGL for the MORR (blue), NSSL2 (red), and NSSL3 (green) microphysics schemes. Black lines represent the range of the data; red horizontal lines show the location of the median; and the color-filled boxes range from the 25$^{\text{th}}$ to 75$^{\text{th}}$ percentile.

In addition to the Z_{DR} column, the area and structure of the K_{DP} foot were also evaluated. Since K_{DP} is linearly related to rainfall rate (Sachidananda and Zrnić, 1985), the magnitude of K_{DP} can be a good measure of the amount of liquid water present in a given volume. It has also been shown that values of enhanced K_{DP} can also indicate regions of negative buoyancy as well, which is pertinent for tornado potential (Carlin and Ryzhkov, 2019).

The location and structure of the K_{DP} foot is compared to the cold pool in Fig. 4.12. At T-30, the MORR ensemble produces a K_{DP} foot that extends south with part of the cold pool (Fig. 4.12a). The NSSL3 ensemble produces a K_{DP} foot with a similar southward protrusion of the K_{DP} foot, but in the NSSL3 ensemble, the K_{DP} foot extends

past where the cold pool commonly resides in most ensemble members (Fig. 4.12c). Meanwhile, at T-30, the NSSL2 ensemble produces a K_{DP} foot that is collocated near the center of the cold pool (Fig. 4.12b).

At the time of tornadogenesis, the K_{DP} foot in the MORR ensemble widens and develops a separate enhancement of K_{DP} to the north of the main foot (Fig. 4.12d). The increase in K_{DP} foot area is also shown in Fig. 4.11a, with the MORR scheme producing the largest K_{DP} foot on average at T-0. The K_{DP} foot in the NSSL2 ensemble retains a similar structure between T-30 and T-0, but there is a larger region of agreement across the ensembles in the K_{DP} foot location at T-0 (Fig. 4.12e). Finally, the K_{DP} foot in the NSSL3 ensemble does not exist in most of the ensemble members due to the low frequency of the K_{DP} foot contour in Fig. 4.12f. This is due to the magnitude of K_{DP} decreasing from T-30 to T-0 in the NSSL3 ensemble (not shown).

The area of the K_{DP} foot is also evaluated over time in comparison with the evolution of the cold pool (Fig. 4.13 and 4.15). The Pearson correlation coefficient (r) was also calculated for the 50^{th} percentile values in the cold pool and K_{DP} foot areas for each ensemble member. The area of the K_{DP} foot decreases in the MORR and NSSL2 ensembles between T-10 and T-0, while the K_{DP} foot area in the NSSL3 ensemble decreases from T-22 to T-17 (Fig. 4.15). There is a relatively weak correlation ($r = 0.62$) between the cold pool and K_{DP} foot area over time in the MORR ensemble, but in the NSSL ensembles, the cold pool and K_{DP} foot areas decrease in the same time period (Fig. 4.13 and 4.15). The correlation between the cold pool and K_{DP} foot areas over time is $r = 0.75$ in the NSSL2 ensemble and $r = 0.92$ in the NSSL3 ensemble. The MORR scheme also had the largest range of K_{DP} foot area values across the ensemble members (0 km^2 – 31 km^2) compared to the NSSL2 and NSSL3 schemes (0 km^2 – 19 km^2 and 0 km^2 – 10 km^2, respectively). While the temporal correlation between decreases in the cold pool and K_{DP} foot areas varied across ensemble members, it is

overall evident that supercells with larger cold pools tended to produce larger regions of enhanced K_{DP}.

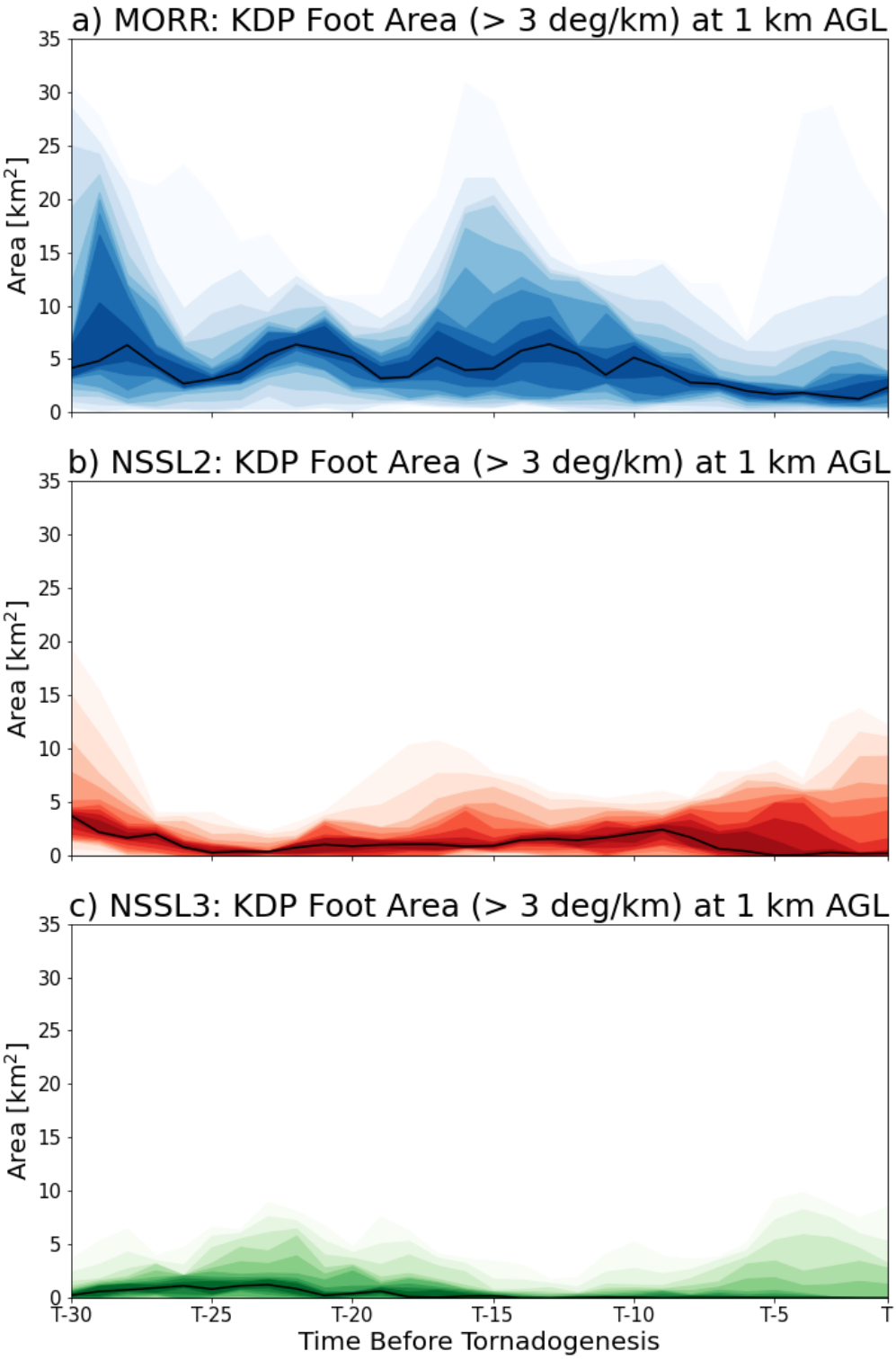


Figure 4.15: Time series of the K_{DP} foot area at 1 km AGL for the a) MORR, b) NSSL2, and c) NSSL3 ensembles. Black lines represent the 50$^{\text{th}}$ percentile while the colorfill ranges from the 0$^{\text{th}}$ to the 100$^{\text{th}}$ percentile.

Finally, the Z_{DR}-K_{DP} separation angle and distance were assessed in Fig. 4.16. In previous work, the Z_{DR} K_{DP} separation angle has been studied as a way of discriminating between tornadic and nontornadic supercells (Loeffler et al., 2020; Homeyer et al., 2020; Wilson and Van Den Broeke, 2022). Such work has found that a distinguishing feature of tornadic supercells is a more orthogonal orientation of the Z_{DR}-K_{DP} separation vector to storm motion. In the simulated supercells in this study, each ensemble produces a Z_{DR}-K_{DP} separation vector that is orthogonal to the storm motion vector, similar to what was shown in Loeffler et al. (2020). Generally, the NSSL ensembles produced larger separation distances than the MORR ensemble, but the separation angle across the three ensembles was quite similar (Fig. 4.16). Thus, while the evolution of the K_{DP} foot and Z_{DR} column areas is sensitive to the selected microphysics scheme, the orientation of the Z_{DR}-K_{DP} separation vector represents what is seen in observed supercells, regardless of the microphysics scheme used.

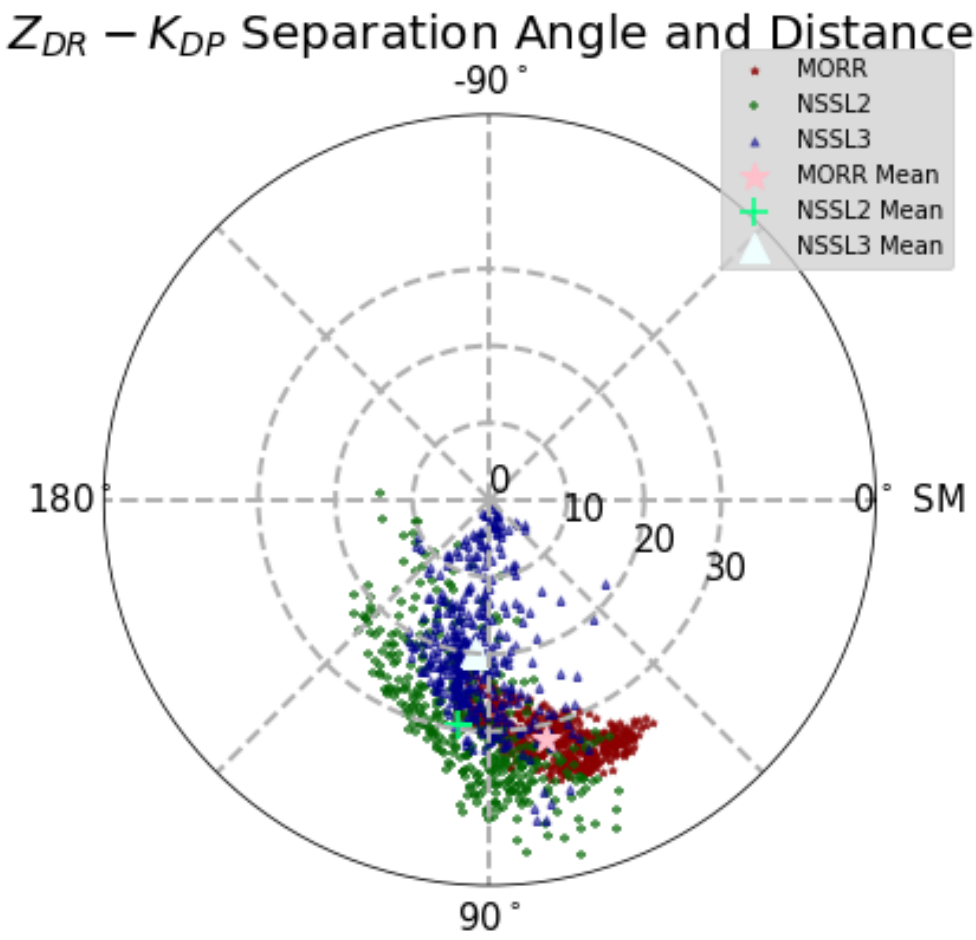


Figure 4.16: Plot of the Z_{DR}-K_{DP} separation angle and distance for the MORR (red), NSSL2 (green), and NSSL3 (blue) ensembles at 0.04 km AGL. Scatter points represent the distance and angle for each ensemble member in the 30-min prior to tornadogenesis. The 0°angle is aligned with storm motion (SM).

4.3.5 Conclusion

Previous work has highlighted the impact of BMPs on supercell dynamics and thermodynamics (e.g., Snook and Xue, 2008; Morrison and Milbrandt, 2011; Dawson et al., 2015b). However, it remains relatively unknown how different BMPs impact the relationships between polarimetric radar signatures and storm dynamics in tornadic super-

cells. Given the insight that polarimetric radar signatures provide into microphysical processes, evaluating how BMPs resolve (or fail to resolve) polarimetric signatures is important for evaluating how well they simulate a realistic supercell. Since supercell simulations have a significant influence on the trajectory of supercell research, it is crucial to document how different BMPs affect polarimetric signatures and supercell dynamics (e.g., the Z_{DR} column and updraft).

To evaluate different BMPs and their impact on supercell dynamics, thermodynamics, and the relationship between supercell dynamics and polarimetric signatures, an ensemble of tornadic supercells was simulated using CM1. Each ensemble was created by varying the microphysical parameters across three microphysics schemes: the Morrison 2-moment, NSSL 2-moment, and NSSL 3-moment schemes. Polarimetric radar variables were obtained through a modified forward operator from Zhang et al. (2021) coupled with a combined melting model adapted from Jung et al. (2008) and Liu et al. (2024a).

Fig. 4.17 provides a summary of some of the metrics used to evaluate supercell dynamics and thermodynamics across each BMP. The MORR scheme typically produced shorter-lived tornadoes at EF5 intensity compared to the NSSL schemes, but the tornadoes reached a higher peak $V_{h,max}$. While the MORR scheme produced the strongest tornadoes, it also produced the smallest updraft areas at both 1 and 5.5 km when using a w $>$ 20 m s^{-1} threshold. This result contrasts with Sessa and Trapp (2020), who showed that stronger tornadoes typically had wider, low-level mesocyclones. The different methods of determining tornado intensity could explain some of the differences between this study and Sessa and Trapp (2020). Also, the parameterized method for resolving phase changes in the BMPs may account for some of the discrepancies between observed studies, such as Sessa and Trapp (2020), and the results from our simulations. Since the area of the 5.5 km AGL updraft core generally follows the region

of maximum θ'_ρ (Fig. 4.8), changes in the temperature field would likely alter the area of the updraft. How phase changes are resolved in each BMP would directly impact θ'_ρ, and thus the area of the updraft core. However, future work should evaluate the direct correlation between changes in latent heat release and in updraft area to fully test this hypothesis.

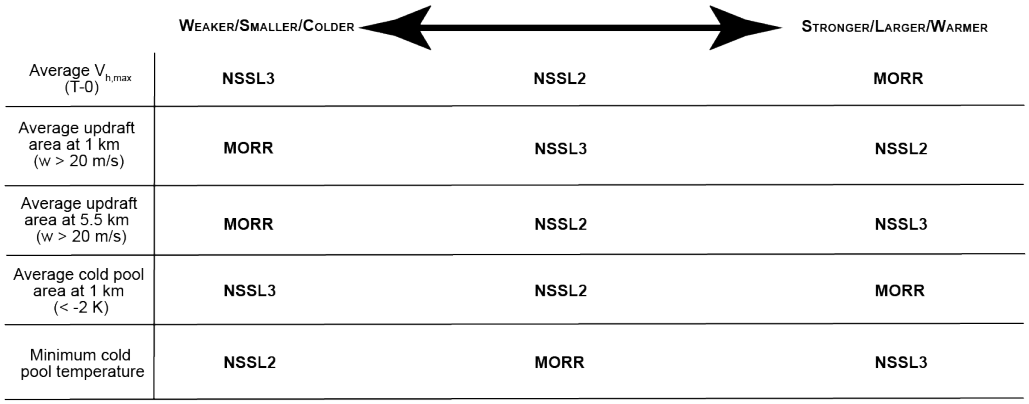


Figure 4.17: Summary of the conclusions for each microphysics scheme for the updraft area, cold pool area, $V_{h,max}$, and the minimum cold pool temperature.

The evolution of $\zeta_{sfc,max}$ and the centroids of $\zeta_{sfc,max}$ and the 1 km updraft were also assessed. It was shown that the 2-moment schemes produced stronger, average ζ_{max} than the NSSL3 scheme; however, the evolution of ζ_{max} in the NSSL3 scheme best represents the evolution of rotation observed by RaXPoL for the 24 May 2011 case in Houser et al. (2015). Additionally, the two-moment schemes showed an alignment between $\zeta_{sfc,max}$ and the updraft core at 1 km, which has been shown in prior work to be beneficial for tornadogenesis (Markowski and Richardson, 2014). This alignment was also seen in the triple-moment scheme, but for a short period of time (< 5 min) before tornadogenesis.

The MORR scheme produced the largest cold pool, while the NSSL2 and MORR schemes generally produced colder cold pools compared to the NSSL3 scheme. Results from Dawson et al. (2015b) show that triple-moment schemes have less evaporation of

rain, which could explain why the NSSL3 scheme had a warmer cold pool than the two-moment schemes. Furthermore, differences in microphysics schemes resulted in order of magnitude differences in cold pool area, with the MORR ensemble producing the largest cold pools on average and the NSSL3 scheme producing the smallest on average.

Finally, polarimetric radar signatures were also compared to supercell dynamics and thermodynamics. It was shown that each ensemble produced a Z_{DR} column that is generally collocated with the 20 m s^{-1} updraft. Also, the NSSL3 scheme produced, on average, the largest Z_{DR} column areas and strongest updraft speeds at 5.5 km AGL, while the MORR scheme produced the smallest Z_{DR} column areas and weakest updraft speeds. French and Kingfield (2021) showed that stronger tornadoes generally produced larger Z_{DR} column areas. However, in the simulated supercells in this study, the MORR scheme had the strongest average $V_{h,max}$ at T-0 and the strongest maximum $V_{h,max}$ during the tornado, yet produced the smallest Z_{DR} column areas. Likewise, the NSSL3 scheme produced the weakest average $V_{h,max}$ at T-0 and the weakest minimum $V_{h,max}$ during the tornado, yet produced the largest Z_{DR} column areas on average. This likely implies the upper-level updraft modulates Z_{DR} column areas more than the low-level $V_{h,max}$ in these simulated supercells. Since each of the simulated supercells produced intense (EF3+) tornadoes, it is unlikely that these results will translate to an observed set of supercells with a larger range of tornado intensities. Thus, these results hold only for this specific set of ensembles and for supercells that produce EF3+ tornadoes.

The evolution of the K_{DP} foot was also analyzed alongside that of the cold pool. It was shown that, in the NSSL schemes, the K_{DP} foot area generally decreased in the same 5 – 10 min window as the cold pool area decreased, with the NSSL3 scheme showing the largest correlation in the temporal trend between the cold pool and K_{DP} foot

area. Also, the ensemble that produced the largest cold pool area (MORR) also produced, on average, the largest K_{DP} foot area, while the ensemble that produced the smallest cold pool area (NSSL3) produced the smallest K_{DP} foot areas on average. Finally, the MORR scheme exhibited the greatest variability in the K_{DP} foot area among ensemble members compared to the NSSL2 and NSSL3 schemes.

Finally, the Z_{DR}-K_{DP} separation angle and distance were evaluated for each microphysics scheme. In previous work (Loeffler et al., 2020; Homeyer et al., 2020; Wilson and Van Den Broeke, 2022), it has been shown that tornadic supercells have an orthogonal orientation between the Z_{DR}-K_{DP} separation and storm motion vectors. Despite triple-moment schemes better resolving size sorting (Dawson et al., 2010), the double- and triple-moment microphysics schemes used in this study produced the orthogonal orientation of the Z_{DR}-K_{DP} separation vector seen in observations.

This study shows that BMPs can recreate the observed relationships between polarimetric radar signatures and supercell dynamics, especially in the NSSL schemes which showed both an orthogonal orientation of the Z_{DR}-K_{DP} separation vector, a relationship between decreases in the K_{DP} foot area and cold pool area, and produced stronger updrafts that, in turn, produced larger Z_{DR} column areas. While it is unknown what the cold pool and updraft characteristics of the El Reno tornado of 24 May 2011 were, it is clear from comparisons to the evolution of rotation in Houser et al. (2015) that the NSSL3 scheme best recreates the vertical evolution of $\bar{\zeta}_{max}$. However, the NSSL3 scheme seemingly shows a correlation between the time of tornadogenesis and CCN in addition to a correlation between $V_{h,max}$ at 0.04 km AGL and CCN, which has yet to be explained. Future work should delve deeper into the relationships between the latent heat absorbed or released during phase change and updraft characteristics for each microphysics scheme, as it is likely the parameterizations of hydrometeor phase changes that are creating the differences across supercell dynamics and thermodynam-

ics outlined in this study. Future work should also seek to compare different BMPs to observations of supercell dynamics and thermodynamics obtained from field projects to assess which BMP accurately resolves supercell cold pool and updraft characteristics.

Chapter 5

Summary and Conclusions

Given the challenges of retrieving the three-dimensional wind field in real time, dual-polarization radar signatures are important for forecasting tornado formation (or failure), as they provide information about the microphysical and dynamical evolution of supercells. The majority of studies have focused on climatological observations of dual-polarization radar signatures or a detailed study of one supercell (e.g., Van Den Broeke, 2017; Loeffler et al., 2020; Homeyer et al., 2020; Van Den Broeke, 2020; Tuftedal et al., 2021; French and Kingfield, 2021; Segall et al., 2022; Healey and Van Den Broeke, 2023; Houser et al., 2015; Bluestein et al., 2019; Wakimoto et al., 2020; Van Den Broeke et al., 2023), which are important for understanding how these signatures vary across different environments and tornado intensities. Fewer studies have focused on both the temporal evolution of dual-polarization radar signatures and their variation across supercells within the same event. Furthermore, studies have also used numerical models to simulate dual-polarization radar signatures. Numerical models can provide high spatiotemporal resolution and insights into supercell dynamics, thermodynamics, and microphysics. While much of the previous work has focused on the individual development of a forward operator or applications of a forward operator across different microphysics schemes (e.g., Shima et al., 2009; Ryzhkov et al., 2011; Matsui et al., 2019; Oue et al., 2020; Zhang et al., 2021; Jung et al., 2008; Dawson II et al., 2014; Johnson et al., 2016; Liu et al., 2024b), few (if any) studies have combined the forward operator output with observations in a detailed study of polarimetric

signature structure and evolution in tornadic supercells. Furthermore, this study leverages the computational efficiency of the polarimetric forward operator by applying it to large ensembles of high-resolution simulations from different microphysics schemes, which is not feasible with higher fidelity radar simulation frameworks incorporating a fully scanning radar. The work in this dissertation fills this gap in the literature by providing an observed case study of the evolution of polarimetric signatures during the 24 – 25 May 2011 outbreak and by evaluating polarimetric signatures in more detail through an ensemble of simulations of the supercell that produced the 24 May 2011 El Reno tornado.

From the observations, the polarimetric signatures showed distinct differences between the 3 tornadic and 3 nontornadic supercells. The tornadic supercells exhibited Z_{DR} rings within 8 min of tornadogenesis, had larger mean areas for all polarimetric signatures, and had larger separation angles than the nontornadic supercells. The progression of the separation angle during the 30-min window prior to tornadogenesis revealed that the differences between the nontornadic and tornadic supercells were maximized between T-15 and T. Each of the tornadic supercells also exhibited similar development of the Z_{DR} arc. This arc development was characterized by an enhanced region of Z_{DR} ($Z_{DR} > 3$ dB) in the western portion of the supercell, the appearance of a Z_{DR} "hole," and subsequent attachment of the arc to the forward flank of the supercell. The nontornadic supercells also generally followed this progression of the arc, but given the lack of data during the early genesis of the Z_{DR} enhancement region for the nontornadic supercells, it was challenging to verify the early development of the arc for these supercells.

The evaluation of the simulated polarimetric signatures began by assessing different melting models and their impact on the signatures. The three melting models evaluated were the Jung et al. (2008) (J08), Liu et al. (2024b) (L24), and a novel Combined

Melting Model (CMM) developed in this study. It was shown that the new CMM creates the most realistic distribution of ice hydrometeors throughout the supercell, limits ice above the freezing level to the vicinity of the updraft, and produces a distribution of D_m that primarily yielded $D_m < 10$ mm, while still allowing a few instances of larger ice hydrometeors. The CMM also combined the D_m and Z_{DR} relationships from the L24 and J08 models, resulting in a melting model that produced realistic relationships between D_m and Z_{DR}. The L24 behaved similarly to the CMM and was the only model to limit D_m to smaller sizes, producing better relationships between D_m and Z_{DR} for ice hydrometeors with a thin water torus. However, the CMM yielded better-looking polarimetric signatures than the L24 model and removed the Z_{DR} artifact above the freezing level in the J08 model.

After assessing which melting model best represented ice hydrometeors in simulated tornadic supercells, the CMM and a modified version of the PFO were used to compare polarimetric signatures across three different microphysics schemes: the NSSL 2-moment (NSSL2), NSSL 3-moment (NSSL3), and Morrison 2-moment (MORR) schemes. It was found that the NSSL3 scheme best represented polarimetric signatures below the freezing level, while the MORR scheme best represented signatures above the freezing level. However, the NSSL2 scheme best represented the overall size of the observed supercell and the range of Z_H.

Finally, the simulation ensembles were used to assess the relationships between supercell dynamics and polarimetric radar signatures. It was found that the NSSL3 scheme best represented the evolution of $\zeta_{sfc,max}$ through the lowest 3 km when compared with the vertical evolution of rotation observed by RaXPoL for the 24 May 2011 case documented in Houser et al. (2015). Also, the NSSL schemes produced larger updrafts on average than the MORR scheme both at 1 km and above the freezing level, despite each ensemble having the same environmental profile. Though, the NSSL3

scheme produced smaller and warmer cold pools compared to both of the 2-moment schemes.

When looking at the polarimetric signature and dynamical relationships, it was shown that the Z_{DR} column was generally collocated with the 20 m s^{-1} updraft across each ensemble. Furthermore, it was shown that the MORR scheme produced the strongest average $V_{h,max}$, the strongest updraft speeds at 5.5 km AGL, and created the smallest Z_{DR} column areas. The NSSL3 scheme produced the weakest average $V_{h,max}$, the weakest updraft speeds at 5.5 km AGL, and created the largest Z_{DR} column areas. This implies the upper-level updraft modulates Z_{DR} column areas more than $V_{h,max}$ in these simulated supercells. However, this finding is limited to this specific set of supercell simulations that produce EF3+ tornadoes.

The relationship between the cold pool and K_{DP} foot was also assessed in these simulated ensembles. It was shown that supercells that produced the smallest K_{DP} foot also had the smallest cold pools. The MORR scheme produced the largest cold pool and K_{DP} foot while the NSSL3 scheme produced the smallest cold pool and K_{DP} foot. Finally, despite triple-moment schemes better resolving size sorting, each scheme used in this study produced the orthogonal orientation of the Z_{DR}-K_{DP} separation vector seen in the observed supercells on 24 May 2011. While microphysics schemes with greater magnitudes of cooling were shown to be associated with larger K_{DP} foots, the centroid of the K_{DP} foot did not change substantially enough in these schemes to impact the orientation.

The results of the polarimetric signatures simulations highlight a new CMM for tornadic supercells and the impact of the selected microphysics scheme on both the structure and evolution of the polarimetric signatures. However, there are still limitations to the CMM and PFO in producing realistic polarimetric signatures. For instance, each scheme produced large regions with high Z_H magnitudes ($Z_H > 60$ dBZ) com-

pared with observations. These regions of high Z_H are dominated by melting graupel and hail, which in BMPs the sizes of hail are governed by and derived from the number concentration (Wu et al., 2022). The number concentration in simulations is highly uncertain, so future work should focus on improved parameterizations of the number concentration of melting ice species in BMPs. Furthermore, the melting models tested in this work apply a single f_w for each hydrometeor species in each model grid cell. A better (albeit more computationally expensive) approach would be to allow f_w to vary with hydrometeor size, as done in Dawson II et al. (2014).

The combination of the CMM and PFO provides a powerful tool that can be used to study simulated polarimetric signatures and perform intercomparisons with observations. This includes different convective modes and associated hazards, such as quasi-linear convective systems, downbursts, nontornadic supercells, and single- and multicell thunderstorms. Future improvements to the polarimetric emulator include adding a beam pattern and angular weighting to emulate an operational radar (Cheong et al., 2017; Mahre et al., 2020). These improvements would enable future studies to assess the impact of radar range and resolution on the evolution of polarimetric signatures. Additionally, future work could include formulating a new set of fitted equations for different radar wavelengths, such as Ka- or X-band. Smaller wavelengths would allow for better comparison of the simulated polarimetric signatures with mobile radar data, such as the Rapid X-band Polarimetric Radar or the mobile Ka-band radars from the Texas Tech University National Wind Institute.

In addition to improvements to the polarimetric emulator, the work presented herein leads to more science questions, such as:

- What physical processes are occurring in tornadic supercells that lead to larger Z_{DR} arc and K_{DP} foot separation angles 15 min prior to tornadogenesis?

- What is the relationship between the latent heat absorbed or released during phase change and updraft characteristics for each microphysics scheme?
- Why does CCN concentration impact the strength of the surface winds in NSSL3 scheme but not in the NSSL2 scheme?

Such questions can be answered either by a more detailed analysis at the simulations used in this study or, in the case of the first question, by high-temporal observations from mobile radars including phased array radars (Palmer et al., 2023; Bodine and Griffin, 2024). Such observations could include a combination of bistatic radars and RaXPoL (Emmerson et al., 2025), which would allow for the retrieval of the three-dimensional wind field in addition to collection of high-temporal resolution polarimetric data.

Overall, the novelty of this dissertation lies in the better understanding of the lifecycle of observed polarimetric signatures and the validation of ensembles of high-resolution idealized supercell simulations with polarimetric radar observations. A deeper understanding of the temporal evolution of polarimetric radar signatures can provide insight into the microphysical and dynamical evolution of observed storms. This knowledge can help inform operational meteorologists about developing hazards, such as tornadoes, as well as information future research on dual-polarization radar signatures. The work herein highlights the need for further verification of idealized simulations of supercells with observations and additional observations of the full life-cycle of observed supercells.

Reference List

Ashley, W. S., 2007: Spatial and temporal analysis of tornado fatalities in the united states: 1880–2005. *Weather and Forecasting*, **22 (6)**, 1214 – 1228, https://doi.org/10.1175/2007WAF2007004.1, URL https://journals.ametsoc.org/view/journals/wefo/22/6/2007waf2007004_1.xml.

Balakrishnan, N., and D. S. Zrnić, 1990: Use of polarization to characterize precipitation and discriminate large hail. *J. Atmos. Sci.*, **47**, 1525–1540.

Benjamin, S. G., and Coauthors, 2004: An hourly assimilation/forecast cycle: The RUC. *Mon. Wea. Rev.*, **132**, 495–518.

Bluestein, H. B., K. J. Thiem, J. C. Snyder, and J. B. Houser, 2019: Tornadogenesis and early tornado evolution in the El Reno, Oklahoma supercell on 31 May 2013. *Mon. Wea. Rev.*, **147**, 2045 – 2066.

Bodine, D., M. R. Kumjian, R. D. Palmer, P. L. Heinselman, and A. V. Ryzhkov, 2013: Tornado damage estimation using polarimetric radar. *Wea. Forecasting*, **28**, 139–158.

Bodine, D. J., and C. B. Griffin, 2024: REVIEW: Meteorological research enabled by rapid-scan radar technology. *Mon. Wea. Rev.*, **152**, 3–37, https://doi.org/10.1175/MWR-D-22-0324.1.

Bodine, D. J., R. D. Palmer, and G. Zhang, 2014: Dual-wavelength polarimetric radar analyses of tornadic debris signatures. *J. Appl. Meteor. Climatol.*, **53**, 242–261.

Brooks, H. E., and J. Correia, 2018: Long-term performance metrics for national weather service tornado warnings. *Weather and Forecasting*, **33 (6)**, 1501 – 1511.

Bryan, G. H., and J. M. Fritsch, 2002: A benchmark simulation for moist nonhydrostatic numerical models. *Monthly Weather Review*, **130 (12)**, 2917 – 2928, https://doi.org/10.1175/1520-0493(2002)130⟨2917:ABSFMN⟩2.0.CO;2, URL https://journals.ametsoc.org/view/journals/mwre/130/12/1520-0493_2002_130_2917_absfmn_2.0.co_2.xml.

Carlin, J. T., and A. V. Ryzhkov, 2019: Estimation of melting-layer cooling rate from dual-polarization radar: Spectral bin model simulations. *Journal of Applied Meteorology and Climatology*, **58 (7)**, 1485 – 1508.

Cheong, B. L., D. J. Bodine, C. J. Fulton, S. M. Torres, T. Maruyama, and R. D. Palmer, 2017: SimRadar: A polarimetric radar time-series simulator for tornadic debris studies. *IEEE Trans. Geosci. Remote Sensi.*, **55**, 2858 – 2870.

Coffer, B. E., M. D. Parker, J. M. L. Dahl, L. J. Wicker, and A. J. Clark, 2017a: Volatility of tornadogenesis: An ensemble of simulated nontornadic and tornadic supercells in vortex2 environments. *Monthly Weather Review*, **145 (11)**, 4605 – 4625, https://doi.org/10.1175/MWR-D-17-0152.1, URL https://journals.ametsoc.org/view/journals/mwre/145/11/mwr-d-17-0152.1.xml.

Coffer, B. E., M. D. Parker, J. M. L. Dahl, L. J. Wicker, and A. J. Clark, 2017b: Volatility of tornadogenesis: An ensemble of simulated nontornadic and tornadic supercells in VORTEX2 environments. *Mon. Wea. Rev.*, **145**, 4605 – 4625, https://doi.org/10.1175/MWR-D-17-0152.1.

Coffer, B. E., M. D. Parker, J. M. Peters, and A. R. Wade, 2023: Supercell low-level mesocyclones: Origins of inflow and vorticity. *Monthly Weather Review*, **151 (9)**, 2205 – 2232, https://doi.org/10.1175/MWR-D-22-0269.1, URL https://journals.ametsoc.org/view/journals/mwre/151/9/MWR-D-22-0269.1.xml.

Cross, R. N., and Coauthors, 2023: Exploring tornadic debris signature hypotheses using radar simulations and large-eddy simulations. *J. Atmos. Oceanic Technol.*, **40**, 1199–1219, https://doi.org/10.1175/JTECH-D-22-0141.1.

Dahl, J. M. L., 2015: Near-ground rotation in simulated supercells: On the robustness of the baroclinic mechanism. *Monthly Weather Review*, **143 (12)**, 4929 – 4942, https://doi.org/10.1175/MWR-D-15-0115.1, URL https://journals.ametsoc.org/view/journals/mwre/143/12/mwr-d-15-0115.1.xml.

Davies-Jones, R., 2015: A review of supercell and tornado dynamics. *Atmospheric Research*, **158-159**, 274–291.

Davies-Jones, R., R. Trapp, and H. Bluestein, 2001: Tornadoes and tornadic storms. *Meteorological Monographs*, **28**, https://doi.org/10.1175/0065-9401-28.50.167.

Dawson, D. T., E. R. Mansell, and M. R. Kumjian, 2015a: Does wind shear cause hydrometeor size sorting? *Journal of the Atmospheric Sciences*, **72 (1)**, 340 – 348, https://doi.org/10.1175/JAS-D-14-0084.1, URL https://journals.ametsoc.org/view/journals/atsc/72/1/jas-d-14-0084.1.xml.

Dawson, D. T., M. Xue, J. A. Milbrandt, and A. Shapiro, 2015b: Sensitivity of real-data simulations of the 3 may 1999 oklahoma city tornadic supercell and associated tornadoes to multimoment microphysics. part i: Storm- and tornado-scale numerical

forecasts. *Monthly Weather Review*, **143 (6)**, 2241 – 2265, https://doi.org/10.1175/MWR-D-14-00279.1, URL https://journals.ametsoc.org/view/journals/mwre/143/6/mwr-d-14-00279.1.xml.

Dawson, D. T., M. Xue, J. A. Milbrandt, and M. K. Yau, 2010: Comparison of evaporation and cold pool development between single-moment and multimoment bulk microphysics schemes in idealized simulations of tornadic thunderstorms. *Monthly Weather Review*, **138 (4)**, 1152 – 1171, https://doi.org/10.1175/2009MWR2956.1, URL https://journals.ametsoc.org/view/journals/mwre/138/4/2009mwr2956.1.xml.

Dawson II, D. T., E. R. Mansell, Y. Jung, L. J. Wicker, M. R. Kumjian, and M. Xue, 2014: Low-level Z_{DR} signatures in supercell forward flanks: The role of size sorting and melting of hail. *J. Atmos. Sci.*, **71**, 276 – 299, https://doi.org/https://doi.org/10.1175/JAS-D-13-0118.1.

Dawson II, D. T., E. R. Mansell, and M. R. Kumjian, 2015: Does wind shear cause hydrometeor size sorting? *Journal of the Atmospheric Sciences*, **72 (1)**, 340 – 348, https://doi.org/10.1175/JAS-D-14-0084.1, URL https://journals.ametsoc.org/view/journals/atsc/72/1/jas-d-14-0084.1.xml.

Doviak, R. J., V. Bringi, A. Ryzhkov, A. Zahrai, and D. Zrnić, 2000: Considerations for polarimetric upgrades to operational WSR-88D radars. *J. Atmos. Oceanic Technol.*, **17**, 257 – 278.

Du, M., J. Gao, G. Zhang, Y. Wang, P. L. Heiselman, and C. Cui, 2021: Assimilation of polarimetric radar data in simulation of a supercell storm with a variational approach and the wrf model. *Remote Sensing*, **13 (16)**, https://doi.org/10.3390/rs13163060, URL https://www.mdpi.com/2072-4292/13/16/3060.

Emmerson, S., R. Palmer, D. Bodine, D. Schvartzman, P. Kirstetter, P. Skinner, and C. Fulton, 2025: Retrieval and quantitative evaluation of three-dimensional winds in severe convection with multistatic radar. *J. Atmos. Oceanic Technol.*, **42 (9)**, 1167 – 1183, https://doi.org/10.1175/JTECH-D-24-0155.1.

Eure, K. C., D. J. Stensrud, Y. Zhang, M. R. Kumjian, and D. M. Kingfield, 2025: Simultaneous assimilation of dual-polarization radar and all-sky satellite observations to improve convection forecasts. *Monthly Weather Review*, **153 (11)**, 2397 – 2414, https://doi.org/10.1175/MWR-D-24-0157.1, URL https://journals.ametsoc.org/view/journals/mwre/153/11/MWR-D-24-0157.1.xml.

Fischer, J., and J. M. L. Dahl, 2020: The relative importance of updraft and cold pool characteristics in supercell tornadogenesis using highly idealized simulations.

Journal of the Atmospheric Sciences, **77 (12)**, 4089 – 4107, https://doi.org/10.1175/JAS-D-20-0126.1, URL https://journals.ametsoc.org/view/journals/atsc/77/12/jasD200126.xml.

Fischer, J., and J. M. L. Dahl, 2023: Supercell-external storms and boundaries acting as catalysts for tornadogenesis. *Monthly Weather Review*, **151 (1)**, 23 – 38, https://doi.org/10.1175/MWR-D-22-0026.1, URL https://journals.ametsoc.org/view/journals/mwre/151/1/MWR-D-22-0026.1.xml.

Fischer, J., J. M. L. Dahl, B. E. Coffer, J. L. Houser, P. M. Markowski, M. D. Parker, C. C. Weiss, and A. Schueth, 2024: Supercell tornadogenesis: Recent progress in our state of understanding. *Bull. Amer. Meteor. Soc.*, **105**, E1084—E1097, https://doi.org/10.1175/BAMS-D-23-0031.1.

Fischer, J., M. Kunz, K. Lombardo, and M. R. Kumjian, 2025: Hail trajectories in a wide spectrum of supercell-like updrafts. *Journal of the Atmospheric Sciences*, **82 (7)**, 1403 – 1422, https://doi.org/10.1175/JAS-D-24-0222.1, URL https://journals.ametsoc.org/view/journals/atsc/82/7/JAS-D-24-0222.1.xml.

Flournoy, M. D., M. C. Coniglio, E. N. Rasmussen, J. C. Furtado, and B. E. Coffer, 2020: Modes of storm-scale variability and tornado potential in vortex2 near- and far-field tornadic environments. *Monthly Weather Review*, **148 (10)**, 4185 – 4207, https://doi.org/10.1175/MWR-D-20-0147.1, URL https://journals.ametsoc.org/view/journals/mwre/148/10/mwrD200147.xml.

French, M., P. Skinner, L. Wicker, and H. Bluestein, 2015: Documenting a rare tornado merger observed in the 24 may 2011 el reno-piedmont, oklahoma, supercell. *Monthly Weather Review*, **143**, 150505125047 001, https://doi.org/10.1175/MWR-D-14-00349.1.

French, M. M., and D. M. Kingfield, 2021: Tornado formation and intensity prediction using polarimetric radar estimates of updraft area. *Weather and Forecasting*, **36 (6)**, 2211 – 2231.

Gallus Jr., W. A., and M. Pfeifer, 2008: Intercomparison of simulations using 5 wrf microphysical schemes with dual-polarization data for a german squall line. *Advances in Geosciences*, **16**, 109–116, https://doi.org/10.5194/adgeo-16-109-2008, URL https://adgeo.copernicus.org/articles/16/109/2008/.

Gibbs, J. G., 2016: A skill assessment of techniques for real-time diagnosis and short-term prediction of tornado intensity using the WSR-88D. *J. Operational Meteor.*, **4**, 170–181.

Gilmore, J. M. S., M. S., and E. N. Rasmussen, 2004a: Precipitation and evolution sensitivity in simulated deep convective storms: Comparisons between liquid-only and simple ice and liquid phase microphysics. *Mon. Wea. Rev.*, **132**, 1897—-1916.

Grzych, M. L., B. D. Lee, and C. A. Finley, 2007: Thermodynamic analysis of supercell rear-flank downdrafts from project answers. *Monthly Weather Review*, **135 (1)**, 240 – 246.

Healey, D. J., and M. S. V. D. Broeke, 2025: Zdr columns in simulated qlcss: Column-updraft relationships and differences between two microphysics schemes. *Monthly Weather Review*, **153 (12)**, 2669 – 2688, https://doi.org/10.1175/MWR-D-25-0031.1, URL https://journals.ametsoc.org/view/journals/mwre/153/12/MWR-D-25-0031.1.xml.

Healey, D. J., and M. S. Van Den Broeke, 2023: Comparing polarimetric signatures of proximate pretornadic and nontornadic supercells in similar environments. *Weather and Forecasting*, **38 (10)**, 2011 – 2027.

Heinselman, P. L., D. S. LaDue, and H. Lazrus, 2012: Exploring impacts of rapid-scan radar data on NWS warning decisions. *Weather and Forecasting*, **27 (4)**, 1031 – 1044, https://doi.org/10.1175/WAF-D-11-00145.1, URL https://journals.ametsoc.org/view/journals/wefo/27/4/waf-d-11-00145_1.xml.

Heinselman, P. L., and Coauthors, 2024: Warn-on-forecast system: From vision to reality. *Weather and Forecasting*, **39 (1)**, 75 – 95, https://doi.org/10.1175/WAF-D-23-0147.1, URL https://journals.ametsoc.org/view/journals/wefo/39/1/WAF-D-23-0147.1.xml.

Helmus, J. J., and S. M. Collis, 2016: The python arm radar toolkit (py-art), a library for working with weather radar data in the python programming language. *Journal of Open Research Software*, **4 (1)**, e25.

Heymsfield, A. J., M. A. Cecchini, A. Detwiler, R. Honeyager, and P. Field, 2023: Exploring the composited t-28 hailstorm penetration dataset to characterize hail properties within the updraft and downdraft regions. *Journal of Applied Meteorology and Climatology*, **62 (12)**, 1803 – 1826, https://doi.org/10.1175/JAMC-D-23-0030.1, URL https://journals.ametsoc.org/view/journals/apme/62/12/JAMC-D-23-0030.1.xml.

Hirth, B. D., J. L. Schroeder, and C. C. Weiss, 2008: Surface analysis of the rear-flank downdraft outflow in two tornadic supercells. *Monthly Weather Review*, **136 (7)**, 2344 – 2363.

Homeyer, C. R., T. N. Sandmæl, C. K. Potvin, and A. M. Murphy, 2020: Distinguishing characteristics of tornadic and nontornadic supercell storms from composite mean analyses of radar observations. *Mon. Wea. Rev.*, **148 (12)**, 5015 – 5040, https://doi.org/10.1175/MWR-D-20-0136.1, URL https://journals.ametsoc.org/view/journals/mwre/148/12/mwr-d-20-0136.1.xml.

Houser, J. L., H. B. Bluestein, and J. C. Snyder, 2015: Rapid-scan, polarimetric, doppler radar observations of tornadogenesis and tornado dissipation in a tornadic supercell: The "el reno, oklahoma" storm of 24 may 2011. *Mon. Wea. Rev.*, **143**, 2685 – 2710.

Houston, A. L., C. C. Weiss, E. N. Rasmussen, M. C. Coniglio, C. L. Ziegler, B. M. Argrow, and E. W. Frew, 2026: Targeted observation by radars and uas of supercells: Torus. *Bulletin of the American Meteorological Society*, **107 (2)**, E249 – E276, https://doi.org/10.1175/BAMS-D-23-0265.1, URL https://journals.ametsoc.org/view/journals/bams/107/2/BAMS-D-23-0265.1.xml.

Hubbert, J., V. N. Bringi, L. D. Carey, and S. Bolen, 1998: Csu-chill polarimetric radar measurements from a severe hail storm in eastern colorado. *Journal of Applied Meteorology*, **37 (8)**, 749 – 775, https://doi.org/10.1175/1520-0450(1998)037⟨0749:CCPRMF⟩2.0.CO;2, URL https://journals.ametsoc.org/view/journals/apme/37/8/1520-0450_1998_037_0749_ccprmf_2.0.co_2.xml.

Jameson, A. R., and E. A. Mueller, 1985: Estimation of propagation-differential phase shift from sequential orthogonal linear polarization radar measurements. *Journal of Atmospheric and Oceanic Technology*, **2 (2)**, 133 – 137, https://doi.org/10.1175/1520-0426(1985)002⟨0133:EOPDPS⟩2.0.CO;2, URL https://journals.ametsoc.org/view/journals/atot/2/2/1520-0426_1985_002_0133_eopdps_2_0_co_2.xml.

Johnson, M., Y. Jung, D. T. Dawson, and M. Xue, 2016: Comparison of simulated polarimetric signatures in idealized supercell storms using two-moment bulk microphysics schemes in WRF. *Mon. Wea. Rev.*, **144**, 971 – 996.

Johnson, P. K. W., D. E., and J. M. Straka, 1993: Numerical simulations of the 2 august 1981 CCOPE supercell storm with and without ice microphysics. *J. Appl. Meteor.*, **32**, 745—-759.

Jung, Y., M. Xue, and G. Zhang, 2010: Simulations of polarimetric radar signatures of a supercell storm using a two-moment bulk microphysics scheme. *J. Appl. Meteor. Climatol.*, **49**, 146 – 163, https://doi.org/https://doi.org/10.1175/2009JAMC2178.1.

Jung, Y., M. Xue, G. Zhang, and J. M. Straka, 2008: Assimilation of simulated polarimetric radar data for a convective storm using the ensemble Kalman filter. Part II:

Impact of polarimetric data on storm analysis. *Mon. Wea. Rev.*, **136**, 2246 – 2260.

Khain, A. P., and Coauthors, 2015: Representation of microphysical processes in cloud-resolving models: Spectral (bin) microphysics versus bulk parameterization. *Reviews of Geophysics*, **53 (2)**, 247–322, https://doi.org/https://doi.org/10.1002/2014RG000468, URL https://agupubs.onlinelibrary.wiley.com/doi/abs/10.1002/2014RG000468, https://agupubs.onlinelibrary.wiley.com/doi/pdf/10.1002/2014RG000468.

Klees, A. M., Y. P. Richardson, P. M. Markowski, C. T. Weiss, J. M. Wurman, and K. Kosiba, 2016: Comparison of the tornadic and nontornadic supercells intercepted by VORTEX2 on 10 June 2010. *Mon. Wea. Rev.*, **144**, 3201 – 3231, https://doi.org/10.1175/MWR-D-15-0345.1.

Kumjian, M., A. V. Ryzhkov, V. M. Melnikov, and T. J. Schuur, 2010: Rapid-scan super-resolution observations of a cyclic supercell with a dual-polarization WSR-88D. *Mon. Wea. Rev.*, **138**, 3762–3786.

Kumjian, M. R., 2013: Principles and applications of dual-polarization weather radar. Part I: Description of the polarimetric radar variables. *J. Operational Meteor.*, **1**, 226 – 242.

Kumjian, M. R., A. P. Khain, N. Benmoshe, E. Ilotoviz, A. V. Ryzhkov, and V. T. J. Phillips, 2014: The anatomy and physics of ZDR columns: Investigating a polarimetric radar signature with a spectral bin microphysical model. *Journal of Applied Meteorology and Climatology*, **53 (7)**, 1820 – 1843, https://doi.org/10.1175/JAMC-D-13-0354.1.

Kumjian, M. R., and K. Lombardo, 2020: A hail growth trajectory model for exploring the environmental controls on hail size: Model physics and idealized tests. *Journal of the Atmospheric Sciences*, **77 (8)**, 2765 – 2791, https://doi.org/10.1175/JAS-D-20-0016.1, URL https://journals.ametsoc.org/view/journals/atsc/77/8/jasD200016.xml.

Kumjian, M. R., K. Lombardo, and S. Loeffler, 2021: The evolution of hail production in simulated supercell storms. *Journal of the Atmospheric Sciences*, **78 (11)**, 3417 – 3440, https://doi.org/10.1175/JAS-D-21-0034.1, URL https://journals.ametsoc.org/view/journals/atsc/78/11/JAS-D-21-0034.1.xml.

Kumjian, M. R., and A. V. Ryzhkov, 2008: Polarimetric signatures in supercell thunderstorms. *J. Appl. Meteor. Climatol.*, **48**, 1940–1961.

Kumjian, M. R., and A. V. Ryzhkov, 2009: Storm-relative helicity revealed from po-

larimetric radar measurements. *J. Atmos. Sci.*, **66**, 667–685.

Kurdzo, J. M., D. J. Bodine, B. L. Cheong, and R. D. Palmer, 2015: High-temporal resolution polarimetric X-band Doppler radar observations of the 20 May 2013 Moore, Oklahoma tornado. *Mon. Wea. Rev.*, **143**, 2711 – 2735.

Kurdzo, J. M., and Coauthors, 2017: Observations of severe local storms and tornadoes with the Atmospheric Imaging Radar. *Bull. Amer. Meteor. Soc.*, **98**, 915 – 935, https://doi.org/https://doi.org/10.1175/BAMS-D-15-00266.1.

Lee, . F. J. M., S., 2022: Mental health impacts of tornadoes: A systematic review. *International Journal of Environmental Research and Public Health*, **19 (21)**, https://doi.org/https://doi.org/10.3390/ijerph192113747.

Liu, P., J. Gao, G. Zhang, and J. T. Carlin, 2024a: Assimilation of radar reflectivity data using parameterized forward operators for improving short-term forecasts of high-impact convection events. *Journal of Geophysical Research: Atmospheres*, **129 (20)**, e2024JD041 458, https://doi.org/https://doi.org/10.1029/2024JD041458, URL https://agupubs.onlinelibrary.wiley.com/doi/abs/10.1029/2024JD041458, e2024JD041458 2024JD041458, https://agupubs.onlinelibrary.wiley.com/doi/pdf/10.1029/2024JD041458.

Liu, P., G. Zhang, J. T. Carlin, and J. Gao, 2024b: A new melting model and its implementation in parameterized forward operators for polarimetric radar data simulation with double moment microphysics schemes. *Journal of Geophysical Research: Atmospheres*, **129**, https://doi.org//10.1029/2023JD040026.

Loeffler, S. D., and M. R. Kumjian, 2018: Quantifying the separation of enhanced Z_{DR} and K_{DP} regions in nonsupercell tornadic storms. *Wea. Forecasting*, **33**, 1143 – 1157, https://doi.org/https://doi.org/10.1175/WAF-D-18-0011.1.

Loeffler, S. D., M. R. Kumjian, M. Jurewicz, and M. M. French, 2020: Differentiating between tornadic and nontornadic supercells using polarimetric radar signatures of hydrometeor size sorting. *Geophysical Research Letters*, **47**, 2211 – 2231.

Loney, M. L., D. S. Zrnić, J. M. Straka, and A. V. Ryzhkov, 2002: Enhanced polarimetric radar signatures above the melting level in a supercell storm. *Journal of Applied Meteorology*, **41 (12)**, 1179 – 1194, https://doi.org/10.1175/1520-0450(2002)041⟨1179:EPRSAT⟩2.0.CO;2, URL https://journals.ametsoc.org/view/journals/apme/41/12/1520-0450_2002_041_1179_eprsat_2.0.co_2.xml.

Mahre, A., T.-Y. Yu, and D. J. Bodine, 2020: A comparison of scan speedup strategies and their effect on rapid-scan weather radar data quality. *J. Atmos. Oceanic Technol.*,

37, 1955 – 1972, https://doi.org/10.1175/JTECH-D-19-0216.1.

Mansell, E. R., D. T. D. II, and J. M. Straka, 2020: Bin-emulating hail melting in three-moment bulk microphysics. *Journal of the Atmospheric Sciences*, **77 (10)**, 3361 – 3385, https://doi.org/10.1175/JAS-D-19-0268.1, URL https://journals.ametsoc.org/view/journals/atsc/77/10/jasD190268.xml.

Mansell, E. R., C. L. Ziegler, and E. C. Bruning, 2010: Simulated electrification of a small thunderstorm with two-moment bulk microphysics. *Journal of the Atmospheric Sciences*, **67 (1)**, 171 – 194, https://doi.org/10.1175/2009JAS2965.1, URL https://journals.ametsoc.org/view/journals/atsc/67/1/2009jas2965.1.xml.

Marion, G. R., R. J. Trapp, and S. W. Nesbitt, 2019: Using overshooting top area to discriminate potential for large, intense tornadoes. *Geophys. Res. Lett.*, **46**, 12 520–12 526.

Markowski, P., and Y. Richardson, 2010: *Mesoscale Meteorology in Midlatitudes*. John Wiley and Sons, https://doi.org/10.1002/9780470682104.

Markowski, P. M., 2002: Hook echoes and rear-flank downdrafts: A review. *Mon. Wea. Rev.*, **130**, 852–876.

Markowski, P. M., 2020: What is the intrinsic predictability of tornadic supercell thunderstorms? *Monthly Weather Review*, **148 (8)**, 3157 – 3180.

Markowski, P. M., and Y. P. Richardson, 2009: Tornadogenesis: Our current understanding, forecasting considerations, and questions to guide future research. *Atmos. Research*, **93**, 3–10.

Markowski, P. M., and Y. P. Richardson, 2014: The influence of environmental low-level shear and cold pools on tornadogenesis: Insights from idealized simulations. *Journal of the Atmospheric Sciences*, **71 (1)**, 243 – 275.

Markowski, P. M., J. M. Straka, and E. N. Rasmussen, 2002: Direct surface thermodynamic observations within the rear-flank downdrafts of nontornadic and tornadic supercells. *Monthly Weather Review*, **130 (7)**, 1692 – 1721.

Matsui, T., B. Dolan, S. A. Rutledge, W.-K. Tao, T. Iguchi, J. Barnum, and S. E. Lang, 2019: Polarris: A polarimetric radar retrieval and instrument simulator. *Journal of Geophysical Research: Atmospheres*, **124 (8)**, 4634–4657, https://doi.org/https://doi.org/10.1029/2018JD028317, URL https://agupubs.onlinelibrary.wiley.com/doi/abs/10.1029/2018JD028317, https://agupubs.onlinelibrary.wiley.com/doi/pdf/10.1029/2018JD028317.

Milbrandt, J. A., and M. K. Yau, 2005a: A multimoment bulk microphysics parameterization. part i: Analysis of the role of the spectral shape parameter. *J. Atmos. Sci.*, **62**, 3051–3064.

Milbrandt, J. A., and M. K. Yau, 2005b: A multimoment bulk microphysics parameterization. part ii: A proposed three-moment closure and scheme description. *J. Atmos. Sci.*, **62**, 3065–3081.

Morrison, H., J. A. Curry, and V. I. Khvorostyanov, 2005: A new double-moment microphysics parameterization for application in cloud and climate models. Part I: Description. *J. Atmos. Sci.*, **62**, 1665 – 1677.

Morrison, H., and J. Milbrandt, 2011: Comparison of two-moment bulk microphysics schemes in idealized supercell thunderstorm simulations. *Monthly Weather Review*, **139 (4)**, 1103 – 1130, https://doi.org/10.1175/2010MWR3433.1, URL https://journals.ametsoc.org/view/journals/mwre/139/4/2010mwr3433.1.xml.

Morrison, H., and J. A. Milbrandt, 2015: Parameterization of cloud microphysics based on the prediction of bulk ice particle properties. part i: Scheme description and idealized tests. *Journal of the Atmospheric Sciences*, **72 (1)**, 287 – 311, https://doi.org/10.1175/JAS-D-14-0065.1, URL https://journals.ametsoc.org/view/journals/atsc/72/1/jas-d-14-0065.1.xml.

Morrison, H., J. A. Milbrandt, and M. Cholette, 2025: A complete three-moment representation of ice in the predicted particle properties (p3) microphysics scheme. *Journal of Advances in Modeling Earth Systems*, **17 (4)**, e2024MS004 644, https://doi.org/https://doi.org/10.1029/2024MS004644, URL https://agupubs.onlinelibrary.wiley.com/doi/abs/10.1029/2024MS004644, e2024MS004644 2024MS004644, https://agupubs.onlinelibrary.wiley.com/doi/pdf/10.1029/2024MS004644.

Morrison, H., and J. O. Pinto, 2006: Intercomparison of bulk cloud microphysics schemes in mesoscale simulations of springtime arctic mixed-phase stratiform clouds. *Monthly Weather Review*, **134 (7)**, 1880 – 1900, https://doi.org/10.1175/MWR3154.1, URL https://journals.ametsoc.org/view/journals/mwre/134/7/mwr3154.1.xml.

Morrison, H., G. Thompson, and V. Tatarskii, 2009: Impact of cloud microphysics on the development of trailing stratiform precipitation in a simulated squall line: Comparison of one- and two-moment schemes. *Mon. Wea. Rev.*, **137**, 991–1007.

Naylor, J., and M. S. Gilmore, 2012: Convective initiation in an idealized cloud model using an updraft nudging technique. *Monthly Weather Review*, **140 (11)**, 3699 – 3705, https://doi.org/10.1175/MWR-D-12-00163.1, URL https://journals.ametsoc.org/view/journals/mwre/140/11/mwr-d-12-00163.1.xml.

NOAA, 2011: Storm events database. National Oceanic and Atmospheric Adminstration National Center for Environmental Information, URL https://www.ncdc.noaa.gov/stormevents/details.jsp?type=collection.

Okubo, A., 1970: Horizontal dispersion of floatable particles in the vicinity of velocity singularities such as convergences. *Deep Sea Research and Oceanographic Abstracts*, **17 (3)**, 445–454, https://doi.org/https://doi.org/10.1016/0011-7471(70)90059-8, URL https://www.sciencedirect.com/science/article/pii/0011747170900598.

Orf, L., R. Wilhelmson, B. Lee, C. Finley, and A. Houston, 2017: Evolution of a long-track violent tornado within a simulated supercell. *Bull. Amer. Meteor. Soc.*, **98**, 45 – 68, https://doi.org/https://doi.org/10.1175/BAMS-D-15-00073.1.

Oue, M., A. Tatarevic, P. Kollias, D. Wang, K. Yu, and A. M. Vogelmann, 2020: The cloud-resolving model radar simulator (CR-SIM) version 3.3: description and applications of a virtual observatory. *Geoscientific Model Development*, **13 (4)**, 1975–1998, https://doi.org/10.5194/gmd-13-1975-2020, URL https://gmd.copernicus.org/articles/13/1975/2020/.

Pal, N. R., A. K. Mandal, S. Pal, J. Das, and V. Lakshmanan, 2006: Fuzzy rule–based approach for detection of bounded weak-echo regions in radar images. *Journal of Applied Meteorology and Climatology*, **45 (9)**, 1304 – 1312, https://doi.org/10.1175/JAM2408.1, URL https://journals.ametsoc.org/view/journals/apme/45/9/jam2408.1.xml.

Palmer, R. D., and Coauthors, 2011: The 10 May 2010 tornado outbreak in central Oklahoma: Potential for new science with high-resolution polarimetric radar. *Bull. Amer. Meteor. Soc.*, **92**, 871–891.

Palmer, R. D., and Coauthors, 2023: Horus—a fully digital polarimetric phased array radar for next-generation weather observations. *IEEE Trans. Radar Systems*, **1**, 96–117, https://doi.org/10.1109/TRS.2023.3280033.

Parker, M. D., 2014: Composite VORTEX2 supercell environments from near-storm soundings. *Monthly Weather Review*, **142 (2)**, 508 – 529, https://doi.org/10.1175/MWR-D-13-00167.1, URL https://journals.ametsoc.org/view/journals/mwre/142/2/mwr-d-13-00167.1.xml.

Pazmany, A. L., J. B. Mead, H. B. Bluestein, J. C. Snyder, and J. B. Houser, 2013: A mobile rapid-scanning X-band polarimetric (RaXPol) Doppler radar system. *J. Atmos. Oceanic Technol.*, **30 (7)**, 1398–1413.

Prevatt, D. O., and Coauthors, 2012: Making the case for improved structural design:

Tornado outbreaks of 2011. *Leadership and Management in Engineering*, **12 (4)**, 254–270, https://doi.org/10.1061/(ASCE)LM.1943-5630.0000192.

Rajeevan, M., S. Gadgil, and J. Bhate, 2010: Active and break spells of the indian summer monsoon. *J. Earth Syst. Sci.*, **119**, 229–247.

Rasmussen, R. M., V. Levizzani, and H. R. Pruppacher, 1984: A wind tunnel and theoretical study on the melting behavior of atmospheric ice particles: III. Experiment and theory for spherical ice particles of radius ¿ 500 m. *Journal of Atmospheric Sciences*, **41 (3)**, 381 – 388, https://doi.org/10.1175/1520-0469(1984)041⟨0381:AWTATS⟩2.0.CO;2, URL https://journals.ametsoc.org/view/journals/atsc/41/3/1520-0469_1984_041_0381_awtats_2_0_co_2.xml.

Romine, G. S., D. W. Burgess, and R. B. Wilhelmson, 2008: A dual-polarization-radar-based assessment of the 8 May 2003 Oklahoma City area tornadic supercell. *Monthly Weather Review*, **136 (8)**, 2849 – 2870, https://doi.org/10.1175/2008MWR2330.1, URL https://journals.ametsoc.org/view/journals/mwre/136/8/2008mwr2330.1.xml.

Ryzhkov, A., M. Pinsky, A. Pokrovsky, and A. Khain, 2011: Polarimetric radar observation operator for a cloud model with spectral microphysics. *Journal of Applied Meteorology and Climatology*, **50 (4)**, 873 – 894, https://doi.org/10.1175/2010JAMC2363.1, URL https://journals.ametsoc.org/view/journals/apme/50/4/2010jamc2363.1.xml.

Ryzhkov, A. V., T. J. Schuur, D. W. Burgess, and D. S. Zrnić, 2005: Polarimetric tornado detection. *J. Appl. Meteor.*, **44**, 557–570.

Ryzhkov, A. V., J. Snyder, J. T. Carlin, A. Khain, and M. Pinsky, 2020: What polarimetric weather radars offer to cloud modelers: Forward radar operators and microphysical/thermodynamic retrievals. *Atmosphere*, **11 (4)**, https://doi.org/10.3390/atmos11040362, URL https://www.mdpi.com/2073-4433/11/4/362.

Sachidananda, M., and D. S. Zrnić, 1985: ZDR measurement considerations for a fast scan capability radar. *Radio Science*, **20 (4)**, 907–922, https://doi.org/https://doi.org/10.1029/RS020i004p00907, URL https://agupubs.onlinelibrary.wiley.com/doi/abs/10.1029/RS020i004p00907, https://agupubs.onlinelibrary.wiley.com/doi/pdf/10.1029/RS020i004p00907.

Sachidananda, M., and D. S. Zrnić, 1986: Differential propagation phase shift and rainfall rate estimation. *Radio Science*, **21 (2)**, 235–247, https://doi.org/https://doi.org/10.1029/RS021i002p00235, URL https://agupubs.onlinelibrary.wiley.com/doi/abs/10.1029/RS021i002p00235,

https://agupubs.onlinelibrary.wiley.com/doi/pdf/10.1029/RS021i002p00235.

Sachidananda, M., and D. S. Zrnić, 1987: Rain rate estimates from differential polarization measurements. *Journal of Atmospheric and Oceanic Technology*, **4 (4)**, 588 – 598, https://doi.org/10.1175/1520-0426(1987)004⟨0588:RREFDP⟩2.0.CO;2, URL https://journals.ametsoc.org/view/journals/atot/4/4/1520-0426_1987_004_0588_rrefdp_2_0_co_2.xml.

Segall, J. H., M. M. French, D. M. Kingfield, S. D. Loeffler, and M. R. Kumjian, 2022: Storm-scale polarimetric radar signatures associated with tornado dissipation in supercells. *Weather and Forecasting*, **37 (1)**, 3 – 21, https://doi.org/10.1175/WAF-D-21-0067.1, URL https://journals.ametsoc.org/view/journals/wefo/37/1/WAF-D-21-0067.1.xml.

Seliga, T. A., and V. N. Bringi, 1976: Potential use of radar differential reflectivity measurements at orthogonal polarizations for measuring precipitation. *Journal of Applied Meteorology and Climatology*, **15 (1)**, 69 – 76, https://doi.org/10.1175/1520-0450(1976)015⟨0069:PUORDR⟩2.0.CO;2, URL https://journals.ametsoc.org/view/journals/apme/15/1/1520-0450_1976_015_0069_puordr_2_0_co_2.xml.

Sessa, M. F., and R. J. Trapp, 2020: Observed relationship between tornado intensity and pretornadic mesocyclone characteristics. *Wea. Forecasting*, **35**, 1243–1261.

Shima, S., K. Kusano, A. Kawano, T. Sugiyama, and S. Kawahara, 2009: The super-droplet method for the numerical simulation of clouds and precipitation: a particle-based and probabilistic microphysics model coupled with a non-hydrostatic model. *Quarterly Journal of the Royal Meteorological Society*, **135 (642)**, 1307–1320, https://doi.org/10.1002/qj.441, physics/0701103.

Snook, N., and M. Xue, 2008: Effects of microphysical drop size distribution on tornadogenesis in supercell thunderstorms. *Geophys. Res. Lett.*, **35**.

Snyder, J. C., H. B. Bluestein, D. T. Dawson II, and Y. Jung, 2017: Simulations of polarimetric, X-band radar signatures in supercells. Part II: ZDR columns and rings and KDP columns. *J. Appl. Meteor. Climatol.*, **56**, 2001 – 2026.

Snyder, J. C., H. B. Bluestein, V. Venkatesh, and S. J. Frasier, 2013: Observations of polarimetric signatures in supercells by an X-band mobile Doppler radar. *Mon. Wea. Rev*, **141**, 3 – 29.

Snyder, J. C., and A. V. Ryzhkov, 2015: Automated detection of polarimetric tornadic debris signatures using a hydrometeor classification algorithm. *J. Appl. Meteor. Climatol.*, **54**, 1861 – 1870.

Snyder, J. C., A. V. Ryzhkov, M. R. Kumjian, A. P. Khain, and J. Picca, 2015: A z_{DR} column detection algorithm to examine convective storm updrafts. *Wea. Forecasting*, **30**, 1819–1844, https://doi.org/10.1175/WAF-D-15-0068.1.

Straka, J. M., D. S. Zrnić, and A. V. Ryzhkov, 2000: Bulk hydrometeor classification and quantification using polarimetric radar data: Synthesis of relations. *J. Appl. Meteorol.*, **39**, 1341–1372.

Tanamachi, R. L., H. B. Bluestein, J. B. Houser, S. J. Frasier, and K. M. Hardwick, 2012: Mobile X-band, polarimetric Doppler radar observations of the 4 May 2007 Greensburg, Kansas, tornadic supercell. *Mon. Wea. Rev.*, **140**, 2103–2125.

Tanamachi, R. L., P. L. Heinselman, and L. J. Wicker, 2015: Impacts of a storm merger on the 24 may 2011 el reno, oklahoma, tornadic supercell. *Weather and Forecasting*, **30 (3)**, 501 – 524, https://doi.org/10.1175/WAF-D-14-00164.1.

Thompson, R. L., R. Edwards, J. A. Hart, K. L. Elmore, and P. Markowski, 2003: Close proximity soundings within supercell environments obtained from the Rapid Update Cycle. *Wea. Forecasting*, **18 (6)**, 1243 – 1261, https://doi.org/10.1175/1520-0434(2003)018⟨1243:CPSWSE⟩2.0.CO;2.

Tuftedal, K. S., M. M. French, D. M. Kingfield, and J. C. Snyder, 2021: Observed bulk hook echo drop size distribution evolution in supercell tornadogenesis and tornadogenesis failure. *Monthly Weather Review*, **149 (8)**, 2539 – 2557, https://doi.org/10.1175/MWR-D-20-0353.1, URL https://journals.ametsoc.org/view/journals/mwre/149/8/MWR-D-20-0353.1.xml.

Van Den Broeke, M. S., 2016: Polarimetric variability of classic supercell storms as a function of environment. *Journal of Applied Meteorology and Climatology*, **55 (9)**, 1907 – 1925, https://doi.org/10.1175/JAMC-D-15-0346.1, URL https://journals.ametsoc.org/view/journals/apme/55/9/jamc-d-15-0346.1.xml.

Van Den Broeke, M. S., 2017: Polarimetric radar metrics related to tornado life cycles and intensity in supercell storms. *Monthly Weather Review*, **145 (9)**, 3671 – 3686, https://doi.org/10.1175/MWR-D-16-0453.1, URL https://journals.ametsoc.org/view/journals/mwre/145/9/mwr-d-16-0453.1.xml.

Van Den Broeke, M. S., 2020: A preliminary polarimetric radar comparison of pretornadic and nontornadic supercell storms. *Monthly Weather Review*, **148 (4)**, 1567 – 1584, https://doi.org/10.1175/MWR-D-19-0296.1, URL https://journals.ametsoc.org/view/journals/mwre/148/4/mwr-d-19-0296.1.xml.

Van Den Broeke, M. S., and S. T. Jauernic, 2014: Spatial and temporal characteristics

of polarimetric tornadic debris signatures. *J. Appl. Meteor. Climatol.*, **53 (10)**, 2217–2231.

Van Den Broeke, M. S., M. B. Wilson, C. A. V. D. Broeke, D. J. Healey, M. J. Wood, and R. E. Nelson, 2023: Polarimetric radar observations of a long-lived supercell and associated tornadoes on 10–11 december 2021. *Monthly Weather Review*, **151 (9)**, 2501 – 2520, https://doi.org/10.1175/MWR-D-22-0330.1, URL https://journals.ametsoc.org/view/journals/mwre/151/9/MWR-D-22-0330.1.xml.

Van Weverberg, K., 2013: Impact of environmental instability on convective precipitation uncertainty associated with the nature of the rimed ice species in a bulk microphysics scheme. *Mon. Wea. Rev.*, **141**, 2841–2849.

Van Weverberg, K., A. M. Vogelmann, H. Morrison, and J. A. Milbrandt, 2012: Sensitivity of idealized squall-line simulations to the level of complexity used in two-moment bulk microphysics schemes. *Mon. Wea. Rev.*, **140**, 1883–1907.

Vich, M., and R. Romero, 2023: Exploring severe weather environments using cm1 simulations: The 29 august 2020 event in the balearic islands. *Atmospheric Research*, **290**, 106 784, https://doi.org/https://doi.org/10.1016/j.atmosres.2023.106784, URL https://www.sciencedirect.com/science/article/pii/S0169809523001813.

Vivekanandan, J., S. M. Ellis, R. Oye, D. S. Zrnić, A. V. Ryzhkov, and J. Straka, 1999: Cloud microphysics retrieval using S-band dual-polarization radar measurements. *Bull. Amer. Meteor. Soc.*, **80**, 381 – 388.

Vulpiani, G., M. Montopoli, D. P. Luca, A. G. Gioia, P. Giordano, and F. S. Marzano, 2012: On the use of dual-polarized C-band radar for operational rainfall retrieval in mountainous areas. *J. Appl. Meteor. Climat.*, **51 (2)**, 405–425, https://doi.org/10.1175/JAMC-D-10-05024.1.

Wakimoto, R. M., Z. B. Wienhoff, H. B. Bluestein, D. J. Bodine, and J. M. Kurdzo, 2020: Mobile radar observations of the evolving debris field compared with a damage survey of the Shawnee, Oklahoma tornado of 19 May 2013. *Mon. Wea. Rev.*, **148**, 1779 – 1803, https://doi.org/10.1175/MWR-D-19-0215.1.

Waterman, P. C., 1965: Matrix formulation of electromagnetic scattering. *IEEE Proceedings*, **53 (8)**, 805–812, https://doi.org/10.1109/PROC.1965.4058.

Weiss, J., 1991: The dynamics of enstrophy transfer in two-dimensional hydrodynamics. *Physica D: Nonlinear Phenomena*, **48 (2)**, 273–294, https://doi.org/https://doi.org/10.1016/0167-2789(91)90088-Q, URL https://www.sciencedirect.com/science/article/pii/016727899190088Q.

Wicker, L. J., and R. B. Wilhelmson, 1995: Simulation and analysis of tornado development and decay within a three-dimensional thunderstorm. *J. Atmos. Sci.*, **52**, 2675–2703.

Wilson, M. B., and M. S. Van Den Broeke, 2022: Using the supercell polarimetric observation research kit (SPORK) to examine a large sample of pretornadic and nontornadic supercells. *Electron. J. Severe Storms Meteor.*, **17 (29)**, URL https://ejssm.com/ojs/index.php/site/article/view/85.

Wu, W., W. Huang, L. Deng, and C. Wu, 2022: Investigation of maximum hail-size forecasting using bulk microphysics schemes. *Monthly Weather Review*, **150 (10)**, 2503 – 2525, https://doi.org/10.1175/MWR-D-21-0312.1, URL https://journals.ametsoc.org/view/journals/mwre/150/10/MWR-D-21-0312.1.xml.

Wurman, J., and M. Randall, 2001: An inexpensive, mobile, rapid-scan radar. *30th Conf. on Radar Meteor.*, Munich, Germany.

Yao, D., H. Xue, J. Yin, J. Sun, X. Liang, and J. Guo, 2018: Investigation into the formation, structure, and evolution of an EF4 tornado in east China using a high-resolution numerical simulation. *Journal of Meteorological Research*, **32 (2)**, 157–171, https://doi.org/10.1007/s13351-018-7083-0.

Yokota, S., H. Niino, H. Seko, M. Kunii, and H. Yamauchi, 2018: Important factors for tornadogenesis as revealed by high-resolution ensemble forecasts of the tsukuba supercell tornado of 6 may 2012 in japan. *Monthly Weather Review*, **146 (4)**, 1109 – 1132.

Yuter, S. E., and R. A. Houze, 1995: Three-dimensional kinematic and microphysical evolution of Florida cumulonimbus. Part II: Frequency distributions of vertical velocity, reflectivity, and differential reflectivity. *Mon. Wea. Rev.*, **123**, 1941 – 1963.

Zhang, G., J. Gao, and M. Du, 2021: Parameterized forward operators for simulation and assimilation of polarimetric radar data with numerical weather predictions. *Advances in Atmospheric Sciences*, **38**, 737–754, https://doi.org/10.1007/s00376-021-0289-6.

Ziegler, C. L., 1985: Retrieval of thermal and microphysical variables in observed convective storms. part i: Model development and preliminary testing. 1487–1509 pp.

Zovko-Rajak, D., K. Tory, and J. Kepert, 2023: A case study of south australia's severe thunderstorm and tornado outbreak 28 september 2016. *Journal of Southern Hemisphere Earth Systems Science*, **73**, 178–193, https://doi.org/10.1071/ES22006.

Zrnić, D. S., and A. Ryzhkov, 1996: Advantage of rain measurements using specific differential phase. *J. Atmos. Oceanic Technol.*, **13**, 454 – 464, https://doi.org/https://doi.org/10.1175/1520-0426(1996)013⟨0454:AORMUS⟩2.0.CO;2.